

The Pennsylvania State University  
The Graduate School  
Department of Energy & Mineral Engineering

**ELECTROCHEMICAL DEGRADATION, KINETICS & PERFORMANCE  
STUDIES OF SOLID OXIDE FUEL CELLS**

A Dissertation in  
Energy & Mineral Engineering  
by  
Debanjan Das

© 2016 Debanjan Das

Submitted in Partial Fulfillment  
of the Requirements  
for the Degree of

Doctor of Philosophy

May 2016

The Dissertation of Debanjan Das was reviewed and approved\* by the following:

Serguei N. Lvov

Professor of Energy and Mineral Engineering & Materials Science and Engineering,  
Director of Electrochemical Technologies Program  
Dissertation Adviser  
Chair of Committee

Derek Elsworth

Professor of Energy and Mineral Engineering

Sarma Pisupati

Professor of Energy & Mineral Engineering

Michael Janik

Associate Professor of Chemical Engineering

Luis F. Ayala

Associate Professor of Petroleum and Natural Gas Engineering  
Associate Department Head for Graduate Education

\* Signatures are on file in the Graduate School

## *Abstract*

---

Linear and Non-linear electrochemical characterization techniques and equivalent circuit modelling were carried out on miniature and sub-commercial Solid Oxide Fuel Cell (SOFC) stacks as an *in-situ* diagnostic approach to evaluate and analyze their performance under the presence of simulated alternative fuel conditions. The main focus of the study was to track the change in cell behavior and response live, as the cell was generating power. Electrochemical Impedance Spectroscopy (EIS) was the most important linear AC technique used for the study.

The distinct effects of inorganic components usually present in hydrocarbon fuel reformates on SOFC behavior have been determined, allowing identification of possible "fingerprint" impedance behavior corresponding to specific fuel conditions and reaction mechanisms. Critical electrochemical processes and degradation mechanisms which might affect cell performance were identified and quantified. Sulfur and siloxane cause the most prominent degradation and the associated electrochemical cell parameters such as Gerisher and Warburg elements are applied respectively for better understanding of the degradation processes.

Electrochemical Frequency Modulation (EFM) was applied for kinetic studies in SOFCs for the very first time for estimating the exchange current density and transfer coefficients. EFM is a non-linear *in-situ* electrochemical technique conceptually different from EIS and is used extensively in corrosion work, but rarely used on fuel cells till now. EFM is based on exploring information obtained from non-linear higher harmonic contributions from potential perturbations of electrochemical systems, otherwise not obtained by EIS. The baseline fuel used was 3 % humidified hydrogen with a 5-cell SOFC sub-commercial planar stack to perform the analysis. Traditional methods such as EIS and Tafel analysis were carried out at similar operating conditions

to verify and correlate with the EFM data and ensure the validity of the obtained information. The obtained values closely range from around  $11 \text{ mA cm}^{-2}$  -  $16 \text{ mA cm}^{-2}$  with reasonable repeatability and excellent accuracy. The potential advantages of EFM compared to traditional methods were realized and our primary aim at demonstrating this technique on a SOFC system are presented which can act as a starting point for future research efforts in this area.

Finally, an approach based on *in-situ* State of Health tests by EIS was formulated and investigated to understand the most efficient fuel conditions for suitable long term operation of a solid oxide fuel cell stack under power generation conditions. The procedure helped to reflect the individual effects of three most important fuel characteristics  $\text{CO}/\text{H}_2$  volumetric ratio, S/C ratio and fuel utilization under the presence of a simulated alternative fuel at  $0.4 \text{ A cm}^{-2}$ . Variation tests helped to identify corresponding electrochemical/chemical processes, narrow down the most optimum operating regimes considering practical behavior of simulated reformer-SOFC system arrangements. At the end, 8 different combinations of the optimized parameters were tested long term with the stack, and the most efficient blend was determined.

## TABLE OF CONTENTS

<b>List of Figures .....</b>	<b>vii</b>
<b>List of Tables.....</b>	<b>xiii</b>
<b>Acknowledgements.....</b>	<b>xv</b>

### **Chapter 1 Introduction & Overview**

<i>Fuel Cells – A General Description.....</i>	<i>01</i>
<i>Types of Fuel Cells .....</i>	<i>03</i>
<i>Solid Oxide Fuel Cell (SOFC) – Overview .....</i>	<i>03</i>
<i>SOFCs – Concept of the Three-Phase Boundary .....</i>	<i>05</i>
<i>Polarization in SOFCs .....</i>	<i>07</i>
<i>Equilibrium Thermodynamics of SOFC – The Nernst Equation .....</i>	<i>11</i>
<i>Research Motivation &amp; Overall Structure of the Dissertation.....</i>	<i>12</i>
<i>References .....</i>	<i>14</i>

### **Chapter 2 Instrumental & Experimental Descriptions**

<i>Button Fuel Cell Setup &amp; Stack Assembly .....</i>	<i>15</i>
<i>Button Cell Membrane Electrode Assembly (MEA) .....</i>	<i>19</i>
<i>Fuel &amp; Oxidant Arrangements .....</i>	<i>20</i>
<i>DC Electrochemical Characterization .....</i>	<i>20</i>
<i>Electrochemical Impedance Spectroscopy (EIS) .....</i>	<i>21</i>
<i>Equivalent Circuit Modeling (ECM) .....</i>	<i>23</i>
<i>Electrochemical Frequency Modulation (EFM) – A new technique used in SOFC .....</i>	<i>31</i>
<i>References .....</i>	<i>32</i>

### **Chapter 3 Poisoning Effects in Solid Oxide Fuel Cells operating on Alternative Fuel Reformate Streams in Presence of Inorganic Impurities**

<i>Preface to Chapter 3.....</i>	<i>33</i>
<i>Introduction .....</i>	<i>34</i>
<i>Experimental</i>	
<i>Anode Supported SOFC Button Cell .....</i>	<i>36</i>
<i>Electrochemical Testing .....</i>	<i>38</i>
<i>Impedance Diagram Fitting .....</i>	<i>40</i>
<i>Results and Discussion</i>	
<i>Baseline Impedance Behavior with Reformate .....</i>	<i>41</i>
<i>Degradation Due to Sulfur Poisoning .....</i>	<i>45</i>
<i>Siloxane Poisoning &amp; Degradation Modelling .....</i>	<i>53</i>
<i>Chlorine Poisoning &amp; Degradation Modelling .....</i>	<i>63</i>
<i>Performance Regaining Tests .....</i>	<i>68</i>
<i>Summary .....</i>	<i>73</i>
<i>References .....</i>	<i>76</i>

## **Chapter 4 Electrochemical Frequency Modulation for Estimation of Exchange Current Density in Solid Oxide Fuel Cells**

<b><i>Preface to Chapter 4</i></b> .....	79
<b><i>Introduction</i></b> .....	80
<b><i>Background Theory</i></b>	
<i>Exchange Current Density and Butler-Volmer equation</i> .....	85
<i>Tafel slopes and Concept of Transfer Coefficient (<math>\alpha</math>)</i> .....	87
<i>Electrochemical Frequency Modulation (EFM)</i> .....	89
<b><i>Experimental</i></b> .....	90
<b><i>Results and Discussion</i></b> .....	92
<b><i>Conclusion</i></b> .....	103
<b><i>References</i></b> .....	104

## **Chapter 5 Sensitivity Studies of Fuel Characteristics and State of Health Test of a Planar SOFC Short Stack Operating on Syngas by Electrochemical Impedance Spectroscopy**

<b><i>Preface to Chapter 5</i></b> .....	106
<b><i>Introduction</i></b> .....	108
<b><i>Experimental</i></b> .....	110
<b><i>Results and discussion</i></b>	
<i>Baseline DC Polarization Behavior</i> .....	111
<i>Baseline AC Impedance Behavior</i> .....	113
<i>Impact of CO/H<sub>2</sub> volumetric composition ratio</i> .....	120
<i>Impact of low Steam to Carbon (S/C) ratio</i> .....	125
<i>Impact of Fuel Utilization</i> .....	132
<i>Long Term Operation with Optimized Conditions</i> .....	134
<b><i>Conclusions</i></b> .....	138
<b><i>References</i></b> .....	141

## **Chapter 6 Summary of the Research**..... 144

## **Chapter 7 General Conclusions and Future Directions**..... 146

## **Appendix** ..... 149

## List of Figures

---

<b>Fig. 1.1</b> A general simplified schematic of a typical fuel cell setup.....	02
<b>Fig. 1.2</b> A schematic of a working SOFC system showing the flow of oxygen anions and the electrons across the external circuit.....	05
<b>Fig. 1.3</b> Microscopic view of the electrolyte-electrode.....	06
<b>Fig. 1.4</b> The Three Phase Boundary interface.....	06
<b>Fig 1.5</b> Sources of Polarization as a function of current density.....	08
<b>Fig. 2.1</b> (Left) Anode surface, (Right) Cathode surface in black with an interlayer white electrolyte.....	16
<b>Fig 2.2</b> A detailed schematic of the SOFC button cell test arrangement.....	17
<b>Fig 2.3</b> A simplified schematic of the SOFC stack testing setup.....	18
<b>Fig. 2.4</b> (Top left) Delphi Gen 3.2 a 5-cell stack, (Top Right) Box furnace with stack installed, (Bottom left) Stack and manifold inside the furnace (Bottom Right) Electrical & gas connections from furnace top.....	18
<b>Fig. 2.5</b> (Left) Small amplitude of input potential perturbation producing a pseudo-linear current response (Right) Mathematical treatment for the input-response impedance data showing the phase shift $\phi$ . Complex impedance is written and can be plotted in the form of real and imaginary part.....	23
<b>Fig. 2.6</b> Representation of an ideal resistor.....	24

<b>Fig. 2.7</b> Representation of an ideal capacitor.....	24
<b>Fig. 2.8</b> Representation of a series R-C circuit.....	25
<b>Fig. 2.9</b> Representative Nyquist plot for a ideally polarizable electrode.....	25
<b>Fig. 2.10</b> (Left) Representation of a parallel R-C circuit (Right) Representative Nyquist plot for a real world polarizable electrode.....	26
<b>Fig. 2.11</b> (Left) Representation of a parallel R-C circuit with a series ohmic resistance (Right) Representative Nyquist plot for a real world polarizable electrode.....	27
<b>Fig. 2.12</b> Representative Nyquist plot for a CPE element in the form of a depressed semi-circle.....	27
<b>Fig 2.13</b> (Left) Representation of a Warburg element with a parallel R-C circuit (Right) Representative Nyquist plot for a Warburg element showing mass diffusion behavior.....	29
<b>Fig 2.14</b> Diagram illustrating the working principle of the FRA for an EIS measurement. CE – Counter Electrode, RE – Reference, WE – Working, $Z_{IM}$ & $Z_{RE}$ – Imaginary & Real impedance.....	30
<b>Fig 2.15</b> A simplified representation of the EFM concept.....	31
<b>Fig. 3.1</b> (a) A schematic of the experimental setup (b) Equilibrium composition diagram of the fuel feed with respect to the operational temperature.....	37
<b>Fig. 3.2</b> (a) Subtraction Impedance spectra of the SOFC cell at 750 °C exposed to the simulated reformat observed after 100, 200 and 500 h at OCP. (b) Subtraction Impedance spectra of the SOFC cell at 750 °C exposed to the simulated reformat observed after 100, 200 and 500 h at	

galvanostatic conditions of  $0.3 \text{ A cm}^{-2}$ . (c) Equivalent Circuit model to fit reformat fuelled impedance data for both OCP and galvanostatic conditions.....43

**Fig. 3.3 (a)** Stability diagram of the Ni-H-S system derived from thermochemical calculations over a temperature range at a constant hydrogen partial pressure. **(b)** Stability diagram of the Ni-H-S system derived from thermochemical calculations over a hydrogen partial pressure range at a constant temperature. **(c)** Stability diagram of the Ni-H-Cl system derived from thermochemical calculations over a hydrogen partial pressure range at a constant temperature. **(d)** Stability diagram of the Ni-H-Cl system derived from thermochemical calculations over a hydrogen partial pressure range at a constant temperature.....46

**Fig. 3.4** Subtraction impedance spectra of the SOFC cell relative to the start of the test at  $750^\circ\text{C}$  exposed to the simulated reformat observed after 200 h at  $0.3 \text{ A cm}^{-2}$  for 0.2, 1 and 4 ppm of  $\text{H}_2\text{S}$ . **(b)** Equivalent Circuit model to fit the sulfur poisoned reformat fuelled impedance data.....48

**Fig. 3.5 (a)** Cell potential - time curve for 10 ppm  $\text{D}_5$  on simulated reformat at current density of  $0.3 \text{ A cm}^{-2}$ . **(b)** Impedance spectra of the SOFC at  $750^\circ\text{C}$  exposed to the simulated reformat with 1 ppm of  $\text{D}_5$  taken after 1, 7 and 20 h at a current density  $0.3 \text{ A cm}^{-2}$ . (Notice the irregular and inconsistent nature in the low frequency region and high increase in ohmic impedance). **(c)** Current density vs. time for a siloxane poisoning test in SOFC fueled by simulated reformat with 0.2 ppm of  $\text{D}_5$  at a potential of 0.58 V .....55

**Fig. 3.6 (a)** Subtraction impedance spectra for the SOFC at  $750^\circ\text{C}$  exposed to the simulated reformat with 0.2 ppm of siloxane during a period of 300 h at a current density  $0.3 \text{ A cm}^{-2}$ . **(b)** The inset below shows the high frequency region of the impedance spectra. **(c)** Equivalent circuit model to simulate the impedance spectra for siloxane poisoning.....57

**Fig. 3.7 (a)** Evolution of the impedance (charge transfer and gas diffusion resistance) for the SOFC at 750 °C exposed to the simulated reformat with 0.2 ppm of siloxane during a period of 300 h at a current density  $0.3 \text{ A cm}^{-2}$ . **(b)** Evolution of the impedance (charge transfer and gas diffusion resistance) for the SOFC with respect to operating temperature exposed to the simulated reformat with 0.2 ppm of siloxane after 50 h of operation at a current density  $0.3 \text{ A cm}^{-2}$  .....61

**Fig. 3.8 (a)** Subtraction impedance spectra for the SOFC at 750 °C exposed to the simulated reformat with 20, 50 and 100 ppm of  $\text{Cl}_2$  after 200 h at a current density  $0.3 \text{ A cm}^{-2}$ . **(b)** The figure below shows a close-up of the high frequency region of the impedance spectra. **(c)** Equivalent circuit model to simulate the impedance spectra for chlorine poisoning.....66

**Fig. 3.9 (a)** Current density vs. time for a sulfur poisoning test in SOFC fueled by simulated reformat with 1 ppm of  $\text{H}_2\text{S}$  at a potential of 0.55 V. **(b)** Potential vs. time for a sulfur poisoning test in SOFC fueled by simulated reformat with 1 ppm of  $\text{H}_2\text{S}$  – OCP condition compared with polarized condition.....69

**Fig. 3.10 (a)** Current density vs. time for a siloxane poisoning test in SOFC fueled by simulated reformat with 0.2 ppm of  $\text{D}_5$  at a potential of 0.58 V. **(b)** Cell potential - time curve for 50 ppm  $\text{Cl}_2$  on simulated reformat at current density of  $0.3 \text{ A cm}^{-2}$  .....72

**Fig. 4.1(a)** Nyquist Plot for at OCP at 750 °C with fuel: 3 % wet  $\text{H}_2$  (2.5 SLPM), oxidant: Air (5 SLPM). **(Inset)** Circuit Model fitted by CNLS method to model the experimental data. **(b)** Impedance parameter trends for cell 3 with varying overpotential and operating temperature, to determine the dependency of the respective arc  $R_2$  on anodic charge transfer process.....93

**Fig. 4.2 (a)** LSV data for at 750 °C with fuel: 3 % wet H<sub>2</sub> (2.5 SLPM), oxidant: Air (5 SLPM). **(b)** Straight line fit with the equation for the linear Tafel plot in SOFC mode **(c)** Comparison between estimated polarization data from obtained parameters and experimentally measured LSV data. **(d)** Intermodulation Spectra at 750 °C; Fuel: 3 % Wet H<sub>2</sub> (2.5 SLPM), Oxidant: Air (5 SLPM).....95

**Fig. 5.1** Polarization plots showing stack voltage and power density with respect to current run on baseline fuel conditions.....112

**Fig. 5.2 (a)** Impedance spectra of the SOFC stack at 750 °C exposed to hydrogen fuel and reformat blend at OCP mode with fuel flow - 5 L min<sup>-1</sup>, air flow - 10 L min<sup>-1</sup>, S/C = 2 **(b)** Impedance spectra of the SOFC stack at 750 °C exposed to hydrogen fuel and reformat blend at 0.4 A cm<sup>-2</sup> with same conditions.....114

**Fig. 5.3** Circuit Model fitted by CNLS method to model the (a) baseline experimental data for hydrogen fuel (b) baseline experimental data for reformat blend and (c) impedance data obtained from S/C values of 0.95, 0.83 and 0.62.....115

**Fig. 5.4 (a)** Parameter dependency of R2 (630 Hz – 1 kHz) on overpotential and temperature. **(b)** Parameter dependency of R3 (2.5 Hz – 10 Hz) on H<sub>2</sub>O partial pressure and temperature.....117

**Fig. 5.5** Bode plot (phase angle v/s logarithmic frequency) showing the respective peaks (rectangular boxes) for the hydrogen fuel and reformat blend across a frequency range of 1 kHz to 0.05 Hz.....118

**Fig. 5.6** Impedance spectra of the SOFC stack at 750 °C exposed to reformat blend at 0.4 A cm<sup>-2</sup> with varying CO:H<sub>2</sub> (X<sub>f</sub>) ratios fuel flow - 5 L min<sup>-1</sup>, air flow - 10 L min<sup>-1</sup>, S/C = 2.....122

**Fig. 5.7 (a)** Impedance spectra of the SOFC stack at 750 °C exposed to reformat blend at 0.4 A cm<sup>-2</sup> with varying S/C ratios fuel flow - 5 L min<sup>-1</sup>, air flow - 10 L min<sup>-1</sup>,  $X_f = 0.5$ . **(b)** Equilibrium carbon formation diagram with the base fuel used for varying S/C ratios with respect to operating temperature.....127

**Fig. 5.8** Area specific resistances with respect to fuel utilization % for SOFC stack at 750 °C exposed to reformat blend at 0.4 A cm<sup>-2</sup> with S/C ratio = 2, air flow - 10 L min<sup>-1</sup>,  $X_f = 0.5$ .....133

**Fig. 5.9 (a)** Degradation rates in % per 500 h of the SOFC stack at 750 °C for eight optimized operating conditions consisting of three variables:  $X_f$ , S/C and FU %. **(b)** Percentage increase in area specific resistances per 500 h for the SOFC stack at 750 °C with eight optimized operating conditions ( $R_{2SOH}$  [left],  $R_{3SOH}$  [middle],  $R_{4SOH}$  [right]).....137

## List of Tables

---

<b>Table 1.1</b> Properties, compositions and conditions for the five types of fuel cells.....	04
<b>Table 3.1</b> Resistive parameters obtained from the equivalent circuit modeling of the subtraction impedance spectra for pure reformato fueled button cells.....	44
<b>Table 3.2</b> Electrochemical parameters as a function of time obtained from the equivalent circuit modeling of the subtraction impedance spectra for sulfur poisoning tests.....	51
<b>Table 3.3</b> Electrochemical parameters as a function of time obtained from the equivalent circuit modeling of the subtraction impedance spectra for siloxane poisoning tests.....	60
<b>Table 3.4</b> Electrochemical parameters as a function of time obtained from the equivalent circuit modeling of the subtraction impedance spectra for chlorine poisoning tests.....	67
<b>Table 4.1</b> Values of the electrochemical parameters obtained from CNLS fitting of the impedance diagram from Fig. 4.1a.....	94
<b>Table 4.2</b> Current components obtained with EFM for the corresponding excitation, harmonic and intermodulation frequencies.....	99
<b>Table 4.3</b> Comparative values of the Exchange Current Density Obtained from EIS, LSV, and EFM.....	101
<b>Table 5.1</b> Composition of Hydrogen and Reformato blend used for baselines current –potential and impedance plots.....	111
<b>Table 5.2</b> Electrochemical resistances obtained from the CNLS fitting for Hydrogen and Reformato blend used for baselines impedance plots.....	116

<b>Table 5.3</b> Range of compositions used for Reformate blend with varying CO/H <sub>2</sub> ( $X_f$ ) values.....	121
<b>Table 5.4</b> Electrochemical resistances obtained from the CNLS fitting for Reformate blend with varying CO/H <sub>2</sub> ( $X_f$ ) values.....	122
<b>Table 5.5</b> Electrochemical parameters obtained from the CNLS fitting for Reformate blend with varying S/C values.....	129
<b>Table 5.6</b> Optimized operating conditions selected for long term stack performance tests.....	135

## Acknowledgment

---

First, I would like to express my sincere gratitude to my advisor, Dr. Serguei N. Lvov, for his constant support, advice, and encouragement throughout my graduate study. I really appreciate his timely help on different occasions and his great sense of humor, which made my research enjoyable. Apart from a great scientist, he is an accomplished teacher and I have greatly benefitted from his innovative techniques to learn different areas of electrochemical engineering. His scientific attitude and achievements in the area of electrochemical science and engineering always motivate me to grow as a researcher.

I would also like to extend my sincere gratitude to Dr. Sarma Pisupati, Dr. Derek Elsworth, and Dr. Michael Janik for their support and serving as my committee members. I am also thankful to the Department of Energy and Delphi Automotive Systems, Michigan for providing me the much needed financial support during my stay at Penn State.

I am extremely grateful to my lab-mates Dr. Mark LaBarbera, Dr. Justin Beck, Derek Hall and Dr. Sanchit Khurana for supporting me in various endeavors and contributing to the research work presented in this dissertation. I am especially thankful to Derek Hall and Dr. Justin Beck for their constant advice on data analysis and interpretations.

Finally, I truly appreciate my family for their constant love and affection. My parents, Dibyendu and Swastika have always provided me with their support and encouragement. I would also like to thank all my friends in Penn State who made my grad school life more enjoyable. At the end, I want to thank the tennis legend Roger Federer, a person whom I have admired and idolized throughout my life, who has been an indirect but constant source of inspiration and encouragement in all the tough times I have encountered at Penn State. Thank you all.

## Chapter 1

---

### Introduction & Overview

#### 1.1 Fuel Cells – A General Description

Fuel cells are electrochemical energy conversion devices which directly transform the chemical energy of fuels into useful electrical energy which can be used to power systems and devices. A single unit of a fuel cell undergoes an oxidation reaction of the fuel, commonly hydrogen and the reduction reaction, commonly oxygen from the air. The oxidation takes place at the anode (fuel electrode) and the reduction takes place at the cathode (air electrode). The representative equation which describes the primary fuel cell reaction which produces electrical energy, heat and byproduct as water is shown in the equation below [1-3],



A physical description of a typical fuel cell system is required to explain the electrochemistry occurring in the overall process as shown in Fig. 1.1. An electrolyte which is fabricated as a non-porous material is sandwiched directly between two porous electrodes namely anode and cathode. The two electrodes are in contact with the electrolyte either electronically or ionic or both and constitute a closed circuit. The anode is exposed to the fuel and the cathode is exposed to the air in most common cases. Continuous energy will be produced from the system as long there is a constant supply of fuel and oxidant at the respective electrodes. In this respect they are different and desirable alternatives to battery technologies because of its ability to constantly generate useful power in presence of fuel and air. For the above reason fuel cells can be termed as thermodynamically open systems.

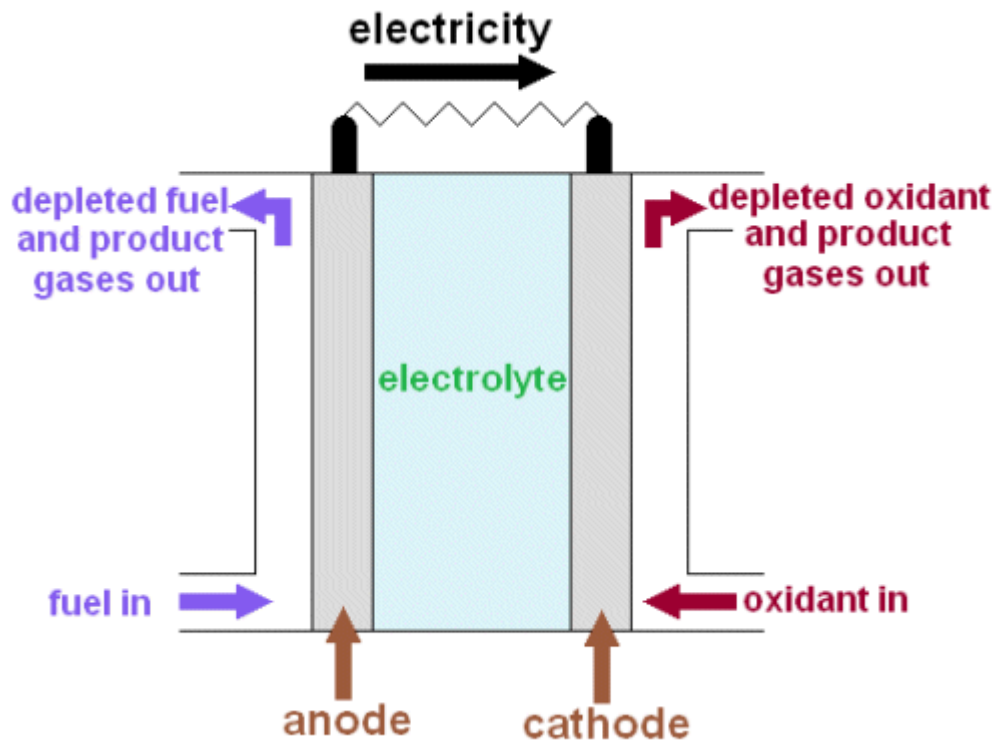


**Fig. 1.1** A general simplified schematic of a typical fuel cell setup

Fuel cells also have a high conversion and thermodynamic efficiency during its electrochemical energy conversion process. When compared to internal combustion engines and other energy producing sources, mechanical energy losses and heat evolution losses are not a concern in such systems. In some cases the heat evolved from a fuel cell system can be used to contribute in combined heat and power systems and also to maintain the fuel cell temperature. Also production of conventional air pollutants such as  $\text{NO}_x$  and  $\text{SO}_x$  are negligible [4] and lesser as compared to other systems. Another important merit is the fact that the size of a fuel cell system does not have any impact of its efficiency which makes it easily accessible to be used in various and specific uses depending on the ability of a type of a fuel cell system to cater to the requirements of that particular application. It hardly generates any noise by itself and thus is also a quiet energy source. The final and most important aspect of a fuel cell in general is their ability and flexibility to work on different types of fuels (especially high temperature systems) which makes it a commercially viable,

feasible and efficient power generation system based on a variety of different application areas in the market [2,4].

## **1.2 Types of Fuel Cells**

Fuel cells can be categorized into five primary types. The main differentiating factor is the nature and type of electrolyte which separates the two electrode chambers. Also, differences which are pertinent are the operating temperature and also the phase of the fuel used (gaseous or liquid). The main types include Solid Oxide Fuel Cells (SOFCs), Polymer Electrolyte Membrane (PEMFC), Molten Carbonate (MCFC), Phosphoric Acid (PAFC) and Alkaline (AFC). With an increase in operating temperature, the fuel flexibility aspect becomes more relaxed. The table 1-1 [1] below summarizes the different kinds of fuel cells with their inherent properties and material compositions.

## **1.3 Solid Oxide Fuel Cell (SOFC) – Overview**

SOFCs are high temperature fuel cells which is mainly composed of solid ceramic electrodes and electrolytes and fuel/oxidant in the gaseous phase. They commonly consist of a dense yttria-stabilized zirconia (YSZ) electrolyte (8 % w/w  $\text{Y}_2\text{O}_3$  in  $\text{ZrO}_2$ ). At high temperatures of 600 C – 900 C, the electrolyte becomes conductive only to ions which initiates the overall electrochemical reaction. The commonly used anode and cathode materials are Ni/YSZ cermets and Lanthanum Strontium Manganate LSM/YSZ composite ceramics. As shown in Fig. 1.2 in a simplified way, the fuel molecules are catalyzed and oxidized at the anode which combines with the electrolyte transported oxygen anions ( $\text{O}^{2-}$ ) produced from the reduction reaction of the oxygen molecules at the cathode. In the above process two electrons are produced at the anode which are transported across the external circuit towards the cathode, after performing useful work. The oxygen

molecules use these two electrons to continue the reduction at the cathode, thus completing the circuit and the entire process continues as long as there is also a constant fuel supply at the anode.

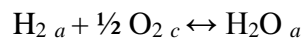
**Table 1.1** Properties, compositions and conditions for the five types of fuel cells [1]

	Solid Oxide Fuel Cell (SOFC)	Molten Carbonate Fuel Cell (MCFC)	Phosphoric Acid Fuel Cell (PAFC)	Alkaline Fuel Cell (AFC)	Polymer Electrolyte Fuel Cell (PEFC)
Typical Electrolyte	Solid YSZ (Y <sub>2</sub> O <sub>3</sub> -stabilized ZrO <sub>2</sub> )	Molten Li <sub>2</sub> CO <sub>3</sub> -K <sub>2</sub> CO <sub>3</sub>	H <sub>3</sub> PO <sub>4</sub>	KOH solution	PFS* acid membrane
Electrolyte Support	None	LiAlO <sub>2</sub>	SiC	Asbestos	None
Cathode	LSM (Sr-doped LaMnO <sub>3</sub> )	Li-doped NiO	PTFE**-bonded Pt on C	Pt-Au	PTFE-bonded Pt on C
Anode	Ni/YSZ	Ni	PTFE-bonded Pt on C	Pt-Pd	PTFE-bonded Pt on C
Interconnect	Doped LaCrO <sub>3</sub>	Stainless Steel with Ni	Glassy carbon	Ni	Graphite
Operating Temperature	1000°C	650 °C	200 °C	100 °C	80 °C
Operating Pressure	1 atm	1-3 atm	1-8 atm	1-10 atm	1-5 atm
Fuel (most common)	H <sub>2</sub> , CO	H <sub>2</sub> , CO	H <sub>2</sub>	H <sub>2</sub>	H <sub>2</sub>
Oxidant	O <sub>2</sub>	O <sub>2</sub> and CO <sub>2</sub>	O <sub>2</sub>	O <sub>2</sub>	O <sub>2</sub>
Contaminant Tolerance	< 10-100 ppm S	< ppm range S	< 1-2 % CO < 50 ppm S	No CO <sub>2</sub> , CO No S	< 50 ppm CO No S

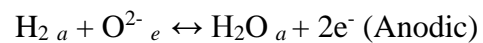
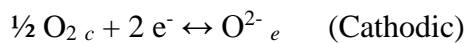
\*PFS = Perfluorosulfonic

\*\*PTFE = Polytetrafluoroethylene

The overall electrochemical reaction considering the basic fuel as H<sub>2</sub> can be written as following where  $a$  denotes the species at the anode and  $c$  denotes the species at the cathode.



The above full cell reaction can be broken down into anodic and cathodic reactions separately ( $e$  represents the species at the electrolyte)



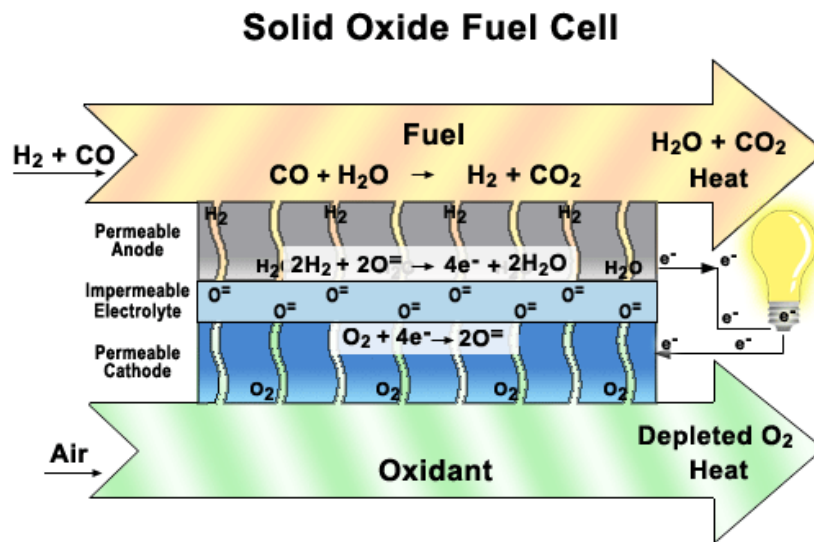


**Fig. 1.2** A schematic of a working SOFC system showing the flow of oxygen anions and the electrons across the external circuit.

#### 1.4 SOFCs – Concept of the Three-Phase Boundary

Nickel is the most generic metal of choice to constitute the bulk of the metal component of the cermet anode due to its high electrochemical activity, higher economic efficiency, and chemical stability. However, it does have disadvantages, as it can diffuse away in certain conditions. The high metal composition ensures electronic conduction occurs easily, and that electrons produced near the anode-electrolyte double phase interface during fuel oxidation reach the current collector. The incorporation of ion conducting YSZ into the anode as seen in Fig. 1.3 and 1.4, to create a cermet material has many purposes, primary being the increase in the number of three phase boundary (TBP) catalytic sites and in the process an increase the overall efficiency of the fuel oxidation reaction. The electrochemical reaction itself takes place in a region aptly named the triple phase boundary or three-phase boundary (TPB). It is here that the three key components meet to effectuate electrochemical oxidation, in the case of the anode.

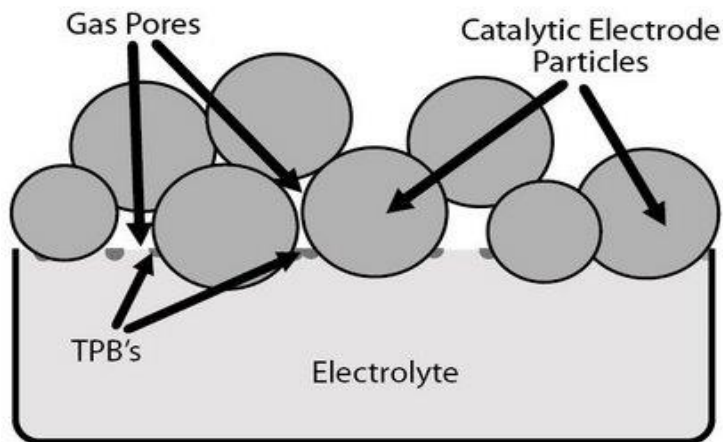


**Fig. 1.3** Microscopic view of the electrolyte-electrode

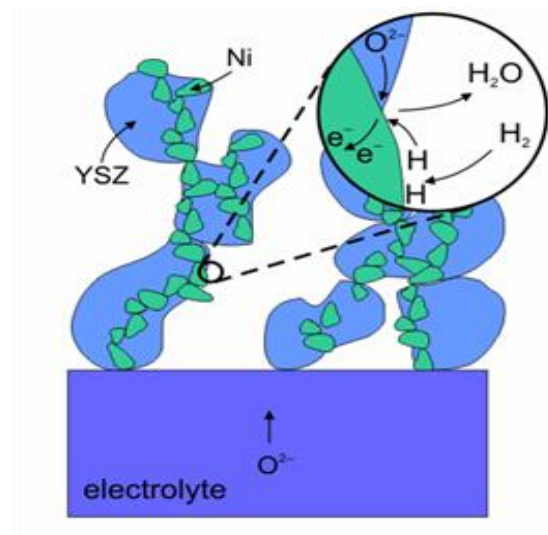


**Fig. 1.4** Three Phase Boundary interface

Oxygen anions, produced at the cathode, migrate through the non-porous electrolyte layer via an ionic conduction mechanism. Gaseous fuel which has diffused through the pores of the anode reaches the solid surface. Electrons produced by the electrochemical oxidation are conducted to the current collector via the reduced metal component. It is where these three phases (namely the reduced metal (alloy), YSZ and the gaseous fuel) contact that the electrochemical reduction at the TPB occurs. The TBP is greatly extended beyond simply the interface between the porous anode and non-porous electrolyte. This has also been described as ‘delocalizing’ the electrochemically active region [4,5]. Oxygen anions can diffuse from the non-porous electrolyte layer further into the porous anode layer through the additional YSZ ceramic phase, which increases the number of triple phase boundary sites. Nickel, in its pure form, tends to aggregate to form larger particles when exposed to high temperatures, known as sintering. During early SOFC development, this process occurred in the extreme, which greatly reduced the number of active sites. Incorporation of YSZ into the Ni to form a cermet greatly reduces the observed degree of aggregation. There is also a considerable mis-match between the thermal expansion coefficients of Ni and YSZ. Contact between the anode and YSZ upon sintering or heating to operational temperatures can cause the

anode to shear and loose physical and electrical contact with the electrolyte layer. This will have detrimental effects on the performance of the cell. Incorporating YSZ into the anode cermet allows for a more favorable match of thermal expansion coefficients, thus reducing the possibility of loss of contact between the anode and electrolyte layers.

## 1.5 Polarization in SOFCs

Polarization can be defined as a voltage loss or overpotential, which is a function of current density. The total cell polarization can be calculated as the sum of the activation polarizations of the anode and cathode kinetics,  $\eta_a$  and  $\eta_c$ , respectively, the ohmic polarization,  $iR$ , and the concentration polarization  $\eta_{cp}$  as shown below [1-5],

$$\eta_{Tot} = \eta_a + \eta_c + iR + \eta_{cp}$$

The polarization is related to the current density drawn from the full cell, as shown in the plot below in Fig. 1.5. The general trend is that, as more current is drawn from the cell, the voltage decreases below the theoretical maximum voltage. This relationship shows three regions: activation polarization causes an initial drop in cell potential at low current densities, ohmic losses create a semi-linear region at moderate current densities, and mass transport losses show a sharp decrease at high current densities. Even though the above behavior is the general trend in most fuel cell polarization tests, but the nature of the curves can change from system to system based on various operating conditions. These three regions will be described in detail in the following paragraphs. The overpotentials of both the anode and cathode increase as current density increases, which relates to the capacity to draw power from the cell, namely, at high overpotentials, less power will be available. It is, therefore, desirable to maintain polarizations of the electrodes at a minimum.

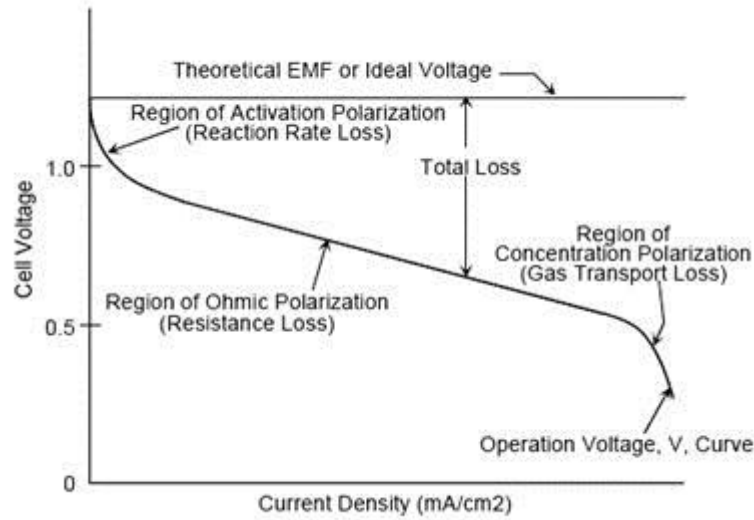


**Fig 1.5** Sources of Polarization as a function of current density

### 1.5.1 Activation Polarization

Activation polarization refers to the overpotential needed to change the activation energy of an electrochemical process occurring at an electrode. In order to accomplish this, an additional potential, an overpotential,  $\eta$ , is applied to lower the free energy of activation,  $\Delta G^{o\ddagger}$ . This potential provides a driving force such that when applied, the rate of the electrode reaction exceeds the spontaneous rate. This modified electrode reaction rate relates to the exchange current density,  $i_o$ , as will be derived below. Here, the free energy of activation,  $\Delta G^{o\ddagger}$ , is lowered from its reversible value by  $\beta\eta F$ , by applying an overpotential,  $\eta$ . The effect of this applied overpotential is that electrons become more abundant at the cathode and less abundant at the anode (the anode becomes an electron ‘sink’).

$$\Delta G_{\eta}^{\ddagger} = \Delta G^{o\ddagger} - \beta\eta F$$

Here,  $\beta$  is a charge-transfer parameter which depends on the symmetry of the energy barrier associated with activation in the reaction process and is assumed to be 0.5 for a one-electron process. The rate constant at equilibrium for standard potential,  $E^0$ , is given below,

$$k_0 = A \exp(-\Delta G^{0\ddagger} / RT) \exp(-\beta E^0 F/RT)$$

For a reaction differing from the standard potential, the expression is represented as below,

$$k_E = A \exp(-\Delta G^{0\ddagger} / RT) \exp(-\beta E F/RT)$$

The above equation can also be represented as shown below,

$$k_E = A \exp(-\Delta G^{0\ddagger} / RT) \exp(-\beta E^0 F/RT) \exp(-\beta \eta F/RT) \quad \text{where } E = E^0 + \eta$$

Therefore the above equation can be simplified as below which represents the rate constant of the electrochemical charge transfer process,

$$k_E = k_0 \exp(-\beta \eta F/RT)$$

In electrochemical reactions kinetics, the rates of the reaction are measured as currents and thus the activation polarization can finally be expressed by the following equation, where  $i_{\text{for}}$  is the net current density for the forward reaction,  $i_0$  is the exchange current density,  $[S]$  is the concentration of the reacting species,  $n$  is the number of electrons,  $\eta_c$  is the cathodic or negative overpotential and  $\beta_c$  ( $0 < \beta_c < 1$ ) is the symmetry factor associated with the cathodic (forward) branch of the reaction. The anodic (reverse) branch of the reaction can be derived in a similar way,

$$i_{\text{for}} = i_0 \exp(-\beta_c \eta_c F/RT) \text{ where } i_0 = n F k_0 [S]$$

### 1.5.2 Ohmic Polarization

The ohmic polarization,  $iR$ , of the cell mainly includes the electrolyte resistance, the contact resistances between cell components and the electrical resistances of electrodes and the current collector materials attached with the electrodes [3]. These combined resistances produce the ohmic polarization, also called the  $iR$  drop, which increases proportionally and linearly with current. The linear effect of ohmic polarization combines with the activation polarization region (a natural logarithmic increase) and the combined relationship becomes relatively linear in the Tafel region (to be described later), as can be seen in Fig 1.5.

### 1.5.3 Concentration Polarization

The concentration polarization,  $\eta_{cp}$ , of the cell is directly related to the limiting current,  $i_L$  by the following expression [4],

$$\eta_{cp} = (RT/nF) \ln (1 - i/i_L)$$

The limiting current takes effect and dominates the overall cell polarization in high current density conditions. The primary reason behind concentration polarization are the mass transport and diffusion effects which limit the current produced in the cell. The above phenomena is caused by concentration gradients near the active catalytic region of the electrode-gas phase interface, producing local potential differences between the bulk gas phase and the electrode surface. It can also be said that at such conditions, the reactants for electrochemical reaction are used up or depleted away at a faster rate than they can be supplied to the electrode surface by gaseous diffusion. This diffusion gradient effect is observed and pertinent in porous electrodes as in the case of SOFCs.

## 1.6 Equilibrium Thermodynamics of SOFC – The Nernst Equation

At equilibrium conditions, the thermodynamics can help to throw light on the electrochemistry of the process by well-established relations. It is understood and a well-known fact that for a particular chemical or electrochemical reaction, the product concentration can be related to the concentration of the reactants by the Gibbs free energy of the process under consideration. Thus if  $\Delta G^0$  denotes the Gibbs free energy of the reaction at standard conditions, the Gibbs free energy ( $\Delta G$ ) of the reaction in equilibrium state can be represented as,

$$\Delta G = \Delta G^0 + RT \ln (a_{\text{products}} / a_{\text{reactants}}) \quad \text{where } a = \text{activity of reacting or product species}$$

If there is an electrochemical reaction (oxidation or reduction) occurring at the electrode interface and there is an involvement of  $n$  electrons being transferred during the reaction, the Gibbs free energy of that half-reaction ( $M^{n+} + ne^- \leftrightarrow M$ ) can be deduced and related to standard electrode potential as follows,

$$\Delta G = -nFE^0$$

Adjusting both the equations and rearranging the famous Nernst equation is deduced [1-3],

$$E = E^0 - (RT/nF) \ln (\Pi a_{\text{reactant}} / \Pi a_{\text{product}})$$

The above equation was first developed in 1904. Here,  $F$  is the Faradays constant which has a constant accepted value of 96485 C/mol,  $R$  is the universal gas constant and  $T$  is the operating temperature in absolute kelvin. As explained before,  $E$  denotes the electrochemical potential under the specified conditions and  $E^0$  denotes the electrochemical potential under standard state conditions. The above relationship is expected to remain unchanged with time because the thermodynamics of a system only depends on the initial and final state, thus proving to be a very important relation in modern fuel cell electrochemical studies.

## 1.7 Research Motivation & Overall Structure of the Dissertation

Solid Oxide Fuel Cells have slowly and surely started to work themselves through well-established laboratory settings to full scale commercial environment. Companies across the world are devising and identifying new application areas in which their utility can be maximized also considering proper longevity and feasibility both in terms of technical and economic aspects. Stationary power general applications have been identified as the most potent area of interest. It is also important to look at other alternative fuels as possible choices in place of hydrogen to overcome some of the techno-economic issues and problems associated with the latter. Hence sophisticated techniques, protocols and procedures based on *in-situ* monitoring, State of Health (SOH) analysis and quantitative estimation are required to work in tandem for complementing each other. These efforts can help in carrying out the best possible system characterization for providing more accurate information on cell behavior which can definitely lead to better performing commercial devices. At this point it should be mentioned, with the use of alternative fuels and low temperature SOFC's arrives a few issues of cell degradation, on-line live cell performance monitoring or optimization of fuel conditions for best possible performance tracking. Extensive efforts have been carried out by microscopic studies but those are usually after the test is completed or a system is dead. Therefore, the motivation of the work arises from the need of the hour for better, new and live data testing methods and approach especially in SOFC systems.

This dissertation explores the performance of miniature button cells and sub-commercial scale SOFC stacks under various operating fuel conditions and characteristics. Both the systems have the same material composition thus making this research driven more towards performance characterization, degradation analysis and long term diagnostics. In a nutshell, the work is an effort to contribute towards worldwide efforts in analysis of the effects of changing fuel conditions on SOFC behavior through *in-situ* DC and AC electrochemical techniques. Both linear and non-linear

techniques are applied to understand the response of the fuel cell system with respect to the presence of inorganic impurities, determination of electro-kinetic parameters and other important fuel characteristics and parameters. In this work, we have also worked and demonstrated the application of a non-linear electrochemical technique for the first time in SOFC's which can effectively determine and monitor critical kinetic parameters of a system at a much faster rate with lesser complexities. We truly believe that this novel contribution towards fuel cell science and electrochemistry can help to enhance the proper assessment and monitoring of SOFC operation and performance. Better knowledge of the above mentioned aspects regarding fuel cell research is important to move forward in the road to commercialization of this exciting technological device.

The text, images and tables of chapters 3, 4 and 5 were originally prepared for peer reviewed journal publications encompassing the entire work. A summary of current literature relevant to the research and data will be presented in each of those chapters.

## References – Chapter 1

- [1] J. Larminie, A. Dicks, Fuel Cell Systems Explained, 2nd edition, Wiley, 2003.
- [2] J.R. Macdonald, Impedance Spectroscopy Emphasizing Solid Materials and Systems, New York, NY: John Wiley and Sons, 1987.
- [3] Bard, Faulkner, 2nd ed, Electrochemical Methods: Fundamentals and Applications, Wiley, 2001.
- [4] K. Huang, J.B. Goodenough, “Solid Oxide Fuel Cell Technology”, September 2009.
- [5] S. Singhal, A. Virkar, “High Temperature and Solid Oxide Fuel Cells”, 2003

## Chapter 2

---

### Instrumental & Experimental Descriptions

#### 2.1 Button Fuel Cell Setup & Stack Assembly

The fuel cell testing setup was constructed with great care. A SOFC system is a high temperature system composed of primarily ceramic materials thus making it an easy candidate for mechanical damage. Thus additional attention has been given towards this aspect of cell assembly. A picture of the button cell and the diagrammatic schematic of the setup is shown in Fig 2.1 & Fig. 2.2 respectively. A custom made stainless steel ultra-torr fitting was used to seal the alumina tubes used for the fuel gas supply and also used as a support for the button cell assembly inside the furnace. The button cell was fixed at one end of the alumina tube by a glass seal to keep the fuel and the oxidant chambers separate. The diameter of the button cell used was 1 inch (25.4 mm). An alumina cap was used along with the glass ring seal on one end of the alumina tube to improve the mechanical stability of the button cell-alumina tube arrangement by preventing any handling damages to the fragile button cell electrode assembly. Electrical leads composed of Pt (0.2 mm diameter, Alfa Aesar©) and Ag (0.25 mm diameter, Alfa Aesar©) were used to carry the electrical currents across the fuel cell electrodes and also for electrochemical measurements. Pt was used as leads directly attached to the electrode surfaces (anode and cathode) and Ag wires were used to connect the Pt wires to electrochemical instruments for data acquisition. Pt due to its higher stability, heat resistance and inert nature was used on the electrode surface. But as Pt is expensive, it was not used to form the entire length of the current carrying leads. Thus Ag being cheaper having similar electrical characteristics was used in conjunction with Pt. All leads were electrically insulated from each other as well as from the Faraday cage and furnace components. To check that all leads were isolated, a handheld voltmeter was used to verify that the resistance between each

of the leads was ‘infinitely’ high. All measurements were carried out between 650 C and 850 C. A K-Type thermocouple was strategically placed near the working electrode to monitor the actual temperature during testing. It was also used to detect leaks readily in the button cell assembly because if there was a leak the temperature detected in the thermocouple would flicker a lot and would be unstable. The furnace used was a vertical tubular furnace (Barnstead Thermolyne) where the temperature was ramped from room temperature to 900 C at a rate of 1 C min<sup>-1</sup>, kept there for an hour and then reduced at a higher rate of 2 C min<sup>-1</sup> to the operating temperature under consideration. This was done to melt the glass rings, vitrify them to make the seal more robust and as efficient as possible.



**Fig. 2.1** (Left) Anode surface, (Right) Cathode surface in black with an interlayer white electrolyte

The SOFC stack setup was different from the button cell setup. While the button cell was a miniature circular cell of diameter 2.5 cm<sup>2</sup>, the SOFC stack composed of a 5 cell planar integrated system with 105 cm<sup>2</sup> surface area. The short stack system was an integrated robust system which had dedicated fuel/oxidant lines and electrical leads. Thus it was only important in this case to use a box furnace (Sentrotech Inc.) with proper size considerations and provisions for fuel and oxidant lines for coming in and out of the system. Because the scale of the stack system was larger, proper hoses were used for supplying the necessary gases and also thicker copper wires with higher power rating were used to carry the current generated across the system and for electrochemical measurements. Additionally, due to the extremely high gas flows (and their explosive nature) used

in stack tests, proper exhaust lines were also built around the system to make sure that the working environment was safe enough. A schematic and pictures of the stack testing setup is shown in Fig. 2.3 and 2.4 respectively.

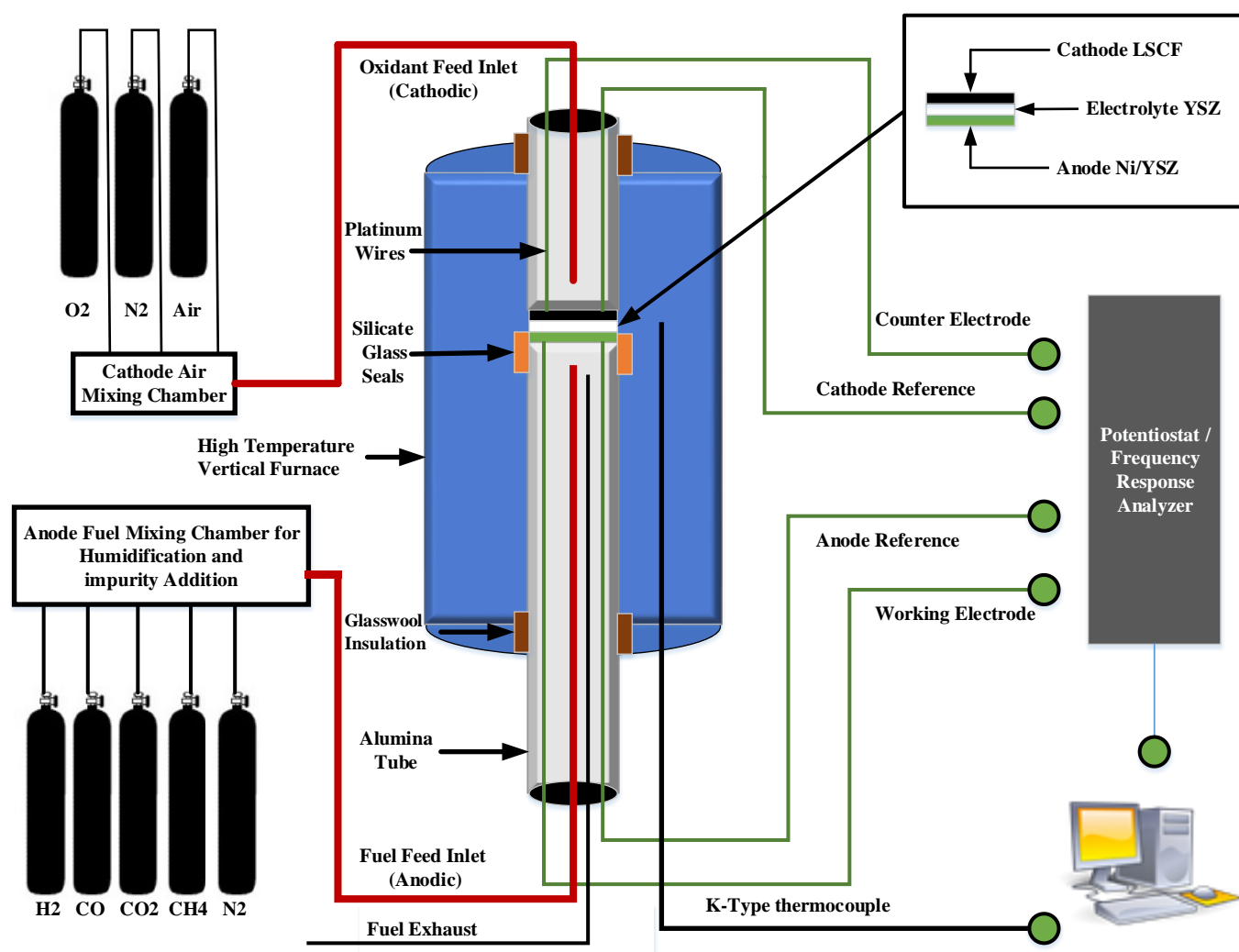


**Fig 2.2** A detailed schematic of the SOFC button cell test arrangement

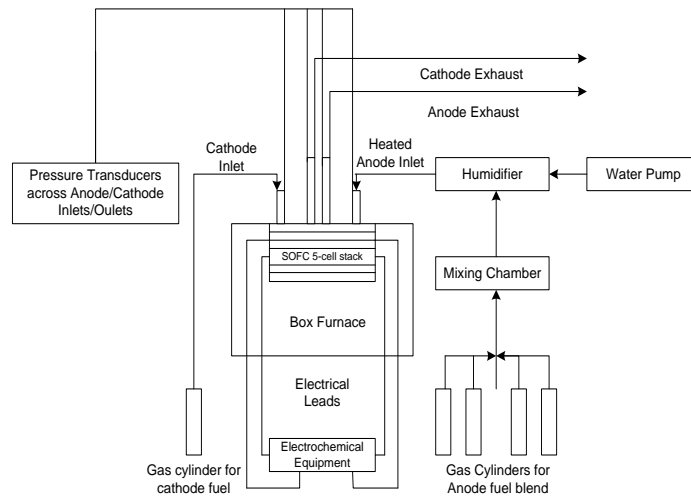


**Fig 2.3** A simplified schematic of the SOFC stack testing setup

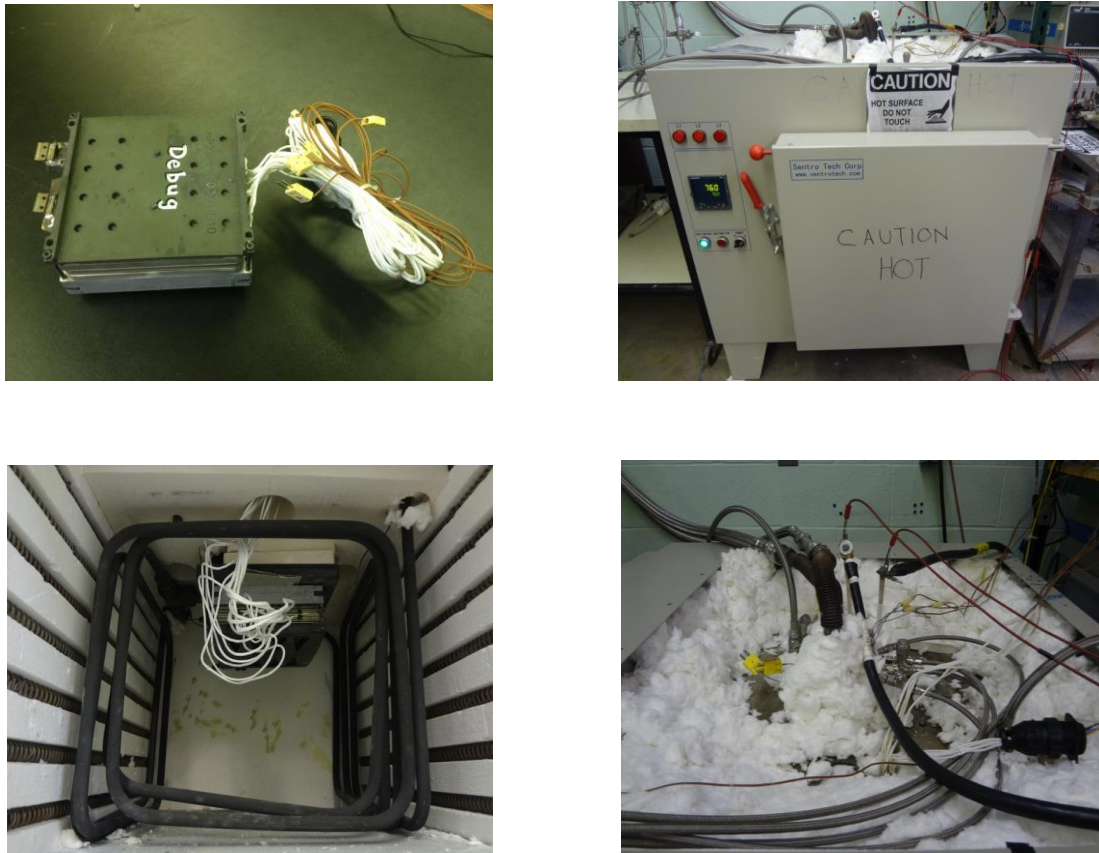


**Fig. 2.4** (Top left) Delphi Gen 3.2 a 5-cell stack, (Top Right) Box furnace with stack installed, (Bottom left) Stack and manifold inside the furnace (Bottom Right) Electrical & gas connections from furnace top

## 2.2 Button Cell Membrane Electrode Assembly (MEA)

The button cell MEA is very important for getting high quality, consistent and repeatable data. In our work, the button cell was provided by Delphi Automotive Systems. The cell architecture consisted of a 30  $\mu\text{m}$  Lanthanum Strontium Cobalt Ferrite (LSCF) cathode, 10  $\mu\text{m}$  Yttria-Stabilized Zirconia (YSZ) membrane (electrolyte) and a 500  $\mu\text{m}$  Ni/YSZ anode. Detailed information regarding cell fabrication, composition and properties have not been provided in lieu of the intellectual property rights. The electrical circuit as explained before was completed using Pt wires of similar diameters. The ability to collect current reliably is crucial to accurate fuel cell operation and data collection. Electrode behavior cannot be reliably determined if this component of the fuel cell is not optimized. Ideal characteristics of the proper current collector are important. Chemical stability in a reducing and oxidizing environment ensures that the material chosen does not itself undergo chemical reactions before or during electrochemical measurements, thus ensuring that differences in numerical data output are due only to the electrode processes themselves. Furthermore, current constriction is a parameter of concern: the current produced by the electrode should be collected in its entirety, and should not be subject to any constriction restrictions. Proper contact between the electrode material and the current collector will ensure this is not a problem. Two prevalent types of current collector can be found in the literature: paste and mesh. Although paste can both be easily painted onto an electrode and ensure reliable current collector-electrode contact, it has been shown to lose proper contact during long term operation. Therefore, a mesh current collector was also chosen to avoid this degradation. Contact resistance was also minimized by employing this method of electrode manufacturing. Considering all the above factors, a combined mesh and paste current collection system was used in our work. Ni mesh with Ni paste (Fuel Cell Materials Inc.) was used in the anode and Ag mesh with Ag/Pd paste (Alfa Aesar©) as current collector materials. The entire MEA was then carefully fixed on the alumina tube arrangement as described earlier.

## 2.3 Fuel & Oxidant Arrangements

All the gaseous components of the fuels ( $\text{H}_2$ ,  $\text{N}_2$ ,  $\text{CO}$ ,  $\text{CO}_2$ ,  $\text{CH}_4$ ) were purchased from Praxair at the industrial grade purity. The gaseous fuels were used “as is” and also before starting any experiment, the fuel lines were purged for 15 minutes to ensure that the purity in the line was acceptable. For mixing purposes, a home-made gas manifold was constructed which allowed all the gases to reach the chamber before being dispersed to the inlet of the fuel cell system. Water was supplied to the system by a home-made vaporizer unit which was simultaneously joined with the gas manifold system. The input lines from the manifold till the fuel cell inlet was wrapped with heating coils and kept at  $200\text{ }^\circ\text{C}$  to avoid any condensation into the inner walls of the tubing. For poisoning tests, the corresponding inorganic impurities were added to the fuel stream and their concentrations levels were adjusted. Gaseous impurity was added directly to the mixing chamber and liquid impurities were added by bubbling inert  $\text{N}_2$  gas through them. Due to the presence of a lot of toxic and explosive substances, alarms were kept at key locations around the experimental setup to detect any undesirable situations because of leaks or other unwarranted factors. Due to its availability air was used as the most standard oxidant in the electrochemical tests. Some tests were carried out with pure oxygen for analysis purposes. Finally, due to the fact that relative performances were emphasized over absolute performance values, the amount of polarization associated with the cathode has lower importance. Therefore, only changes associated with anode characteristics are of importance in this work.

## 2.4 DC Electrochemical Characterization

DC testing of solid oxide fuel cells mainly includes Linear Sweep Voltammetry (LSV) and Polarization curves. In general DC electrochemical techniques have been conventional methods for preliminary fuel cell performance analysis. They give a nice indication about the fuel cell polarization behavior and the interdependencies between potential & current. *I-V* (Current-

potential) and *P-I* (Power-Current) curves gives information on the initial performance of a fuel cell under standard conditions which help in directing future test plans in fuel cell research. LSV is also a well-established technique which is good for estimating and comparing the thermodynamics, kinetics, and mechanisms of various fuel cell reactions. In LSV the potential of a fuel cell is scanned at a definite rate normally in the order of  $\text{mV s}^{-1}$  from the Open Circuit Potential (zero current potential) to a certain overpotential value. In this work, DC measurements have been carried out with a Solartron<sup>®</sup> 1470 E potentiostat and also a HP 6060B electronic load. Due to a current limit of 4 A on the potentiostat, the electronic load was used when high current load requirement was necessary. In short, DC techniques are standard tests for fuel cell evaluation.

## **2.5 Electrochemical Impedance Spectroscopy (EIS)**

EIS is a powerful linear electrochemical perturbation AC technique which is used for investigating reaction pathways, failure modes and degradation mechanisms in complex fuel cell processes [1-3]. It also helps to explore the properties of electrode materials in certain cases. The primary purpose which it serves is that it is used to separate and distinguish various processes occurring in different time-scales. This characterization technique has been used in fuel cell research [] for identifying the contributions from ohmic, activation and concentration polarization in a definite frequency range. But simple qualitative analysis might make data interpretation difficult at times. For this reason, EIS should be complemented with Equivalent Circuit Modeling (ECM) to give an idea regarding the quantitative side of the overall information. ECM is defined as the arrangement of electrical circuits and elements in plausible combinations (network of series and parallel elements) to model the actual behavior observed in EIS data applied on electrochemical systems. The method consists of physically relevant circuit elements with Complex Non-Linear Squares (CNLS) data fitting [2] combined with an assessment of the stochastic error structure, to make it a consistent and valid simulation procedure.

EIS primarily involves a small amplitude AC potential perturbation on the electrochemical system under consideration. The small potential signal can be in the form of  $A\sin(\omega t)$  where  $A$  is the amplitude and  $\omega$  is the frequency. As a result of the potential input, there is a sinusoidal current response with a phase shift ( $\phi$ ) with a different amplitude. Therefore the current response and the potential input can be used to determine the complex impedance ( $Z$ ) arising from the system from Ohm's law (resistance term replaced with impedance in the relation). At this point it is also important to mention that in real world applications, the word "resistance" is replaced by impedance because of the inherent non-linear nature of practical electrochemical systems. Thus to apply the concept of Ohm's law in EIS, a smaller amplitude is considered which make the perturbation and the response pseudo-linear. It can also be understood well from the Fig. 2.5. A complete EIS plot consists of a frequency sweep in a definite range and the various time-scale dependent impedances such as ohmic, charge-transfer (activation) and diffusion (concentration) are displayed in the graph. A faster process such as ohmic losses occurs at high frequency and mass transfer effects which are slower processes occur in low frequencies. A conventional EIS plot is called a Nyquist plot or a Cole-Cole plot.

Therefore three most important factors to be considered while considering EIS data [2-4] are,

1. Causal – The current response is only caused by the potential perturbation.
2. Linear – The amplitude of the input should be small to give a linear output.
3. Stable – There should be no or minimum drift or background noise in the current response

After the acquisition of an impedance plot and before applying circuit modeling, it is also important to check for the validity of the obtained data for the above three conditions to be fulfilled. The data then can be termed consistent and valid. Kramers Kronig (K-K) transform [1,2] are established relations [] which serve as an internal check on the validity and quality of the data. The

K-K relations state that the real part of the impedance data can be obtained by an integration of the imaginary part and vice versa. If the above three conditions are maintained for any EIS data, it can be safely said that the K-K transform relations will hold well. If in any case, the real and imaginary part of the data do not conform well to K-K transformations, it can be inferred that the data obtained is not valid and cannot be considered for further ECM data treatment. Thus K-K analysis of the impedance data is always important and serves as a useful check before understanding of physically relevant models to EIS plots.

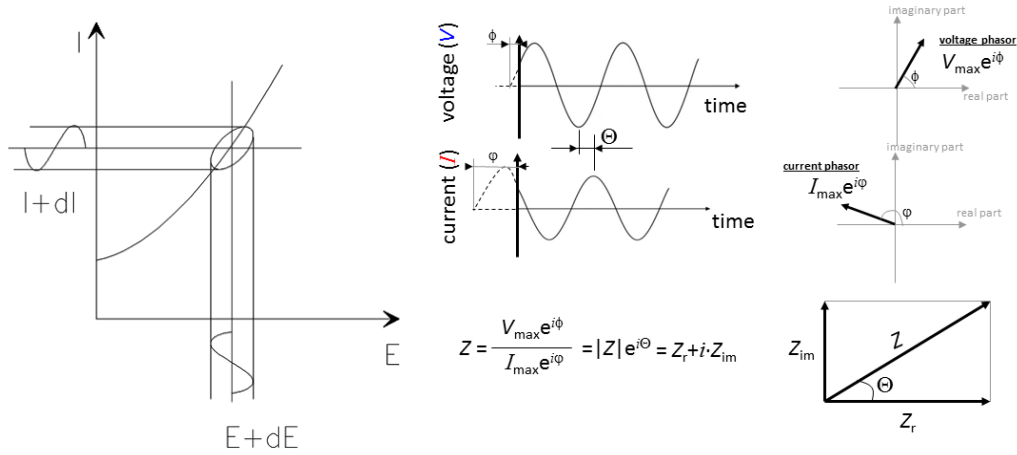


**Fig. 2.5** (Left) Small amplitude of input potential perturbation producing a pseudo-linear current response (Right) Mathematical treatment for the input-response impedance data showing the phase shift  $\phi$ . Complex impedance is written and can be plotted in the form of real and imaginary part.

## 2.6 Equivalent Circuit Modeling (ECM)

As mentioned before, ECM gives both a qualitative and quantitative perspective of the impedance data which helps to understand the electrochemical processes and their behavior in a much better way [2]. It is important in the sense that after proper validation of the EIS data, ECM can be used to associate physically meaningful parameters to the impedance of the system. These parameters can be simple electrochemical parameters or complex parameters derived from first

principles and established chemical reaction models. Therefore it gives adequate information on the process parameters such as diffusion coefficient and reaction rate constant etc. In short, it adds an analytical interpretation to the overall process investigation technique by EIS.

The circuit models are constructed using three primary elements: ideal resistors (R), Capacitors (C) and inductors (L). Since real world systems rarely behave ideally, specialized circuit elements are also used as well namely the constant phase element (CPE), Warburg element (W), Gerischer element (Ge) etc. The main parameters are described below.

### **Resistors**

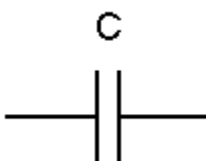
For an ideal resistor element (R), it is represented by the symbol shown in Fig. 2.6. The impedance of a resistor is independent of frequency and has no imaginary component. The current through a resistor stays in phase with the voltage across the resistor ( $\phi = 0$ ). It can be thus related by Ohm's law as below.

$$Z_r = E/I = R$$


**Fig. 2.6** Representation of an ideal resistor

### **Capacitors**

For an ideal capacitor (C), it is represented by the symbol shown in Fig. 2.7. A capacitor's impedance decreases as the frequency is raised. Capacitors also have only an imaginary impedance component. The charge  $q$  stored in the plates of the capacitor relates to the potential across the plate.

$$q = CE$$


**Fig. 2.7** Representation of an ideal capacitor

The relation which describe the impedance of a capacitor is represented as below,

$$E = -j (1/\omega C) I$$

Here the term  $-j (1/\omega C)$  is equivalent to  $R$  and is also frequency and capacitance dependent.

### **Series R-C circuit**

When the above two phase elements are placed in series, an equivalent circuit model for an ideally polarizable electrode is obtained as shown in Fig. 2.8. The total potential drop in this circuit is the sum of the resistive and capacitive elements. Thus from the previous relations, a complex notation can be obtained which can be expressed in the form of a sum of real and imaginary component.

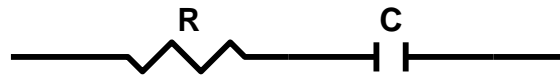


**Fig. 2.8** Representation of a series R-C circuit

The above impedance can be graphically interpreted and plotted which is named the Nyquist Plot as shown in Fig. 2.9. In such a plot, the real component of the impedance is graphed as a function of the imaginary component. In this relation, the real component is not dependent of frequency and the imaginary component tends to zero with an increase in frequency.

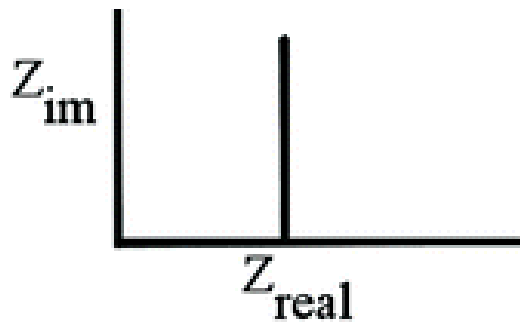


**Fig. 2.9** Representative Nyquist plot for an ideally polarizable electrode

### Parallel R-C circuit

For a real world systems, which involves both capacitive and faradic currents, the parallel R-C circuit can be represented as shown in Fig. 2.10. Such Nyquist plots are most regularly seen in actual electrochemical systems.

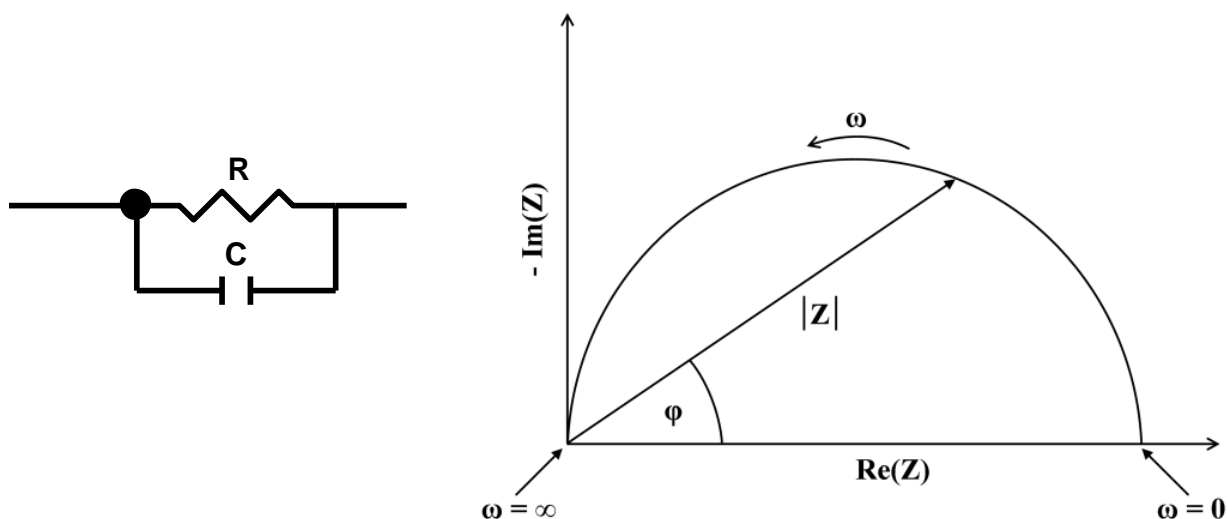


**Fig. 2.10** (Left) Representation of a parallel R-C circuit (Right) Representative Nyquist plot for a real world polarizable electrode

Based on the impedances of the individual impedances of the elements, the total impedance can be similarly calculated quantitatively by using conventional circuit laws for series and parallel formations. In real world applications there is also an associated ohmic resistance with electrochemical systems. In such a case the circuit models comprises of another simple resistor element in series with one shown in Fig 2.10 and the Nyquist plot gets shifted in the positive x axis direction by the value of the ohmic resistance. A representation is shown in Fig 2-11. Here  $R_\Omega$  represents the ohmic resistance,  $R_t$  the charge transfer resistance arising from activation related processes and  $C_{dl}$  is the double layer capacitance in the electrode interface.

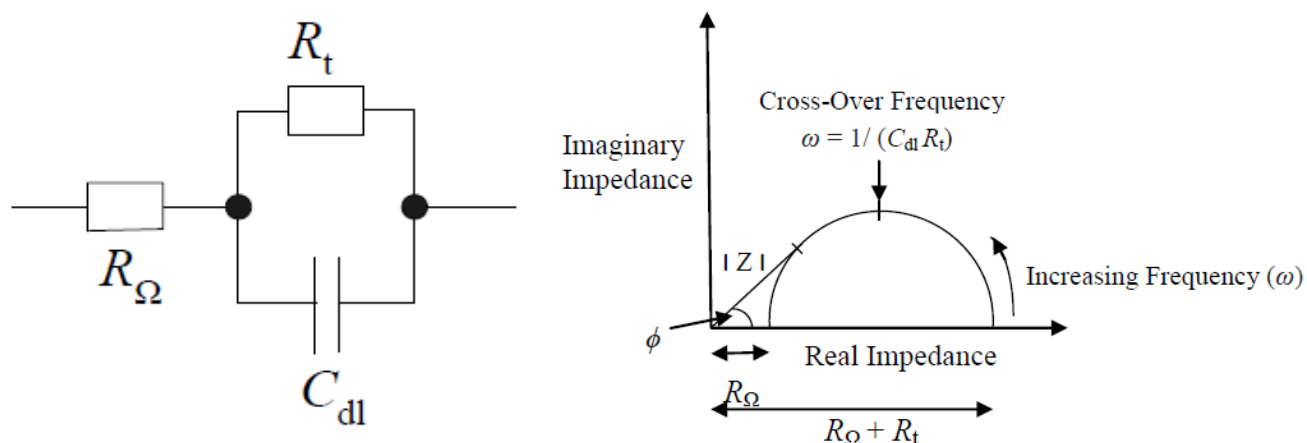


**Fig. 2.11** (Left) Representation of a parallel R-C circuit with a series ohmic resistance (Right) Representative Nyquist plot for a real world polarizable electrode

### Constant Phase Element (CPE)

This element is analogous to capacitors and is mostly encountered in solid state electrochemical systems. A CPE element mainly is represented in the form of a depressed semi-circle arc (different from a conventional capacitor which is a regular semi-circle) which has its center below the real impedance x-axis. The center is located at an angle of  $(1-n) 90^\circ$  as measured from the origin, where  $n$  is the depression parameter. The  $n=1$  case corresponds to an ideal capacitive element. A representative Nyquist plot for a CPE is shown in Fig. 2.12.

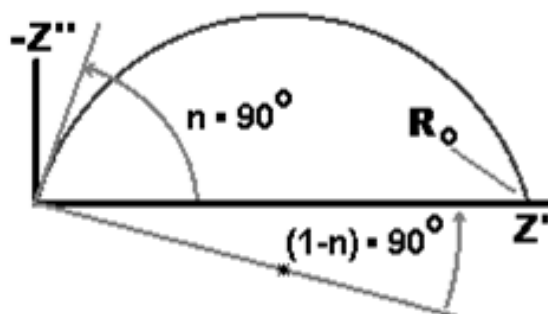


**Fig. 2.12** Representative Nyquist plot for a CPE element in the form of a depressed semi-circle

The CPE element mainly indicates surface roughness of the system which also may arise from high distributed reaction rates, varying thickness or composition of the electrode and non-uniform current distribution. The anode of a solid oxide fuel cell is generally porous and due to its fabrication nature, it is expected that there will be regions on the catalyst which have different energy of activation. Thus electrochemical oxidation reactions occur differently at different rates across the anode surface which gives rise to a CPE behavior. Also due to various current collector materials (mesh and paste) used in a SOFC in a home-made environment, various “edge effects” also creep in which increases the variation in current across the entire surface. Under such an effect, the current at the center of the active area may be lesser than the edge which increases the overall surface roughness factor of the system under test. Because of the above reasons, a commercially built robust fuel cell stack setup shows mostly capacitive behavior and home-made non-uniform cells indicate constant phase element behavior.

### **Warburg Element**

Bulk diffusion in electrochemical systems is also another important component of the global impedance in real world systems. The Warburg impedance ( $Z_w$ ) is a specialized element which dominates in low frequencies because then, the reactants have to diffuse further but is absent in high frequency regions when the reactants do not diffuse due to shorter time-scales [2,4]. On a Nyquist plot as shown in Fig. 2.13, it appears ideally as a line with a slope of 0.5 or at an angle of 45 with respect to the x-axis. The Warburg or Diffusion impedance is quantified and derived from the Fick’s first law of diffusion and it gives information on important physical parameters such as diffusion coefficient and diffusion layer thickness.

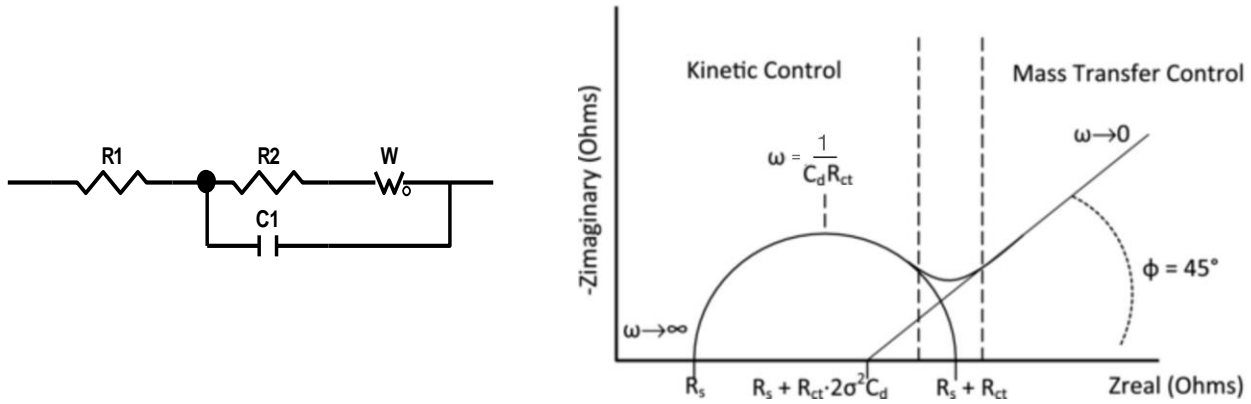


**Fig 2.13** (Left) Representation of a Warburg element with a parallel R-C circuit (Right) Representative Nyquist plot for a Warburg element showing mass diffusion behavior

### Circuit Obscurity & Fitting Algorithms

Even though EIS is a powerful technique in conjunction with ECM, it has an important drawback. At certain circumstances, the circuit models could be possible non-unique and multiple models could fit a single particular Nyquist plot. Thus it becomes even more important as a researcher to initially understand the physical nature of the system, its possible reaction schemes and then try to relate a definite model to an impedance data. *Ab initio*, after understanding the fundamentals of the system, it is a good practice to choose simplified circuits to initiate system modelling. Complex and specialized circuits can then be introduced into existing models to simulate the behavior in a much better way both in terms of fitting and also valid conceptual reasoning.

ZView is the software used for the fitting of the impedance data to equivalent circuit models. The software uses the conventional complex nonlinear least squares (CNLS) method [2] which is one of the most popular techniques to fit experimental data. To improve the efficiency of the CNLS fitting the chi squared ( $\chi^2$ ) algorithm was used. A smaller value of the  $\chi^2$  indicates a better statistical fit to the considered circuit model. The CNLS method considers and assumes the fact that the experimental impedance data consist of only Gaussian errors. Any different kinds of errors

could result in a reduction of the goodness of the fit. The CNLS procedure uses a convergence technique where the algorithm may stop at a “local minimum”, characterized by a large  $\chi^2$ . In such circumstances, the initial guessed value of the various parameters in the model should be tinkered around and also selective parameters should be changed from free to fixed or vice-versa.

### **EIS Instrumentation**

The EIS data and Nyquist plots are obtained by a Solartron® 1252 A Frequency Response Analyzer in conjunction with a Solartron® 1470E potentiostat. The fuel cell system is swept in a definite frequency range and the software connected to the Solartron systems acquire and plot the data during acquisition. A frequency response analyzer uses Fourier Transformation [1-3] to convert the frequency domain measurements to time domain. A detailed schematic is shown in Fig. 2.14.

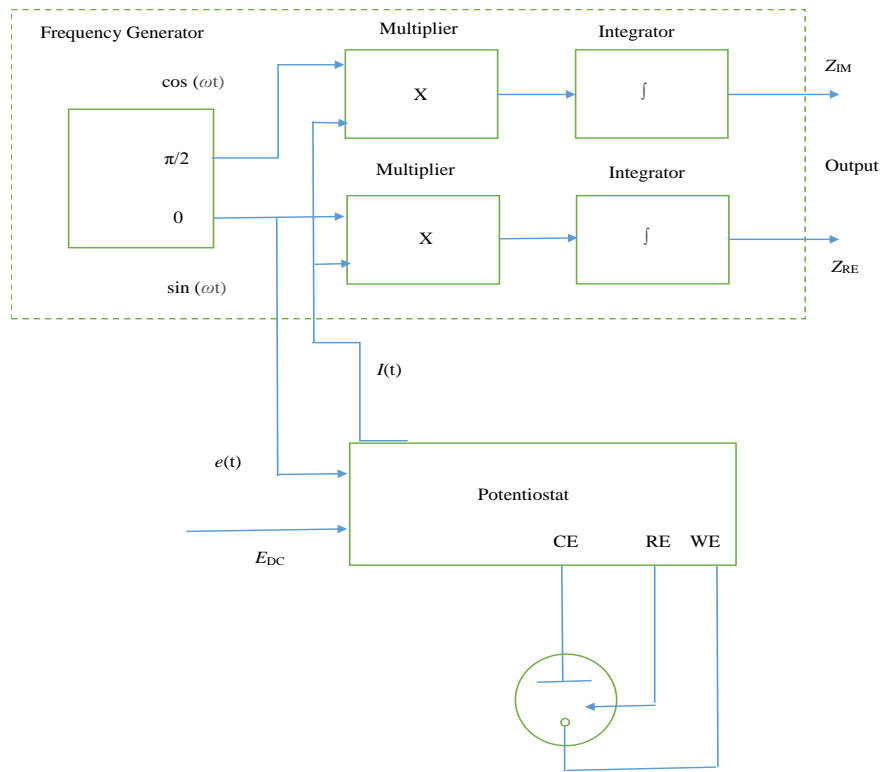


**Fig 2.14** Diagram illustrating the working principle of the FRA for an EIS measurement. CE – Counter Electrode, RE – Reference, WE – Working,  $Z_{IM}$  &  $Z_{RE}$  – Imaginary & Real impedance

## 2.7 Electrochemical Frequency Modulation (EFM) – A new technique used in SOFC

This is a new introductory AC technique [6] used for the first time in fuel cell applications. EFM has been used extensively in corrosion systems and is a very useful non-linear, non-destructive electrochemical technique which can be used for estimation of intrinsic kinetic data. EFM consists of potential perturbation of the system by two sinusoidal waves of different frequencies which results in a non-linear current response of the electrochemical system. A graphical representation of the basic operational concept is shown in Fig. 2.15. It can serve as an effective complementary technique to conventional electrochemical characterization methods. The reason for the above statement being the fact that it is a faster *in-situ* technique and the necessary electrochemical kinetic parameter values can be directly obtained from the observed data by proper preliminary model consideration. The background concepts, theory and advantages of the technique are explained in a separate chapter later in the dissertation.

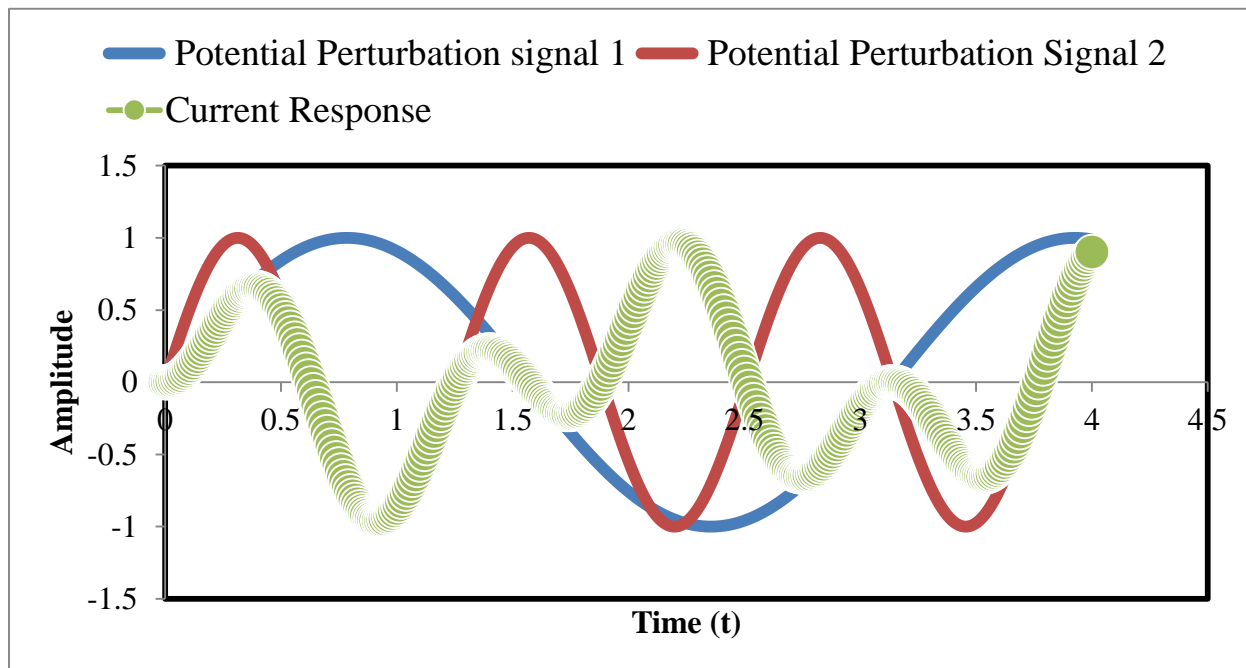


**Fig 2.15** A simplified representation of the EFM concept

## References – Chapter 2

- [1] J. Larminie, A. Dicks, Fuel Cell Systems Explained, 2nd edition, Wiley, 2003.
- [2] J.R. Macdonald, Impedance Spectroscopy Emphasizing Solid Materials and Systems, New York, NY: John Wiley and Sons, 1987.
- [3] Bard, Faulkner, 2nd ed, Electrochemical Methods: Fundamentals and Applications, Wiley, 2001.
- [4] K. Huang, J.B. Goodenough, “Solid Oxide Fuel Cell Technology”, September 2009.
- [5] S. Singhal, A. Virkar, “High Temperature and Solid Oxide Fuel Cells”, 2003
- [6] R.W. Bosch, J. Hubrecht, W.F. Bogaerts, B.C. Syrett, Corrosion, 2001

## Chapter 3

---

### Impedance Spectra Effects in Solid Oxide Fuel Cells Operating on Alternative Fuel Reformate Streams poisoned by Inorganic Impurities

This text for this chapter was originally prepared for the *Journal of Electrochemical Society Transactions* as “Subtraction Impedance Spectra Effects in Solid Oxide Fuel Cells Operating on Alternative Fuel Reformate Streams poisoned by Inorganic Impurities”; **Debanjan Das**, Serguei N. Lvov. The paper was accepted for publication in ECS Meeting, San Diego (June 2016)

#### Preface to Chapter 3

Poisoning effects by three inorganic impurities on the performance of a solid oxide fuel cell are tested, analyzed and compared by applying electrochemical impedance spectroscopy (EIS) and equivalent circuit modeling (ECM). A series impedance subtraction method was applied on the tested cells to account for only the degradation occurring in the cell anode due to impurities. Due to the fact that the respective SOFC electrodes and electrolyte are connected in series in an electrochemical circuit, cell performance change can be attributed to the anode in this approach. Degradation of the cell performance caused by inorganic impurities is characterized by measuring EIS spectra at a constant current density of  $0.3 \text{ A cm}^{-2}$  for a diesel fuel reformat blend. The concentrations of impurities are selected in accordance with the levels expected after commercial biogas or diesel fuel cleaning processes. Critical electrochemical processes and degradation mechanisms which affect cell performance are identified and quantified. The impurities tested are sulfur, chlorine and siloxane at various ppb/ppm levels over a time period of 200-300 h. Sulfur and siloxane cause the most prominent degradation and the associated best fit electrochemical cell

parameters, Gerischer and Warburg elements, are applied respectively for better understanding of the degradation processes.

### **3.1 Introduction**

The interest in the determination of the effects of impurities and contaminants in solid oxide fuel cells (SOFCs) has received much attention in recent years among researchers due to the plausibility of utilizing reformed natural gas as a direct fuel in SOFC anodes [1-12]. Important and notable work has been carried out to study the microstructural degradation based on visual microscopy techniques and x-ray data interpretations [3, 10-12, 20], and to understand qualitatively the impact of anode degradation on the impedance evolution under the presence of various contaminants. EIS is a powerful technique to understand, identify and distinguish the different chemical/electrochemical processes occurring in the fuel cell under the presence of various undesirable substances. Concerted efforts have been made to study the various arcs obtained in a typical EIS spectra. The low frequency behavior is attributed to the diffusion or mass-transfer controlled processes and the high frequency arc pertains to the charge-transfer process [4-7, 16, 22-26]. However, EIS alone is only useful to a certain extent. To extend the utility and effectiveness of EIS, it should be combined and complemented with the equivalent circuit modelling to analyze the processes in a qualitative and quantitative way. Therefore, there is a need to apply suitable and specific electrochemical models based on obtained EIS spectra with various inorganic impurities to optimize the fuel cell system operation in practical and commercial systems to achieve stable operation and maximum fuel efficiency [26].

In biogas or digester gas there are also other inorganic impurities such as sulfur, halogens, siloxane and phosphorus present which may have harmful effects on the performance of a SOFC.

Biogas may contain higher part per million (ppm) levels of chlorine and siloxane, which may negatively influence the fuel cell performance. Sulfur has been studied the most in detail which also focused on poisoning effects of sulfur on shift reactions [4-8]. Work on siloxane and chlorine, two prime impurities in biogas have been rather limited [2-3, 12] even though the authors have discussed possible mechanisms mainly from microscopy approach. Even though studies with relation to poisoning phenomena is a topic of intense research, there is a need for identifying applicable electrochemical models and using it in Equivalent Circuit Modeling (ECM) in conjunction with EIS on poisoned SOFC systems.

In this work, the impedance spectrum subtraction method is applied to identify and analyze the exclusive effects of the individual impurities on the SOFC [25]. It is understood that it is very difficult to separate electrode contributions in a SOFC, thus if there are changes occurring in one particular electrode in the cell, a subtraction spectrum provides an alternative way to identify the effect caused by the corresponding change in fuel conditions provided other conditions remain same. The above concept arises from the fact that the anode, electrolyte and the cathode of a SOFC are connected in series, if the overall electrochemical circuit is considered. Therefore a series subtraction of the cell parameters in ECM at two different time-scales can be used to quantify the causal effect of the parameter changed during the test. In this case, the changing parameter are the various concentration levels of the three impurities tested (sulfur, siloxane and chlorine). The effects of impurities are only manifested in the anode thus it is a useful way to relate anodic degradation phenomena to impurity effects. A systematic variation of the impurity levels coupled with well-reasoned subtracted EIS spectra and EFM models help to pin-point the corresponding nature of the poisoning effects. To our knowledge, this approach has not been extensively applied for impurity studies on SOFCs and this is an effort to do the same. This paper therefore aims to contribute to the overall degradation studies of SOFC technology by complementing the microstructural and optical investigations in the past and present. No optical microscopy

investigations were performed on the cells as this work mainly concentrated to increase the effectiveness of electrochemical impedance measurements and relate them to poisoning studies through microstructural characterization done by other researchers in the past.

## **3.2 Experimental**

### *3.2.1 Anode Supported SOFC Button Cell*

In this study, the solid oxide fuel cells were miniature button cells provided by Delphi Automotive, LLC, Michigan [27,28]. The button cells used in the work were provided as a part of a project to test the possibility of working with full commercial SOFC stacks with different alternative reformates fuels and inorganic impurities. The cell architecture consisted of a 33  $\mu\text{m}$  Lanthanum Strontium Cobalt Ferrite (LSCF) cathode, 10  $\mu\text{m}$  Yttria-Stabilized Zirconia (8YSZ) membrane (electrolyte) and a 515  $\mu\text{m}$  Ni/YSZ anode. The entire anode layer consisted of three sub layers tape-casted which comprised of an active anode in contact with the electrolyte (10  $\mu\text{m}$ ), an anode support functional layer (500  $\mu\text{m}$ ) and a contact layer (5  $\mu\text{m}$ ) on the top. The electrolyte layer was also fabricated using the tape-casting. The cathode also consisted of a bi-layer comprising of an active screen-printed cathode (30  $\mu\text{m}$ ) along with an outside cap layer (3  $\mu\text{m}$ ). The cells were operated at temperatures of 750 °C and a 2-electrode 4-lead system was used to perform the electrochemical measurements on the cells. Two electrode leads were attached on each electrode surfaces, therefore resulting in current being carried by one set while the other set was used for measuring potential. This arrangement helped in obtaining consistent EIS data by preventing the passage of current in voltage leads such that the correct potential could be measured against the reference potential lead. For proper current collection, Ni paste was used along with a Ni-mesh and fixed onto the anode. Ag/Pd paste was used with a Ag screen mesh fixed onto the cathode side. Four platinum electrode leads were pasted on the electrode surfaces (two on each

electrode) which served as voltage and current leads for electrochemical measurements. . All calculations were performed considering the geometric active cell area of  $2.5 \text{ cm}^2$  which was measured by a Vernier caliper. A schematic of the experimental setup is shown in Fig. 3.1a.

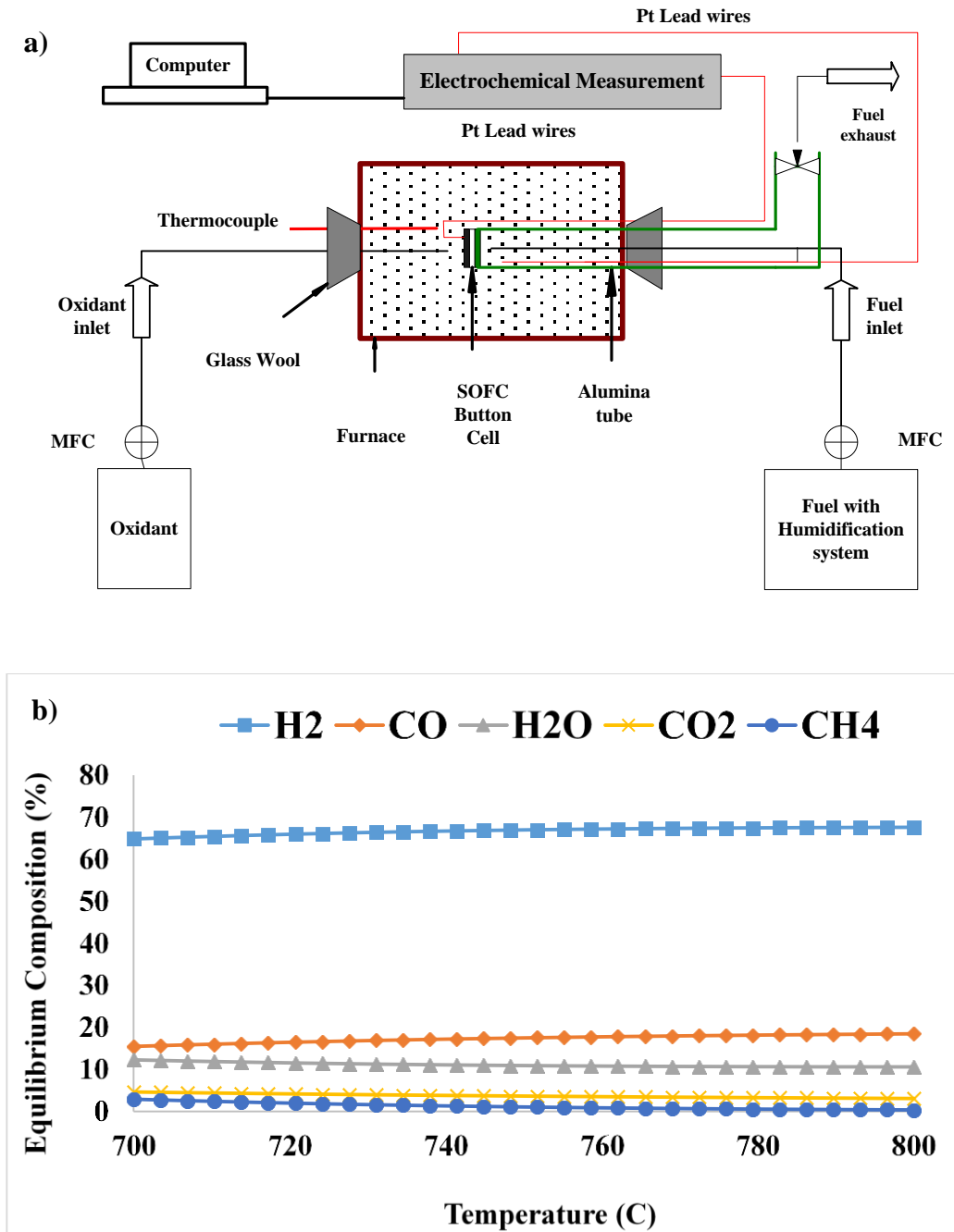


**Fig. 3.1 (a)** A schematic of the experimental setup **(b)** Equilibrium composition diagram of the fuel feed with respect to the operational temperature.

### 3.2.2 Electrochemical Testing

Before actual testing, the anode of the button cells were reduced by supplying a 5 %  $\text{H}_2$  – 95 %  $\text{N}_2$  gas blend at a flow rate of  $1 \text{ L min}^{-1}$  for 2 h. The temperature of the furnace (a vertical Barnstead Thermolyne tubular furnace) was increased at a rate of  $1 \text{ }^\circ\text{C min}^{-1}$  from room temperature to the required value of  $750 \text{ }^\circ\text{C}$ . The slow heating rate was used to make sure that no cracks developed in the cell structure due to thermal and mechanical stress, which might be a problem in the case of button cells. The anode fuel feed was a simulated diesel reformat mixture consisting of 10 %  $\text{CO}_2$ , 3 %  $\text{CH}_4$ , 10 %  $\text{CO}$ , 7 %  $\text{H}_2\text{O}$ , 70 %  $\text{H}_2$  at a flow rate of  $0.5 \text{ L min}^{-1}$  and air at a flow rate of  $1 \text{ L min}^{-1}$  was supplied as the oxidant to the cathode. The steam-to-carbon ratio (S/C) was maintained at a suitable level around 2.5 ~ 3 to avoid or minimize any possibilities of carbon deposition during the operation of the fuel cell at high temperatures. The equilibrium gas composition was estimated as 3.66 %  $\text{CO}_2$ , 1.08 %  $\text{CH}_4$ , 17.4 %  $\text{CO}$ , 10.9 %  $\text{H}_2\text{O}$  and 66.9 %  $\text{H}_2$  as shown in Fig. 3.1b. The Nernst potential for the above equilibrium blend was calculated as  $\sim 1.03 \text{ V}$  and the open circuit potential for a fresh cell ranged from around  $\sim 0.965$  to  $\sim 0.985 \text{ V}$ . The above percentage fraction of gases in the mixture was chosen as an approximate simulated composition which is obtained after a typical steam reforming process of a hydrocarbon fuel/natural gas. Heated lines were used to maintain the system above the dew point of water to avoid any condensation. The poisoning test was completed by adding impurity-containing  $\text{N}_2$  gas with the adjusted concentration levels of the particular contaminant to the main fuel feed at a temperature of  $750 \text{ }^\circ\text{C}$ . The contaminant compounds chosen for the impurities were (i)  $\text{H}_2\text{S}$  for Sulfur, (ii) Dimethylcyclopentasiloxane ( $\text{D}_5$ ) for siloxane and (iii) Tetrachloroethylene for Cl. The type of contaminants and their concentration

level for poisoning was decided keeping view of the practical operation of SOFC systems after carefully reviewing literature and suggestions from Delphi and Department of Energy (DoE). It was agreed to test at typical ppm/ppb levels to which tested commercial/industrial cleaning systems would reduce the concentration of inorganic impurities, from those in unprocessed alternative fuels. For maintaining the proper concentration levels of liquid contaminants at ppb/ppm in the gaseous phase the vapor density – temperature data was taken into consideration. The flow rates through the bubbler containing the contaminant chemical were accordingly adjusted to make up the main fuel stream with the required concentration as close as possible. Gaseous contaminants were added directly from gas cylinders and concentrations in the fuel stream were adjusted.

Experiments were conducted both at open circuit potential (OCP) and at a constant current density of  $0.3 \text{ A cm}^{-2}$  in power generation mode. The criteria for the chosen current density was to avoid the re-oxidation of the active Ni anode which could lead to cell delamination and fracturing under such high operating temperature regimes. For obtaining the impedance spectra at constant current conditions, a Solartron Analytical 1252-A Frequency Response Analyzer was used in conjunction with a Solartron Analytical 1470-E Cell Test System. The frequency range for which the impedance data was obtained ranged from 0.01 Hz to 1000 kHz and the amplitude used was 10 mV. This allowed the electrochemical processes to be represented in the Nyquist plots. Equivalent circuit modeling was performed using ZView version 3.2c on the obtained EIS spectra to determine the corresponding electrochemical parameters associated with the fuel cell system. Tests were repeated multiple times to check the stability and repeatability of the obtained data. In some cases, recovery tests were carried out by returning the cell conditions to a pure fuel feed which was free from any inorganic impurity. Thermochemical calculations were performed to derive stability diagrams of different phases expected to be present in a reaction system at the elevated operating temperature. HSC Chemistry (Version 5. Outokumpu Research Oy, Finland)

was applied to obtain phase and equilibrium diagrams. The calculation method adopted by the above software was the minimization of Gibbs energy.

### 3.2.3 Impedance diagram fitting

Kramers-Kronig (KK) transformations [26] were initially performed to validate and confirm that the obtained data was of high quality and experimentally valid. After the data was validated, equivalent circuit modelling was carried out with ZView using the complex non-linear least squares fitting (CNLS) method. This is a nonlinear least-squares fit of the real and imaginary parts, or magnitude and phase-angle of the experimental impedance to a given model. The sum of squares ( $S$ ) can be represented as below:

$$S = \sum \{ w_i' [Z_i' - Z_i'_{\text{calc}}]^2 + w_i'' [Z_i'' - Z_i''_{\text{calc}}]^2 \}$$

where  $Z_i'$  and  $Z_i''$  are the real and imaginary parts of the experimental impedances at the frequencies  $\omega_i$ ,  $Z_i'_{\text{calc}}$  and  $Z_i''_{\text{calc}}$  are the values calculated from a given model,  $w_i'$  and  $w_i''$  are the statistical weights of the data estimated as inversely proportional to the measured impedances, and the summation runs over all  $N$  experimentally used frequencies ( $i = 1$  to  $N$ ). The above minimization of error procedure is iterative, hence a relatively close initial guess of some of the parameters is required to simulate the observed experimental data. While fitting, physico-chemical explanations for the system were considered and accordingly fitted with the above procedure to corresponding models to allow for convergence of model data. The best fit of the experimental data with the adopted model were checked using the sum of squares and chi-squared value ( $\chi^2$ ). A standard chi-squared figure for a well fit model to a particular EIS data was considered less than  $10^{-5}$  [21]. In some cases due to circuit ambiguity, local minima occurred. In that situation, new initial parameter values were chosen and convergence was re-checked with new chi-squared values for various circuits.

### 3.3 Results and Discussion

#### 3.3.1 Baseline Impedance Behavior with Reformate

It is also a well-known and studied fact amongst researchers that the presence of sulfur affected the carbon containing fuel streams in a different way. Two primary means of effect could be the poisoning of water gas shift reactions and the competition for surface adsorption of  $H_2$  and CO molecules [16, 17] on the active anode surface. The poisoning of the shift reaction can take place by possible side reactions of the elemental sulfur with carbon species thus in the process affecting the conversion of CO to  $H_2$ . Surface adsorption effect is also well known [2-7] due to the fact that sulfur coverage reaches equilibrium rapidly on the outer nickel surface thus reducing the adsorption rate of  $H_2$  and CO in multistep electro-oxidation reaction. However it has been seen this effect is maximum and pronounced at very low  $H_2$  to CO ratios in the fuel [8]. In our case the equilibrium composition used had a very high  $H_2$  to CO ratio which made it possible to negate the effects of sulfur on reforming to a little extent keeping the degradation within an acceptable limit. But it was necessary to differentiate between the impedance effects of reformate with and without  $H_2S$  for a same time period for similar button cells. This was important to understand the difference in mechanism when sulfur is injected into the system and the appropriate, conceptually applicable electrochemical models which can be applied in that case to understand the change of behavior. Two set of data were obtained in Fig. 3.2 for reformate composition mentioned before without  $H_2S$  for a period of 500 h at open circuit and constant current polarized conditions ( $0.3 \text{ A cm}^{-2}$ ). The data shown were the three subtraction spectra obtained by a series subtraction of the impedance curve obtained at  $t=0$  from the one obtained at  $t= 200, 400$  and  $500$  h. In this way true anode change was specifically checked because the cathode characteristics were expected to be similar

throughout the experiment. A similar approach was considered for the poisoning tests with the three impurities in the work. It was also made sure that the fresh cell for both the cases and for all other poisoning tests were as close to each other in terms of electrochemical performance, to avoid any complications due to a poorly home-made electrode assembly. Upon initial visual inspection of the impedance trends for both the cases it was observed that there were two time constants (two depressed semi-circular arc) for both the cases at all data points taken at various time of operation. The behavior was found similar to few other works [17-19] and different [16] in terms of the observable arcs in the response. Usually the low frequency arc was attributed to the gas diffusion contribution which included both  $H_2/H_2O$  and  $CO/CO_2$  diffusion [8,16,17], but in our case the low frequency part (summit frequency 0.5 Hz) was obtained as a single arc which could be attributed to differences in equipment resolution and system specifications. The proper model selected to fit the data obtained in Fig. 3.2a and 3.2b consisted of two  $RQ$  elements in series with a series resistance shown in Fig. 3.2c. The fitting was considered optimal, keeping view of the CNLS criterion mentioned before. The fitted parameters are given in Table 3.1.

Even though the visual evolution of the impedance plot was quite similar in OCP and galvanostatic conditions over the entire duration, it was observed that there was a significant difference between the percentage increases of the corresponding resistances for both the operating modes. The dependency of the high frequency arc (summit frequency  $\sim 1$  kHz) on hydrogen partial pressure and temperature indicated a charge transfer dominated process [21-24], while anode gas flow rate,  $CO/CO_2$  ratio and water content particularly affected the low frequency arc signifying diffusion related process as mentioned before. It was clearly observed from Table 1 regarding the evolution of the resistance contributions that the resistances in galvanostatic mode increase at a lesser rate than the one in the OCP mode. While the  $R_2$  (high frequency arc) and  $R_3$  (low frequency arc) in OCP mode increased by a factor of 10 and 14 respectively, the same parameters in galvanostatic mode increased by a lesser number of  $\sim 4$  and  $\sim 5$ . Due to the initial cell parameters

being very similar, the comparison was even more applicable. This behavior can possibly indicate towards a higher oxygen flux in polarized conditions leading to the surface oxidation of non-hydrogen adsorbed species which might be contributing towards the higher increase of the charge transfer resistance in OCP mode.

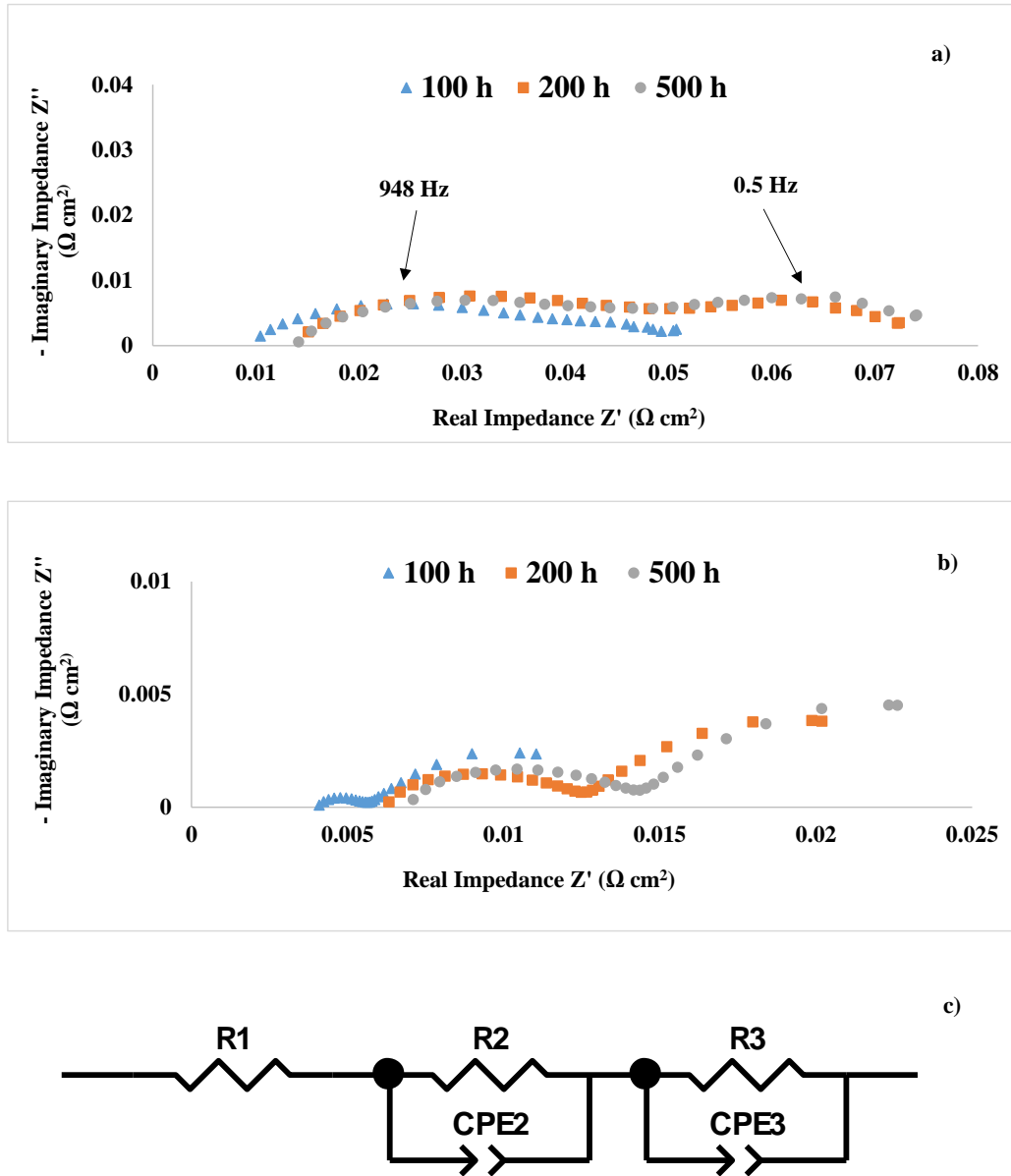


**Fig. 3.2 (a)** Subtraction Impedance spectra of the SOFC cell at 750 °C exposed to the simulated reformat observed after 100, 200 and 500 h at OCP. **(b)** Subtraction Impedance spectra of the SOFC cell at 750 °C exposed to the simulated reformat observed after 100, 200 and 500 h at

galvanostatic conditions of  $0.3 \text{ A cm}^{-2}$ . (c) Equivalent Circuit model to fit reformat fuelled impedance data for both OCP and galvanostatic conditions.

**Table 3.1** Resistive parameters obtained from the equivalent circuit modeling of the subtraction impedance spectra for pure reformat fuelled button cells.

<b>OCP Mode (Zero Current)</b>			
<b>Parameter/ time (h)</b>	<b>100</b>	<b>200</b>	<b>500</b>
$R1 (\Omega \text{ cm}^2)$	0.0086	0.0124	0.0134
$R2 (\Omega \text{ cm}^2)$	0.0216	0.0317	0.0228
$R3 (\Omega \text{ cm}^2)$	0.0239	0.0346	0.04748
<i>Chi- Squared value</i>	2.12E-05	3.78E-05	0.98E-05
<b>Constant Current mode – <math>0.3 \text{ A cm}^{-2}</math></b>			
$R1 (\Omega \text{ cm}^2)$	0.0038	0.0058	0.0065
$R2 (\Omega \text{ cm}^2)$	0.0021	0.0067	0.0078
$R3 (\Omega \text{ cm}^2)$	0.0074	0.0133	0.0155
<i>Chi- Squared value</i>	2.5E-06	2.47E-06	3.52E-06

It has been studied by researchers that CO electro-oxidation rate was a much slower step than  $\text{H}_2$  oxidation [8, 26] and also the fact that CO species did not undergo diffusion into the porous structure to get oxidized into  $\text{CO}_2$ . In comparison the bulk of CO usually is adsorbed on the active sites on the anode surface. In the galvanostatic mode, the constant oxygen flux initiated by the

higher potential gradient in the cell increases the rate of electro-oxidation of surface adsorbed CO species. Such improved oxidation of surface species can also play an important role in relative removal rate of adsorbed inorganic species as is discussed later. As far as the low frequency arc was concerned, even though the nature of arc was quite similar in both cases with excellent fitting of the same model, there was difference in their quantitative evolution which was not totally clear. A higher increase of  $R3$  in OCP mode, can be related towards gas conversion process impedance which means a higher amount of  $H_2$  and CO species diffused through the inert  $H_2O$  and  $CO_2$  into the porous anode structure. In polarized mode, higher conversion of the fuel molecules can lead to a reduced low frequency impedance because more percentage of fuel species get converted to  $H_2O$  and  $CO_2$ .

### 3.3.2 Degradation Due to Sulfur Poisoning

Thermochemical calculations and stability diagrams were obtained for a system comprising of Ni-H-S system to predict the chemical reactivity with contaminants. Fig. 3.3a and Fig. 3.3b show the thermodynamic stability diagrams with variation in temperature and also variation in  $H_2$  partial pressure respectively. At the temperature range of interest (750 – 800 °C), it is observed that  $Ni_3S_2(s)$  did not exist as a stable phase at concentrations in hundreds of ppm's of  $H_2S(g)$  (represented on the y-axis log scale; -4 is equivalent to 100 ppm). The stability region of  $Ni_3S_2(s)$  was almost absent above 800 °C. Only at significantly higher concentration of more than 1000 ppm and low temperatures below 400 °C, there were possibilities of the 3D sulfide formation as mentioned before. From Fig. 3.3b it can be seen that at 750 °C, when concentration of  $H_2(g)$  was sufficiently high, there should be no sulfide formation based on the stability diagram.  $Ni_3S_2$  only exists in an environment with very poor hydrogen content. The formation of other stable sulfide phases such as  $Ni_3S_4$  and  $NiS_2$  are more unlikely to occur at the specified operating conditions. Therefore from above discussion and studies of other researchers [2,3,6], it is clear that only in

extremely high sulfur concentrations in the order of hundreds of ppm, bulk transformation of nickel takes place at normal SOFC operating temperatures. According to Ghoniem et al. [8], a partial pressure ratio of  $\text{H}_2\text{S}/\text{H}_2$  of the order of  $10^{-3}$  at standard temperatures creates the formation of  $\text{Ni}_3\text{S}_2$ . Thus considering the concentration levels tested in our work, chances of bulk sulfide formation can be safely neglected.

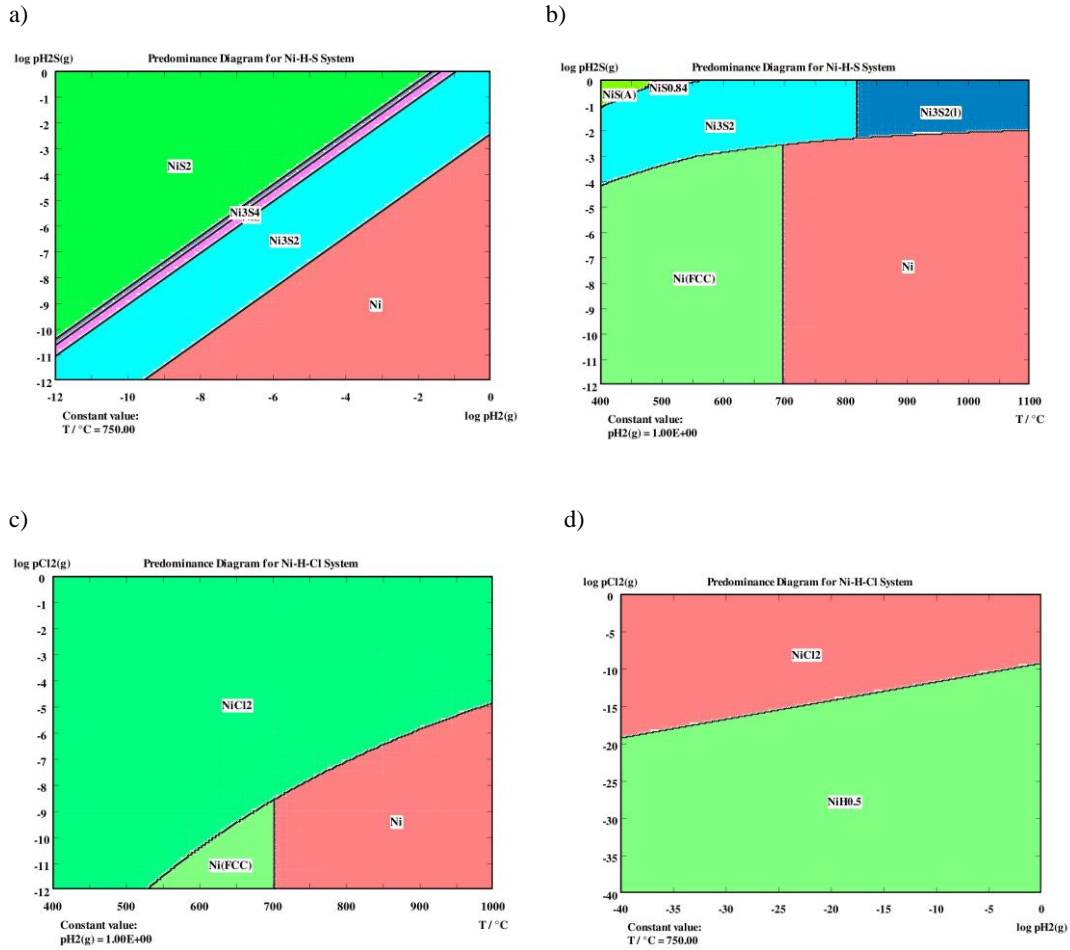


**Fig. 3.3** (a) Stability diagram of the Ni-H-S system derived from thermochemical calculations over a temperature range at a constant hydrogen partial pressure. (b) Stability diagram of the Ni-H-S system derived from thermochemical calculations over a hydrogen partial pressure range at a constant temperature. (c) Stability diagram of the Ni-H-Cl system derived from thermochemical calculations over a hydrogen partial pressure range at a constant temperature. (d) Stability diagram

of the Ni-H-Cl system derived from thermochemical calculations over a hydrogen partial pressure range at a constant temperature.

Introduction of sulfur into the system with the specified fuel composition showed a completely different impedance behavior under galvanostatic conditions. Three concentrations of H<sub>2</sub>S (0.2 ppm, 1 ppm and 4 ppm) were tested for the cell at 0.3 A cm<sup>-2</sup> for 200 h each. The Ni/YSZ electrode is connected in series with the electrolyte and the cathode. In this test only the conditions with respect to the anode were changed and only the sulfur concentrations were changed from the start of the experiment with the same reformat compositions for all three tests. All other conditions including cathode gas characteristics, temperature, initial cell performance was kept constant and as close to each other. Therefore an impedance subtraction spectrum for each H<sub>2</sub>S poisoned spectrum after 100 h with respect to the spectrum at the 0 h mark with non-poisoned reformat can be obtained. In this way the true representation of change in the anode characteristics with shifting of the fuel from a pure reformat to a poisoned reformat can be determined. A similar analysis was carried out by Jensen et al. [25], but on solid oxide electrolysis cell anode materials. Thus, the actual change in anode impedance can be obtained making it easier to relate the change of behavior to the effects of various levels of H<sub>2</sub>S in the fuel stream. Fig. 3.4 shows the impedance diagram obtained after subtracting the initial impedance data from the final impedance data obtained after 200 h for the three respective H<sub>2</sub>S concentration levels.

The expected mechanism by which sulfur can affect the performance is either by (1) blocking the active surface sites and thus converting them inaccessible for consequent adsorption of H<sub>2</sub> or by (2) structural changes in the anode catalyst caused by strong & thermodynamically reversible Ni-S interactions. Another possibility is that sulfur reacts chemically with the adsorbed and bulk H<sub>2</sub> and CO molecules [8,9,17]. The thermodynamics of such multi-component mixtures with sulfur is very complex because the electrochemistry and stoichiometry varies with changes in operating

parameters such as temperature and pressure. Therefore, predicting the exact mechanisms becomes a very difficult task. However, knowledgeable assumptions and analysis based on impedance modelling helps to understand the impact of sulfur on degradation of the anode catalyst layer. Sulfur has always been known to have a strong affinity for metallic catalysts such as nickel. An adsorbed sulfur atom physically blocks at least three or four metal atom surfaces (in a three dimensional space). Due to its strong chemical bond, sulfur electronically modifies its nearest neighbor atoms and their capability to adsorb and/or dissociate the reactant molecules. Because of the changed surface structure the surface diffusion of adsorbed reactants is prevented or slowed down [35,36].

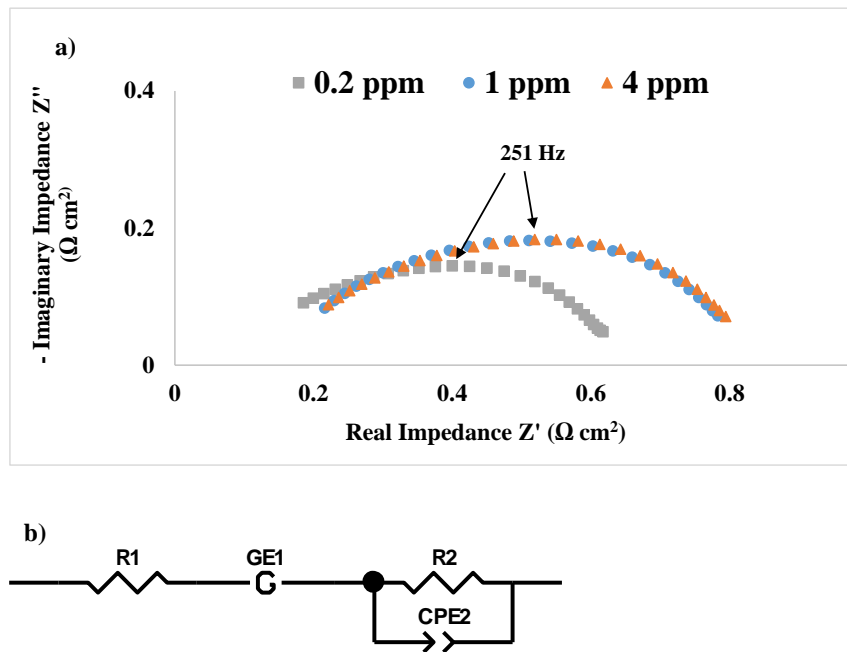


**Fig. 3.4** Subtraction impedance spectra of the SOFC cell relative to the start of the test at 750 °C exposed to the simulated reformat observed after 200 h at 0.3 A cm<sup>-2</sup> for 0.2, 1 and 4 ppm of H<sub>2</sub>S. (b) Equivalent Circuit model to fit the sulfur poisoned reformat fuelled impedance data.

An important observation was that the two time constants with a pure reformat at galvanostatic conditions changed to an impedance plot with one visible primary arc. Thus it was a distinct change observed reflecting the effect of sulfur on the electrochemistry. The obtained impedance curves were used for circuit fitting and two primary element combinations were considered to fit with the obtained diagram. The two elements used were a standard  $RQ$  model and the Gerischer element. It was observed that the chi-squared value after fitting a  $RQ$  element with a series resistance to the diagram was around  $2 \cdot 10^{-2}$ . Even though the high frequency part fitted well there was significant deviation in the low frequency part between the obtained data and simulated model leading to a higher chi-squared value. The overall fitting improved considerably especially in the low frequency part, with a chi-squared value  $6 \cdot 10^{-5}$  after the introduction of the Gerischer element in series with a  $RQ$  element and a series resistance. The model is shown in Fig. 3.4b. The sulfur reaction chemistry is such that it can be modeled as a Gerischer response which constitutes a slow adsorption (reaction) step coupled with a chemical reaction/ diffusion. In other words, this circuit element is usually associated with molecular reactions taking place in the bulk of porous electrodes before any electrochemical oxidation/reduction occurs. According to Boukamp et al. [34] the modelling with a Gerischer element is applicable to such reaction schemes mentioned above and distributed charge-transfer steps. It is important to notice that for porous electrodes of mixed ionic-conductive materials, like the one used in the present work, processes can more complicated due to the presence of charge-transfer coupled with non-charge transfer processes distributed on the surface like diffusion, adsorption and interaction of sulfur with the fuel species. This explanation is also consistent with the findings of a similar analysis by Kjelstrup et al. [32] in a PEM fuel cell system.

The Gerischer impedance can be derived from diffusion with a 'sink term' in Fick's second law. The simple meaning is that the electrochemical active species are reacting away in a conversion

process to an inactive complex or absorbed species. The overall impedance describes a semi-infinite diffusion with a side reaction and the frequency domain solution can be described as,

$$Y = Y_0 (K_a + i\omega)^{1/2} \quad (1)$$

$$GE-T = Y_0 \quad (2)$$

$$GE-P = K_a \quad (3)$$

The Gerischer element as shown above consists of two electrochemical parameters: an admittance (inverse of impedance) parameter ( $Y_0$  with units  $S s^{1/2}$ ), and a rate constant ( $K_a$ , units of  $s^{-1}$ ). Here,  $K_a$  represents the first order effective rate constant of the chemical reaction. In this paper,  $GE-T$  and  $GE-P$  represent the  $Y_0$  parameter and  $K_a$ , respectively. The most interesting aspect of the Gerischer element pertains to its finite impedance value in spite of the global diffusion process being semi-infinite. The term was coined by Sluyters-Rehbach [29] and they defined this complete expression for a chemical-electrochemical-chemical reaction (CEC), i.e. two chemical reactions occurring one before and another one after an electrochemical reaction. As explained by Jensen [25], Ni/YSZ electrode is a porous composite electrode which can be visualized in the form of a transmission line model which conducts both electrons (Ni phase) and oxygen ions (YSZ phase) and the electrochemical reaction takes place at the three phase boundaries. Thus this transmission line model (infinite ladder model) can be derived for the Gerischer element mentioned. Under this model,  $r_s$  can be stated as the ionic resistance ( $O^{2-}$  in YSZ),  $r_p$  can be stated as the volume specific charge transfer resistance occurring at all the triple phase boundaries (TBPs) and  $c_p$  can be defined as the double layer capacitance at the TBPs. For a 10  $\mu m$  thick active anode layer, the Gerischer element can be applied when  $r_s \gg r_p$  which considers the assumption that increasing the Ni/YSZ electrode thickness beyond 10  $\mu m$  does not increase the electrode performance and the ionic pathways in the YSZ electrolyte are always connected in the electrode layer. The equation (1) can also be rearranged and represented as,

$$Z_{\text{Gerischer}} = (r_s/c_p)^{1/2} / [(r_p c_p)^{-1} + i\omega]^{1/2} \quad (4)$$

The above equation can also be rearranged and equated with equation (1) to give the relations of below,

$$r_s r_p = (1/Y_0)^2 (1/K_a) \quad r_s c_p^{-1} = (1/Y_0)^2 \quad (5)$$

**Table 3.2** Electrochemical parameters as a function of time obtained from the equivalent circuit modeling of the subtraction impedance spectra for sulfur poisoning tests.

<b>EIS Parameters</b>	<b>0.2 ppm H<sub>2</sub>S after 200h</b>	<b>1 ppm H<sub>2</sub>S after 200h</b>	<b>4 ppm H<sub>2</sub>S after 200h</b>
$R1 (\Omega \text{ cm}^2)$	0.074	0.136	0.136
$R2 (\Omega \text{ cm}^2)$	0.420	0.606	0.580
$GE1\text{-}T (\text{S s}^{1/2})$	2.897	4.951	2.944
$GE1\text{-}P (\text{s}^{-1})$	1907	1666	1935
$r_s r_p (\Omega^2 \text{ cm}^4)$	1.53E-04	3.90E-04	3.72E-04
$r_s q_p^{-1} (\Omega \text{ cm}^4 \text{ s}^{-1})$	0.2549	0.7444	0.7211
<i>Chi- Squared value</i>	5.5E-05	2.6E-05	0.9E-05

Table 3.2 shows the fitted parameters for the subtraction impedance spectrums of the three H<sub>2</sub>S concentration tests after 100 h. It was seen from Fig. 3.4 and Table 3.2 that with the use of

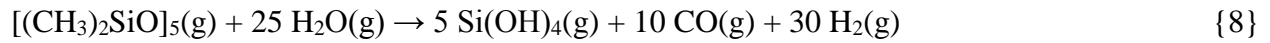
increasing concentration of  $\text{H}_2\text{S}$  in the fuel stream, there was a noticeable increase of both the terms  $r_s r_p$  and  $r_s c_p^{-1}$  relative to the beginning of the test. It was assumed that the term  $r_s$  would remain constant for the same temperature thus the evolution of the two previous terms indicates the change in anode behavior ( $r_p$  and  $c_p$ ) upon sulfur poisoning. The  $r_s r_p$  and  $r_s c_p^{-1}$  value increased by  $\sim 143\%$  and  $\sim 182\%$  respectively upon increasing the concentration. This increase could be attributed to the rapid adsorption of sulfur onto the anode surface and the TPB, which results in the surface nickel inhibition to the required electrochemical activity. A similar behavior was observed by Jensen [25] where they postulated buildup of impurities at the TBP during electrolysis resulting in the increase of the resistance per unit length in the TBP. It was also interesting to note that the increase in the charge transfer resistance in the latter half of the experiment was comparatively much lower than the initial period. The values of  $r_s r_p$  and  $r_s c_p^{-1}$  almost remained stable for the 1 ppm and 4 ppm case. This indicated that the primary degradation related to the charge transfer process occurred at the initial introduction of sulfur within the range of  $< 1$  ppm in the system when the sulfur adsorption dominated the entire electrochemistry and prevented activation controlled reactions to occur at the same rate vs. a fresh cell. Once the cell operated for a sufficiently long time and  $> 1$  ppm, it would be more accurate to assume that the extent of adsorption was constant over time (i.e. new molecules were being adsorbed as fast as they were reacting/desorbing). The process had then reached a steady-state which would actually make a stable maximum of the coverage. In the definition of the infinite ladder model discussed before, the Gerischer type response of a system only occurs when  $r_s \gg r_p$ . When  $r_p$  becomes too large and becomes higher than the ionic resistance  $r_s$ , the system cannot be modelled by this response. Instead a simple  $RQ$  element is required to fit the appropriate data. Thus this variation of impedance behavior in the subtraction spectrum can very well help to determine the limits within which the charge transfer resistance is within a specific limit showing the extent of degradation in sulfur poisoned Ni/YSZ anodes. With even higher concentration ranges of  $\text{H}_2\text{S}$ , the Gerischer behavior

may not be visible and hence can provide a check for degradation limits with variation in concentration ranges. The behavior of the low frequency arc ( $R_2$ ) was ambiguous but overall it showed the expected trend. As explained earlier the low frequency arc for a reformate fueled cell was associated to the combined diffusion effects of  $H_2$  and CO. The value of  $R_2$  increased with increase in concentration of 0.2 ppm to 1 ppm  $H_2S$  by around 40 %. This can be attributed to the fact that with a higher ppm content of sulfur in the fuel, the water gas shift reaction gets poisoned for which CO conversion gets affected [5-8]. Thus the additional CO/ $CO_2$  contributes towards increasing the overall gas density of the system inducing an additional gas transport resistance. Interestingly, it was observed that when the concentration was 4 ppm, the relative increase in  $R_2$  was almost similar to the 1 ppm case. This non-linearity of impedance increase was also seen for the charge transfer Gerischer impedance.

### 3.3.3 Siloxane Poisoning and Degradation Modelling

Siloxanes are organosilicon compounds generally represented as  $[SiO(CH_3)_2]_n$  or  $[SiO(C_6H_5)_2]_n$ . These classes of compounds have been shown to be present in ppb/ppm levels in biogas or digester gases. Knowledge of the mechanism of degradation and also the tolerance levels for siloxane compounds will help to develop novel adsorbents for efficient removal of siloxane to acceptable concentration levels. Organic siloxanes are semi-volatile compounds. The gaseous compounds are not reactive or corrosive as such, but they do turn into hard, abrasive silica in the engine's combustion chamber. In the combustion of siloxane, gas microcrystalline silica is formed, which has similar properties to that of glass. This hard substance can also additionally act as a thermal and electrical insulator on the surfaces. The thermodynamics of  $D_5$  is such that it thermally dissociates into silica ( $SiO_2$ ) at high SOFC operating temperatures and silica can be deposited or precipitated on the porous anode cermet. The formation chemistry of silica deposits under high temperature SOFC conditions can be explained by the reactions below which has also been

validated by researchers before in their reaction mechanism studies in SOFC fuel cleaning and combustion area [3],



The above reactions result in the formation of an insulating non-conducting oxide layer on the anode as confirmed by others [2-4, 20] in their poisoning tests and microstructural images. This prevents (completely or partially depending upon the time of operation) the passage and diffusion of the fuel into the TPB where electrochemical oxidation of the fuel takes place.

In fact during the 20-hour operation with 10 ppm D<sub>5</sub> (Fig. 3.5a), as mentioned before, the anode surface was speculated to be completely deactivated by the silica for which the data points in the EIS plot are not consistent and shows discontinuity in trends at lower frequencies. Even at such a low concentration, deposition of solid silica at the anode cermet severely affected the hydrogen diffusion and electrochemical oxidation reaction at the anode TPBs. The continuous precipitation of SiO<sub>2</sub> also seemed to cause an instability issue in the cell causing mechanical damage causing possible cell fracture which was directly observed by the discontinuity and spraying of the data points and the increase in the low frequency arc. It can be also be noticed on the real impedance intercept in Fig. 3.5b, which was simply the ohmic resistance of the cell increasing appreciably within a very short period of time indicating that the adsorbed silica affected the current collector and the electrical leads forming an insulating barrier between them and the electrodes. This directly increased the ohmic resistance of the cell slowing down the passage of electrons from the anode to the cathode.

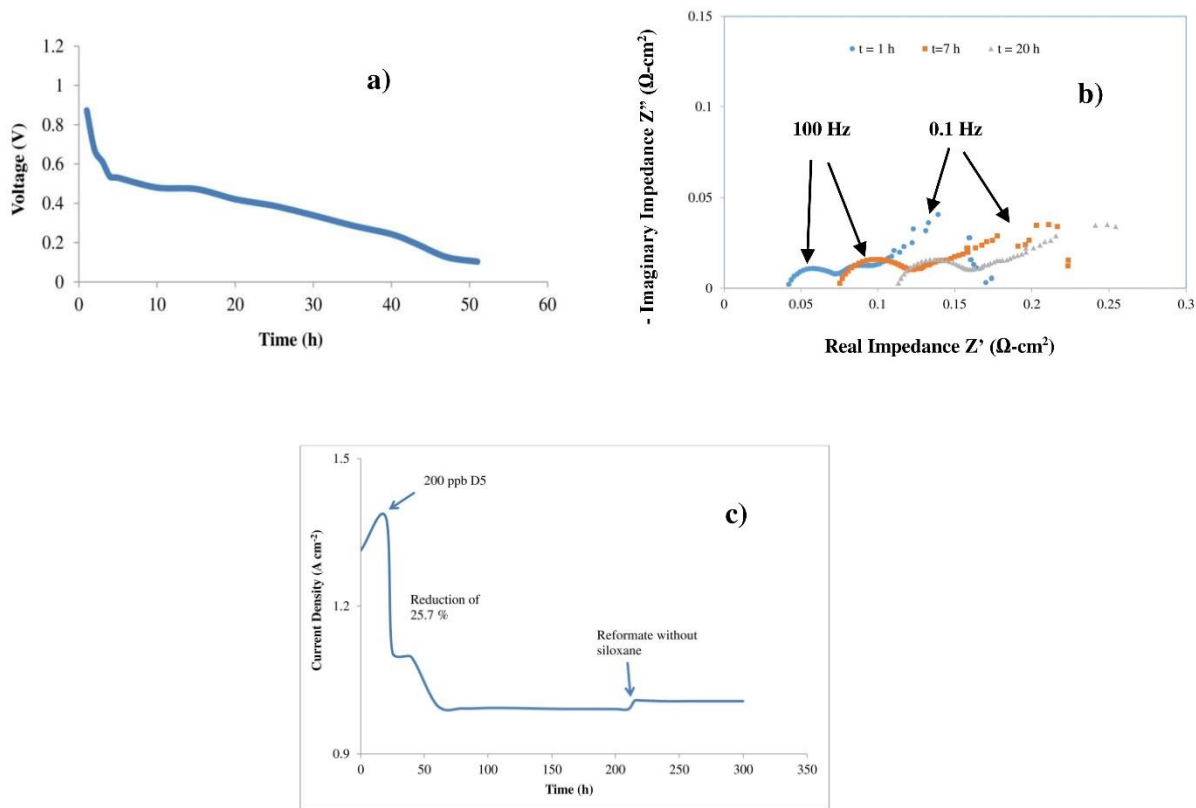


**Fig. 3.5** (a) Cell potential - time curve for 10 ppm D<sub>5</sub> on simulated reformat at current density of 0.3 A cm<sup>-2</sup>. (b) Impedance spectra of the SOFC at 750 °C exposed to the simulated reformat with 1 ppm of D<sub>5</sub> taken after 1, 7 and 20 h at a current density 0.3 A cm<sup>-2</sup>. (Notice the irregular and inconsistent nature in the low frequency region and high increase in ohmic impedance). (c) Current density vs. time for a siloxane poisoning test in SOFC fueled by simulated reformat with 0.2 ppm of D<sub>5</sub> at a potential of 0.58 V.

The previous results clearly indicated that ppm levels of siloxane produced a detrimental effect on the cell behavior. Therefore, in this study the siloxane concentrations were reduced down to ppb values for further testing. In the case of siloxane, the deposited silica adhered to the anode surface and formed a very stable oxide layer, which was resistant to electrochemical oxidation and its removal from the anode surface was difficult, also confirmed by microscopic images by Sasaki

et al. [4,20]. Thus, the insulating silica layer deactivated the reaction sites permanently and reduced the cell performance.

When the active nickel anode was exposed to a small concentration of siloxane of 0.2 ppm (Fig. 3.5c), there was no significant or immediate deactivation of the cell but a sustained reduction of performance. This reduction of performance could be attributed to the gradual formation of thin and porous silica films on the active catalytic sites. In this case where concentrations were as low as 0.2 ppm, there was no immediate deactivation caused to the cell unlike before when 1 ppm of siloxane was added to the fuel stream. Exposure to higher concentration siloxane compounds may have caused cell fracturing or delamination, as which would explain the increasing ohmic resistances in Fig. 3.5b. This effect in button cells could also possibly be attributed to mechanical stresses generated due to the excessive weight developed on the system which could micro-fracture the cell when there was a large weight of deposition of non-conductive solid materials. Because the button cells were not robust systems and fixed on the system using ceramic materials, heavy weight developed due to accumulation of solid materials can lead to the above behavior observed. In this case, the coating seemed to behave as a thin capacitive coating, which actually formed a porous non-conducting layer on the catalyst. From our impedance spectroscopy measurements, consistent semi-circles with straight lines at an angle were obtained which signified charge transfer process followed by a capacitive behavior coupled with diffusion. Sasaki et al. [3] observed a substantial amount of  $\text{SiO}_2(\text{s})$  deposited near the top surface but only a smaller amount was found near the anode TPBs. They had used a 10 ppm concentration siloxane for their tests. Thus, it is quite evident that at even lower concentrations of  $\text{D}_5$  we should expect interaction of the silicon species with the inner TPBs and the outer functional layer of the anode. Therefore, this led to a reduced harmful effect on the charge transfer process than the mass transfer processes which occur between the anode surface and the bulk fuel stream.

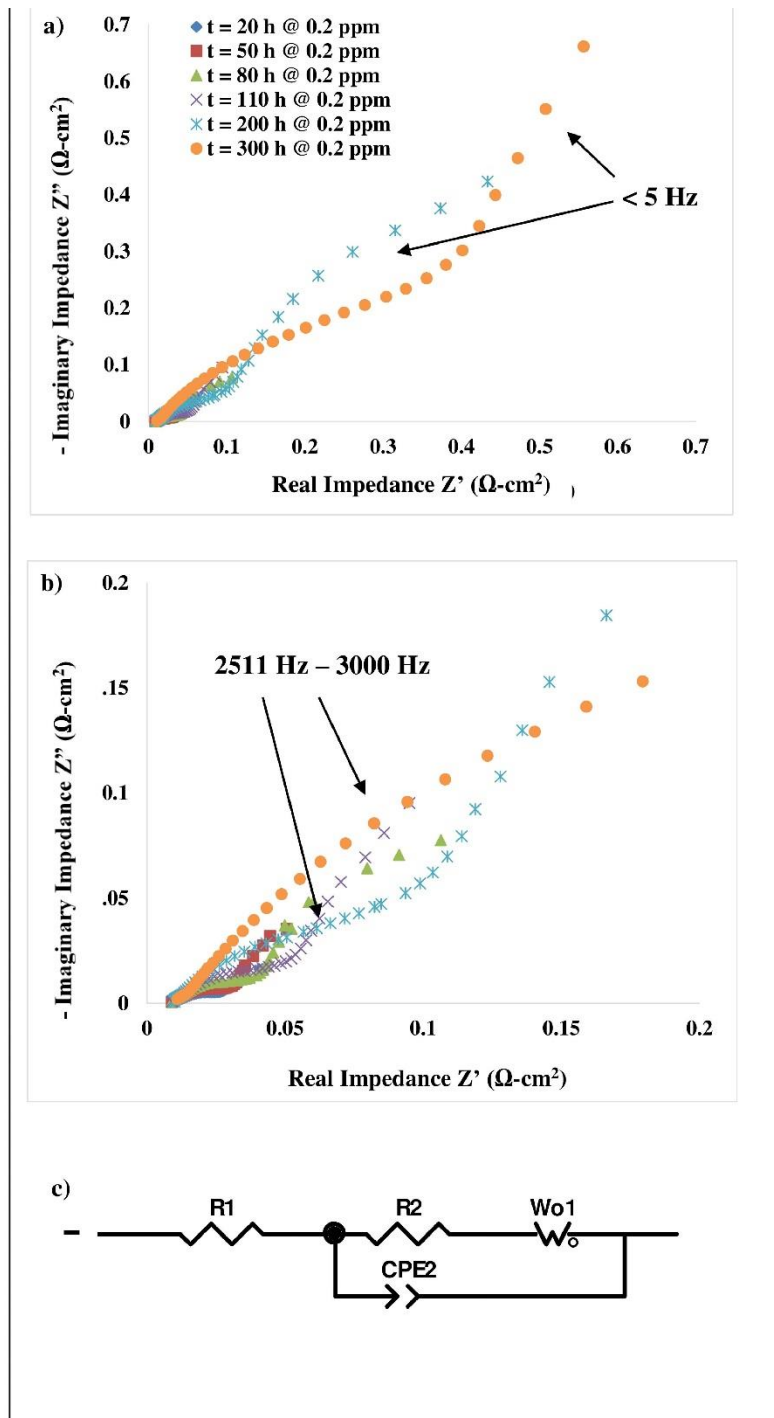


**Fig. 3.6** (a) Subtraction impedance spectra for the SOFC at 750 °C exposed to the simulated reformat with 0.2 ppm of siloxane during a period of 300 h at a current density  $0.3 \text{ A cm}^{-2}$ . (b) The inset below shows the high frequency region of the impedance spectra. (c) Equivalent circuit model to simulate the impedance spectra for siloxane poisoning.

Impedance tests were now carried out at a much lower concentration of 0.2 ppm  $D_5$  to understand the change of electrochemical behavior with respect to the shape of the plots. In this case, tests were performed at one single concentration for 300 h and the corresponding subtraction spectrums were estimated to observe the resistance evolution with time. In Fig. 3.6a and 3.6b the gas diffusion resistance was attributed to the anode gas diffusion resistance, and the low frequency arc in the impedance data was fit with a finite-length Warburg element to extract the anode diffusion resistance ( $W$ ). The term  $W_0$  represented the ease with which the fuel gases were being transported to the reaction sites for the electrochemical oxidation to occur. The films produced in this case did seem to have a high blocking character for which there was still diffusion of the fuel species through the porous and irregular film onto the anode surface which is evident from their sustained performance over a period of 300 h. It was clear from the nature of the Nyquist plot that with the passage of time the capacitive behavior of the film increased showing an increased dielectric behavior for the oxide films. The mixed insulating and diffusing characteristics could also be due to the fact of varying rates of deposition of the oxide which makes subsequent layers porous and insulating. In this case, there was no thick deposition of silica on the anode due to a highly reduced concentration for which diffusion of fuel species still occurred through the porous cermet structure. The Randles equivalent describes the response of a single-step charge-transfer process with diffusion of reactants and/or products to the catalyst interface. To understand this behavior we propose a circuit model shown in Fig. 3.6c to model the corresponding impedance spectrum. The  $R2$  ( $CPE2$ ) models the charge transfer process and the surface roughness at the anode three-phase boundaries. The Warburg element shown ( $W_0$ ) models the diffusion process where there is a linear concentration gradient between the active reaction sites and the fuel feed stream. The insulating silica layer which was formed behaved like a capacitor due to its non-conducting nature. In a more uniform system when such passivation layers are smooth, they exhibit purely capacitive behavior, which manifests themselves in impedance spectra as almost

perpendicular lines to the real axis [26]. When a complete film is formed, there is a perfect capacitance behavior. When a film is defective, it ends up with (potentially very small) active sites where the reaction can occur.

It was observed from the obtained data that there was a gradual increase in both the values of the charge transfer resistance and the diffusion resistance over the period of time. The most interesting aspect to consider in this case was, when a much lower siloxane concentration was used, the percentage increase in the diffusion related resistance ( $W_0$ -R) was lower than the charge transfer resistance ( $R_2$ ). As seen from Table 3.3, the value of  $R_2$  increased about 2.75 times during the period from 100 h to 300 h while  $W_0$ -R increased 1.25 times. This behavior was different from the case where a much higher siloxane concentration was used. This indicated a significant effect on the triple phase reaction sites within the porous anode structure even though the cell did not get permanently poisoned and was not deactivated. The effect can be mostly attributed to permanent blocking of electro-oxidation sites inside the porous anode catalyst. Notice that this effect was different from sulfur which was more of surface adsorption related effect (partially reversible) whereas siloxane probably had an irreversible effect on the porous nature of the anode microstructure reducing TBP length across the entire layer.

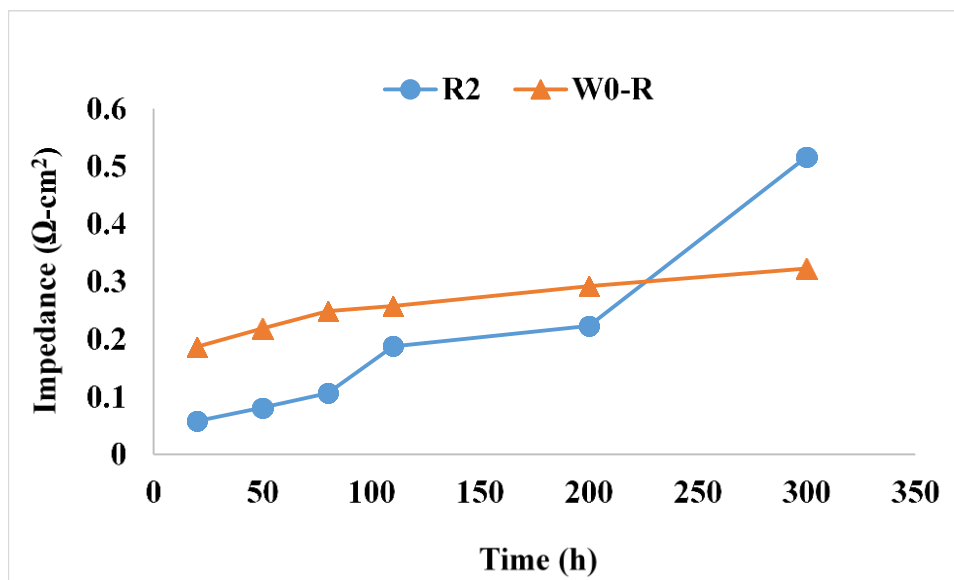
It can be validated clearly from Fig. 3.2 that the nature of the impedance spectrum for non-poisoned reformat hardly changed and the pattern/shape of the spectrum was consistent throughout the test duration. It was also ascertained that the low frequency impedance was related to the combined gas diffusion impedance for  $H_2$  and CO. In this case, the significant increase of the low frequency impedance arc (summit frequency  $\sim 0.1$  Hz) equating to Warburg behavior indicated that the processes due to the deposition of oxide films formed on the catalyst surface and the TPBs altered the porosity of the anode microstructure resulting in the decrease of performance level. This can also be easily stated as per Fig. 3.7a which shows the increase of both the charge

transfer resistance and diffusion resistance over the entire duration of the test. Reduction of porosity also seemed to affect the high frequency (summit frequency  $\sim 3$  kHz) charge transfer processes due to a direct reduction of the active TBPs available for electronic/ionic charge transfer. In Fig. 3.7b, to further verify this aspect, another sister cell was kept at a concentration of 0.2 ppm and the operating temperature was varied after 50 h of operation to observe its effects on the term  $R_2$  and  $W_0$ -R. The temperature was shifted quickly to negate any effect of operation time on the degradation response. It was seen that as the temperature was increased from 750 °C to 850 °C, there was a steady decrease in  $R_2$  due to increased YSZ conductivity of  $O^{2-}$  ions while the gas diffusion resistance was almost steady (increased a bit) showing no dependence on temperature. Thus it can be justified that the porosity was affected by siloxane poisoning and the gas diffusion resistance had no impact on better ionic exchange in the porous electrode. It was also evident from the analysis of the structural factor in the next section.

**Table 3.3** Electrochemical parameters as a function of time obtained from the equivalent circuit modeling of the subtraction impedance spectra for siloxane poisoning tests.

<b>EIS Parameters</b>	<b>0.2 ppm of <math>D_5</math> after 110 h</b>	<b>0.2 ppm of <math>D_5</math> after 200 h</b>	<b>0.2 ppm of <math>D_5</math> after 300 h</b>
$R_1$ ( $\Omega$ cm <sup>2</sup> )	0.0110	0.0114	0.0117
$R_2$ ( $\Omega$ cm <sup>2</sup> )	0.1874	0.2230	0.5163
$W_{01}$ -R ( $\Omega$ cm <sup>2</sup> )	0.2577	0.2921	0.3226
$W_{01}$ -T (s)	0.0036	0.0058	0.0105
$W_{01}$ -P	0.5000	0.5000	0.5000
<i>Chi- Squared value</i>	0.19E-04	1E-05	0.26E-05

a)



b)

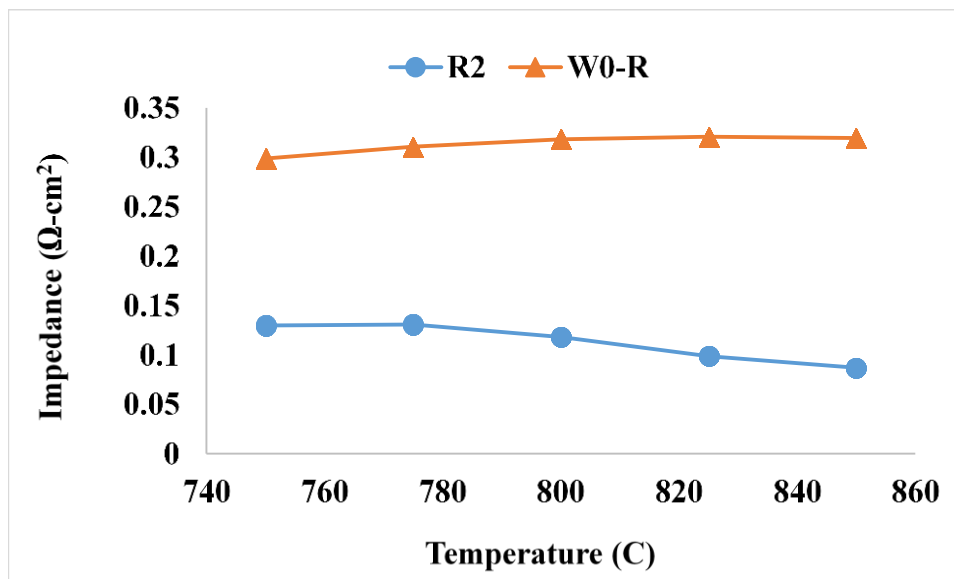


**Fig. 3.7 (a)** Evolution of the impedance (charge transfer and gas diffusion resistance) for the SOFC at 750 °C exposed to the simulated reformat with 0.2 ppm of siloxane during a period of 300 h at a current density  $0.3 \text{ A cm}^{-2}$ . **(b)** Evolution of the impedance (charge transfer and gas diffusion resistance) for the SOFC with respect to operating temperature exposed to the simulated reformat with 0.2 ppm of siloxane after 50 h of operation at a current density  $0.3 \text{ A cm}^{-2}$ .

### 3.3.3.1 Analysis of Effective Diffusion Coefficient during Siloxane Poisoning

In a recently published paper by Mogensen et al. [41], a Generalized Finite Warburg Element (GFW) has been applied for impedance response arising from gas transport contributions in an anode supported solid oxide fuel cell. The GFW is the solution of the one-dimensional diffusion equation of a particle, which is completely analogous to wave transmission in a finite-length RC transmission line. The impedance response for the finite space Warburg element (open) can be written as:

$$W_o = R_D \coth [(sT_w)^\alpha]/(sT_w)^\alpha \quad (6)$$

where  $s$  is the Laplace complex frequency,  $R_D$  is the resistance at low frequencies associated with the transport of gas through the anode supported layer in steady state,  $\alpha$  is a constant related to the roughness of the diffusion media which is equal to 0.5 for a finite Warburg impedance and  $T_w$  is a time constant which numerically is equal to  $l^2/D_{\text{eff}}$  ( $l$  is the effective diffusion thickness and  $D_{\text{eff}}$  is the effective diffusion coefficient of the particle). In this paper,  $W_o$ -R,  $W_o$ -T,  $W_o$ -P signified the  $R_D$ ,  $T_w$  and  $\alpha$  respectively.

The hydrogen diffusion coefficient in the multi-component mixture  $D_{H_2}$  at the mentioned process temperature and pressure can be calculated using the Chapman-Enskog equation [42];  $D_{H_2} = 3.717 \text{ cm}^2 \text{ s}^{-1}$

From Table 3, it is noticed that the time constant ( $T_w$ ) obtained after fitting the Warburg element to the impedance behavior shows reasonable increase from  $t=110 \text{ h}$  to  $t=300 \text{ h}$ . The time constant is a measure of the rate of movement of fuel molecules to and from the interface with a lower time constant indicating a higher diffusion coefficient and vice versa. At  $t=110 \text{ h}$  the time constant value obtained was  $0.0036 \text{ s}$ . Therefore considering  $l$  as  $500 \text{ }\mu\text{m}$  or  $0.05 \text{ cm}$  (length of the active anode catalyst layer) from equation mentioned before ( $T_w=l^2/D_{\text{eff}}$ ), we get the value of the  $D_{\text{eff},H_2} = 0.6944 \text{ cm}^2 \text{ s}^{-1}$ . The structural factor (porosity/tortuosity) was estimated as ( $D_{\text{eff},H_2}/D_{H_2}$ ) or  $0.1868$ . After

operation of the cell for 300 h, the time constant value obtained increased to 0.0105 s or 10.5 ms. The corresponding  $D_{\text{eff,H}_2}$  was  $0.238 \text{ cm}^2 \text{ s}^{-1}$ , which gave a structural factor value of 0.064. Therefore, from the obtained data it was concluded that the effective diffusion coefficient as well as the structural factor decreased by a factor of 3 over the period of 190 h. The lower diffusion coefficient indicated that the system was influenced by the poisoning of the silicon species in the porous microstructure. This can also be concluded from a lower structural factor after 300 h of operation which directly pointed towards a reduction of the volume porosity in the active anode functional layer or an increase in the tortuosity. Tortuosity is defined as the ratio of the typical diffusion path length to the electrode thickness. The typical diffusion length for the fuel particle is expected to increase with operation, which could be attributed to the accumulation of silica species in the anode microstructure resulting in a reduction of the available three phase reaction sites for the fuel oxidation and electron transfer.

#### *3.3.4 Chlorine Poisoning and Degradation Modelling*

To confirm the phases present at the specified conditions, stability diagrams were derived from thermodynamic calculations for the Ni-H-Cl system over a specified temperature range and hydrogen partial pressure. Figs. 3.3c and 3.3d show the stability diagrams with variation of temperature and hydrogen partial pressure, respectively. From the plots, it can be inferred that  $\text{NiCl}_2(\text{s})$  is stable at around  $750 - 800^\circ\text{C}$ , even at low  $\text{Cl}_2(\text{g})$  concentrations in the order of hundreds of ppb's. Thus it is assumed that the reaction between chlorine and nickel can take place at the catalyst surface after the surface adsorption of chlorine atoms on the anode.

Tetrachloroethylene is confirmed to undergo oxidative dissociation at such high temperatures in reducing atmospheres into primarily HCl and a lesser amount of  $\text{Cl}_2$  [38]. Along with HCl, various other intermediate minor compounds are formed from side reactions (with hydrocarbons

molecules present in a fuel mixture) which are basically volatile organic compounds (VOC) and are carried away with the fuel stream towards the exhaust. Due to these side reactions, a reduced concentration of chlorine compounds in ppm/ppb levels can be expected in the poisoned fuel than the one before entering the SOFC high temperature system. Hence a lesser amount of elemental Cl interacted with the actual Ni catalyst surface bringing about the corresponding degradation occurring in the system. Poisoning by chlorine was confirmed to occur in a complex mechanism and could be attributed to a reaction of the surface Ni with the halogen or hydrogen chloride to form  $\text{NiCl}_2$ . The formation of  $\text{NiCl}_2(\text{g})$  can be explained by the two reactions below [43]:



The degradation observed in this study was very slow and was accompanied by a sustained performance reduction. Chlorine is expected to react with the metallic nickel, so it is highly likely that the formation of  $\text{NiCl}_2(\text{g})$  could cause the cermet anode degradation. The interaction of the catalyst with the Nickel can also be explained by the increase in the charge transfer resistance. Due to the sublimation temperature being within  $\sim 200^\circ\text{C}$  of the SOFC operational temperature, a high vapor pressure of  $\text{NiCl}_2(\text{g})$  could also be expected, which results in a continuous evaporation process during longer duration of operation. As the sublimation temperature is quite high being  $985^\circ\text{C}$ , there is no expected permanent loss of Ni material from the cermet anode. Instead an equilibrium adsorption-desorption mechanism is speculated with constant accumulative deposition/adsorption of inorganic species.

To test the impedance response and correlate the above described expected mechanism, EIS tests were carried for three different concentrations (20, 50 and 100 ppm) for 200 h each and series subtraction spectrum were estimated just like previous cases. It was seen that unlike sulfur and

siloxane the pattern/shape of the impedance diagram was almost similar to the one obtained for non-poisoned reformat fuel. But the relative increase in chlorine poisoned cell was around 5 - 10 times higher than the plain reformat fuelled cell. From Fig. 3.8 it was observed that  $R_2$  had a reasonable change over the period of 300 h. Thus it was assumed that bonded Cl compounds blocked and reduced active sites for oxidation, thus slowing charge transfer kinetics and increasing the charge transfer resistance,  $R_2$ . It can also be considered that were no halogenated compounds depositing on the surface which would block the passage of the fuel from the bulk into the three phase reaction sites which is evident from the a minimal change of  $R_3$  attributed to the mass transfer/gas diffusion impedance. The minimal change in  $R_3$  could also be attributed to the fact that chlorinated compounds are not expected to precipitate on the catalyst layer which prevents any side reactions to occur with highly energized reformat species in the fuel stream. Thus the unchanged pattern of low frequency processes which governed gas diffusion or shift reactions were not being affected/poisoned by the presence of chlorine in the system. When chlorine-containing compounds were introduced into the fuel stream,  $\text{NiCl}_2$  is expected to form initially as per the reaction described earlier in reaction { 10}. Because  $\text{HCl(g)}$  was the predominant species present in the gas phase at such temperatures, maximum amount of  $\text{NiCl}_2(\text{g})$  forms through the second reaction { 11 } and the reverse reaction lead to the precipitation of Ni on the electrolyte and the metal surface. High temperatures and reducing fuel conditions in the anode are expected to favor the reverse reaction back to  $\text{Ni(s)}$ . The above mechanism was also confirmed by microstructural images obtained by various researchers [43,44].  $\text{Ni(s)}$  metal nucleates and starts regrouping and re-grows on the YSZ surface. This reduces both the number of active catalytic sites and the active surface area and also explains the increase of the charge transfer resistance ( $R_2$ ). Therefore, it is proposed with the combined inputs from impedance spectra and previously obtained microscopic images from other researchers that the  $\text{NiCl}_2$  product constantly vaporizes at the specified temperature.

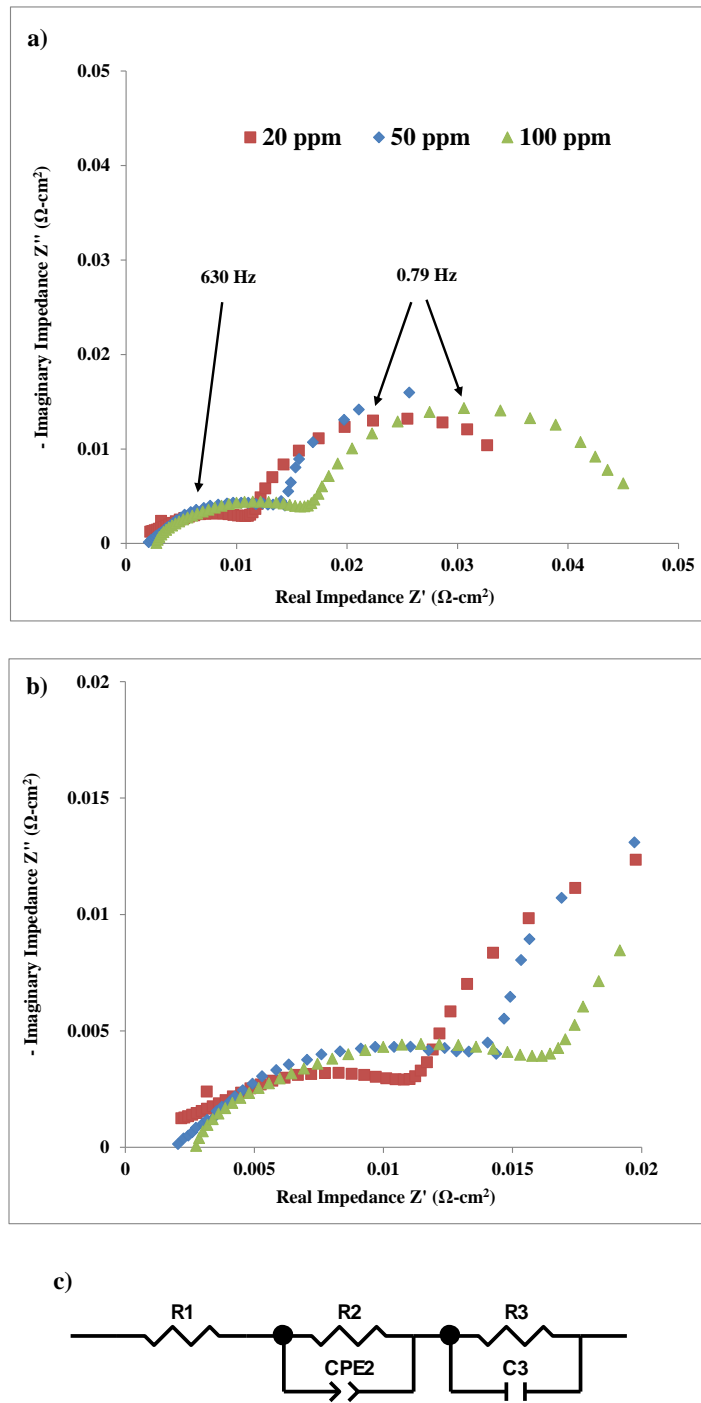


**Fig. 3.8** (a) Subtraction impedance spectra for the SOFC at 750 °C exposed to the simulated reformat with 20, 50 and 100 ppm of  $\text{Cl}_2$  after 200 h at a current density  $0.3 \text{ A cm}^{-2}$ . (b) The figure below shows a close-up of the high frequency region of the impedance spectra. (c) Equivalent circuit model to simulate the impedance spectra for chlorine poisoning.

**Table 3.4** Electrochemical parameters as a function of time obtained from the equivalent circuit modeling of the subtraction impedance spectra for chlorine poisoning tests.

<b>EIS Parameters</b>	<b>20 ppm Cl<sub>2</sub> after 200h</b>	<b>50 ppm Cl<sub>2</sub> after 200h</b>	<b>100 ppm Cl<sub>2</sub> after 200h</b>
<i>R1</i> ( $\Omega \text{ cm}^2$ )	0.0052	0.00528	0.0068
<i>R2</i> ( $\Omega \text{ cm}^2$ )	0.0254	0.0235	0.0260
<i>R3</i> ( $\Omega \text{ cm}^2$ )	0.0356	0.0392	0.03844
<i>Chi- Squared value</i>	1.15E-06	2.77E-06	6.16E-06

As shown in Table 3.4, the electrochemical parameters over the entire time period of operation allow us to speculate about the quantitative evolution of both the resistances (*R2* & *R3*) with change in the chlorine concentration, as explained earlier. The value of *R3* was almost unchanged for all the three cases varying from 0.0356  $\Omega \text{ cm}^2$  - 0.038  $\Omega \text{ cm}^2$ . It implied a very little change in the global interfacial mass transfer resistance across the catalyst surface and also the fact that the low frequency arc had no dependence on the concentration ranged used for poisoning. This explained the behavior discussed earlier. The largest change was noticed in the values of *R2*, which increased by 51 % with increase in concentration levels. In addition to points stated above, chlorine induced a degradation mechanism which can be simply described as “Reaction of Ni catalyst particles followed by re-deposition” [44]. The adsorption-desorption process was accompanied by the interference of highly electronegative atoms like Cl on the H<sub>2</sub> adsorption reaction on the active nickel catalyst as mentioned before. The above combined processes overall contributed towards the SOFC performance reduction over time. It could directly point towards a state of equilibrium after a reasonable time of operation, when the side reactions involving chlorinated compounds and

fuel molecules form intermediate products and dominate the overall chemistry inside the system. Therefore, the above observation could also indicate towards an adsorption-desorption reaction mechanism of chlorine atoms on anode surface rather than a complete removal or loss of Ni through the sublimation of  $\text{NiCl}_2$ , which would have been more prominent if the SOFC operating temperature was significantly higher.

### *3.3.5 Performance Regaining Tests*

Performance regaining tests were carried out for the three impurity poisoned cells which were important to understand their corresponding effect on anode after they are removed from the fuel stream. The initial sudden drop of about 14.5 % in the cell current shown in Fig. 3.9a was attributed to desorption/chemisorption of sulfur on the anode surface [12-16, 33]. This behavior was followed by a much more sluggish and continuous performance drop of about 2.8 % (in the next 200 h), which could be attributed to slower electrochemical kinetics at the reaction TPBs because of a smaller number of the active catalytic sites are available for the electrochemical reaction or lesser availability of hydrogen molecules (due to side reactions with the surface adsorbed sulfur) for surface oxidation. Another possible explanation is that, after the surface absorption of sulfur on Ni reaches a steady-state, the continued sulfur exposure leads to a change in surface construction of Ni as suggested by Sasaki et al. [16]. This process is expected to be much slower, and probably change the exposed Ni planes to less active ones [14]. Upon removal of  $\text{H}_2\text{S}$  from the fuel and increasing the oxygen concentration at the cathode, the cell performance gradually and slowly rebound within a few hours. However, the recovery was not complete and the cell current was stabilized at 97 % of the initial value.

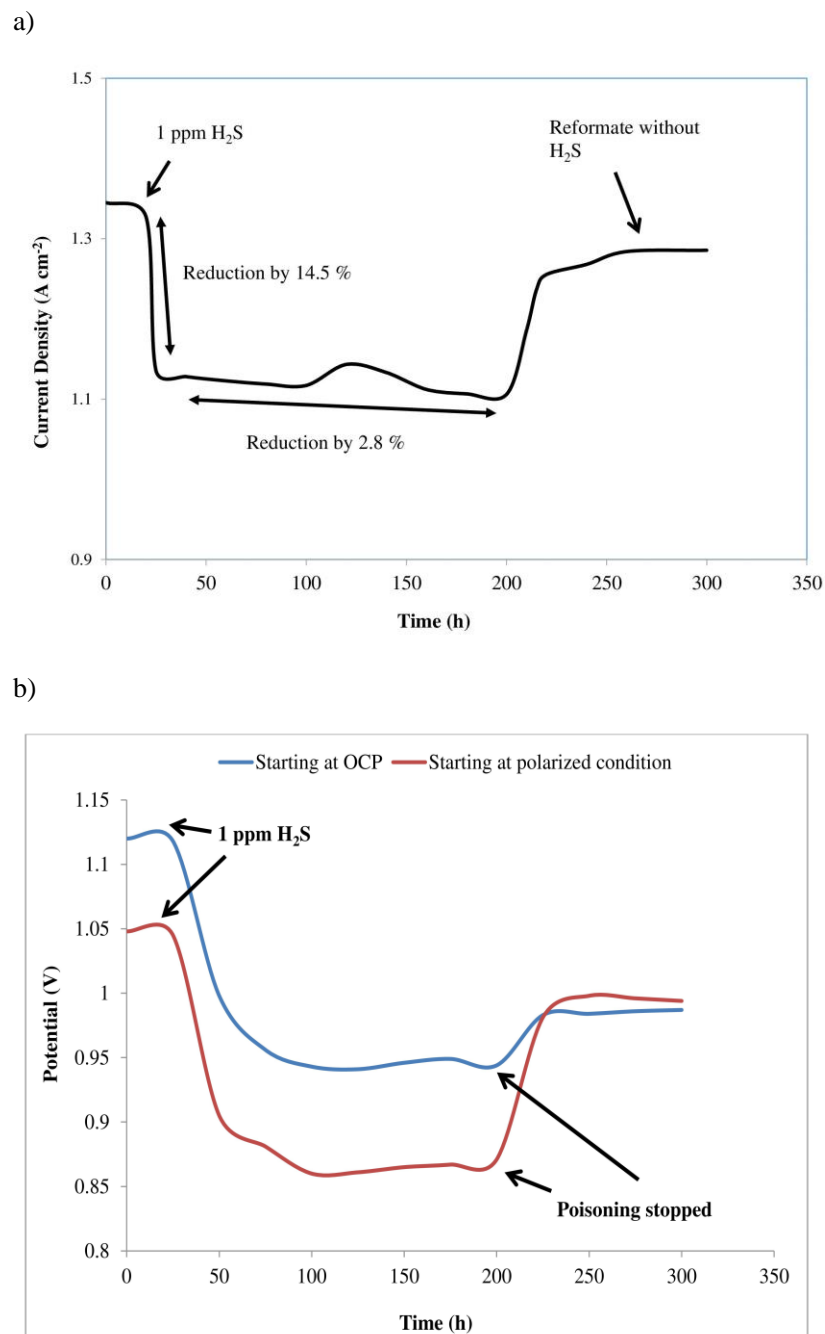
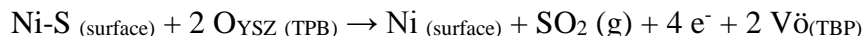


**Fig. 3.9 (a)** Current density vs. time for a sulfur poisoning test in SOFC fueled by simulated reformat with 1 ppm of H<sub>2</sub>S at a potential of 0.55 V. **(b)** Potential vs. time for a sulfur poisoning test in SOFC fueled by simulated reformat with 1 ppm of H<sub>2</sub>S – OCP condition compared with polarized condition.

It was also observed from Fig. 3.9b that the sulfur poisoning and regeneration processes strongly depended on the cell voltage. A polarized cell had more chances for the best possible recovery in the cell performance. It can be said from this study that the current passing through the cell favored the electrochemical oxidation of the sulfur adsorbed on the Ni anode surface. At polarized conditions and possibly higher relative oxygen flow at the cathode [not tested in our work], there was a higher oxygen ion flux across the electrolyte facilitating the oxidation of the adsorbed sulfur into gaseous sulfur dioxide. This resulted in a rapid desorption of the sulfur species at the anode surface, which lead to a steady removal of sulfur after stopping the poisoning process by H<sub>2</sub>S. A possible reaction for the recovery process can be as follows [38]:



where O<sub>YSZ</sub> signifies lattice oxygen, Vö - an oxygen vacancy in YSZ, TPB - the three-phase boundary between the Ni electrode, electrolyte (YSZ) and the gas phase (fuel). However, it was noticed that the actual rate of poisoning process at any particular concentration was not altered by change in cell voltage or current. The chemisorption of sulfur on Ni is a reversible process if the poisoning has not occurred at very high sulfur concentrations [which lead to an accelerated deterioration]. Therefore, exposing it to appropriate operating conditions can regenerate the sulfur-deactivated Ni catalyst. Removal of H<sub>2</sub>S from the feed gas can allow recovery of the catalyst activity, and lower H<sub>2</sub>S concentrations in the feed gas obviously lead to a lesser extent of permanent poisoning. Since chemisorption is an exothermic process, adsorbed sulfur can be also be removed by increasing the temperature [25-30,38].

When the active nickel anode was exposed to a small concentration of siloxane of 0.2 ppm (Fig. 3.10a), there was no significant or immediate deactivation of the cell but a sustained reduction of performance. This reduction of performance could be attributed to the gradual formation of thin and porous silica films on the active catalytic sites. In this case where concentrations were as low

as 0.2 ppm, there was no immediate deactivation caused to the cell unlike before when 1 ppm of siloxane was added to the fuel stream. Exposure to higher concentration siloxane compounds may have caused cell fracturing or delamination, as which would explain the increasing ohmic resistances previously in siloxane poisoning tests. This effect in button cells could also possibly be attributed to certain mechanical stresses generated due to the excessive weight developed on the system which could occur in the cell when there was a large amount of deposition of non-conductive solid materials. In this case, the coating seemed to behave as a thin capacitive coating, which actually formed a porous non-conducting layer on the catalyst. From our impedance spectroscopy measurements, consistent semi-circles with straight lines at an angle were obtained which signified charge transfer process followed by a capacitive behavior coupled with diffusion. Sasaki et al. [ ] observed a substantial amount of  $\text{SiO}_2(\text{s})$  deposited near the top surface but only a smaller amount was found near the anode TPBs. They had used a 10 ppm concentration siloxane for their tests. Thus, it is quite evident that at even lower concentrations of  $\text{D}_5$  we can expect interaction of the silicon species with the inner TPBs and the outer functional layer of the anode. Therefore, this led to a reduced harmful effect on the charge transfer process than the mass transfer processes which occur between the anode surface and the bulk fuel stream. In contrast to sulfur, after removing siloxane from the fuel stream, very small performance recovery was observed indicating a stable oxide phase on the anode as explained before after impedance tests.

Chlorine performance reduction and reversibility was tested as shown in Fig. 3.10b. A gradual reduction of 3.54 % in cell voltage was observed in 100 h. After around 120 h, the cell performance became stabilized and there was no further reduction of performance effected from the presence of impurities. In this study at the concentration level of 50 ppm, the performance reduction was not a continuous one unlike reported by Sasaki et al. [12-16]. It could directly point towards a state of equilibrium after a reasonable time of operation, when the side reactions

involving chlorinated compounds and fuel molecules form intermediate products and dominate the overall chemistry inside the system.

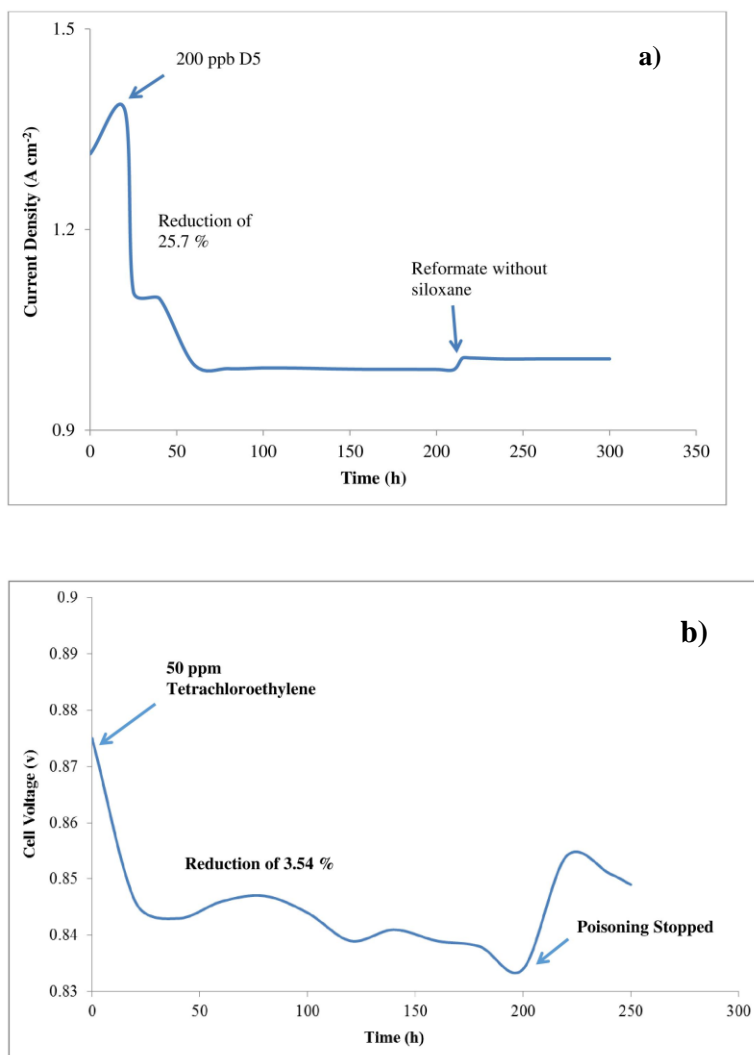


**Fig. 3.10 (a)** Current density vs. time for a siloxane poisoning test in SOFC fueled by simulated reformat with 0.2 ppm of  $\text{D}_5$  at a potential of 0.58 V. **(b)** Cell potential - time curve for 50 ppm  $\text{Cl}_2$  on simulated reformat at current density of  $0.3 \text{ A cm}^{-2}$ .

Therefore, the above observation could also indicate towards an adsorption-desorption reaction mechanism of chlorine atoms on anode surface rather than a complete removal or loss of Ni through the sublimation of  $\text{NiCl}_2$ . When the poisoning was stopped, a partial performance

regaining was noticed where the cell voltage recovered around 60 % of the original value. As we had discussed before about HCl being the dominant species at SOFC operating conditions, reaction {11} is expected to dominate the main chemistry near the catalyst surface. The above process would also explain the chances of partial recovery of the performance after the poisoning was stopped and the fuel was replaced with pure reformat, originating from (i) removal of surface adsorbed chlorine resulting in formation and entrainment of HCl(g) and (ii) re-deposition of Ni(s).

### 3.4 Summary

The influence of various inorganic fuel impurities on SOFC anodes at intermediate temperatures of 750°C and their individual degradation mechanisms have been tested and analyzed by electrochemical impedance spectroscopy (EIS) and equivalent circuit modeling (ECM). ECM with proper data fitting helped to assign generalized circuit models to quantitatively analyze the interaction behavior of foreign elements with the catalyst. While ECM is a relatively complicated technique and even though the treatment made in this study is not exhaustive, the ECM-based approach presents a realistic understanding of the complex processes of poisoning phenomena in addition to the microscopic and microstructural characterization obtained by other authors. The impedance series subtraction method was applied successfully in understanding the actual performance change brought about due to change in anode characteristics because of the presence of the three impurities in the fuel blend. The above approach helped in removing any cathodic impedance contributions towards the overall cell impedance. This approach has not been used before in SOFC impurity studies to our knowledge and can prove helpful in analyzing degradation along with microscopic investigations.

Under the influence of sulfur, the cell EIS data seemed to follow a Gerischer behavior which directly indicated a chemical-electrochemical reaction combination coupled with surface diffusion of the reacting species. This behavior was accurately fitted with a Gerischer element in the high

frequency region. Important cell parameters from the Gerischer element such as admittance and rate constant were estimated and trends were observed for sulfur poisoning. It was found that the increase in  $r_p$  was non-linear and can be used effectively to determine specific concentration ranges at which  $r_p \gg r_s$ , characterized by Gerischer behavior. Siloxane caused a detrimental deactivation of the fuel cell probably by causing deposition of silica on the anode cermet. With a much reduced siloxane concentration, it was found that extensive diffusion process dominates the low frequency part of the EIS spectra and this diffusion was attributed to the resulting blockage or obstruction to the fuel passage by the deposited inert  $\text{SiO}_2$  films. A Warburg impedance element which signified diffusion in a system was also used to fit the data and improve the proposed model. This hence proved the suitability of the chosen elements in the CNLS fitting. From the corresponding ECM the effective diffusion coefficients with passage of time were calculated using the obtained fitted Warburg element data. Changes in the structural factor also indicated a change in the porosity-tortuosity ratio in the porous Ni active catalyst layer during the poisoning process which also points towards an irreversible and stationary deposition of oxide films along the inner pores of the cermet layer. Chlorine affected the nickel metal of the Ni/YSZ cermet in a different way. There was a lesser impact on the low frequency diffusion-related arc in the EIS spectra, but the charge transfer resistance increased with increasing concentration of chlorine. This behavior can be explained by the fact that the chlorine directly interacted with the nickel catalyst via surface reactions (reaction, vaporization and re-deposition), hence reducing the amount of active TBP sites impacting the charge transfer resistance mainly on the surface. A minimal impact on the diffusion resistance possibly means the absence of any deposited halogen species on the surface which served as a continuous barrier for the fuel to enter the porous anode structure or no interaction of the impurity with the reformate species

Analysis of performance degradation by ECM and CNLS fitting in addition to the conventional EIS spectra helps to approach the issue differently and to understand the quantitative evolution of key electrochemical parameters. The circuit modelling confirms the various mechanisms by which foreign impurities affect the cell voltage at constant current density conditions. It would help to complement the microscopy techniques already used in degradation studies and relate them to meaningful physical interpretations in the fuel cell system. Future studies should be directed towards work on other different impurities with the current series subtraction approach in EIS and better ECM methodologies performed with more extensive set of experiments to test system variability in a much better way.

## References – Chapter 3

- [1] Y. Matsuzaki, I. Yasuda, *Solid State Ion.* 132 (2000) 261–269.
- [2] K. Sasaki, S. Adachi, K. Haga, M. Uchikawa, J. Yamamoto, A. Iyoshi, J.-T. Chou, Y. Shiratori, K. Itoh, *Proc. 10th International Symp. Solid Oxide Fuel Cells, Electrochem. Soc. Proc.*, vol. 7–1 (2007) p. 1675.
- [3] K. Sasaki, S. Adachi, K. Haga, M. Uchikawa, J. Yamamoto, A. Iyoshi, J.-T. Chou, Y. Shiratori, K. Itoh, *ECS Transactions* 7 (1) (2007) 1675-1683.
- [4] K. Haga, S. Adachi, Y. Shiratori, K. Itoh, K. Sasaki, *Solid State Ionics* 179 (2008), 1427-1431.
- [5] A. Hagen, *J. Electrochem. Soc.*, 160 (2) 2013 F111-F118.
- [6] J. B. Hansen, *Electrochem. Solid State Lett.*, 11(10), B178 (2008).
- [7] A. Hauch, A. Hagen, J. Hjelm, and T. Ramos, *J. Electrochem. Soc.*, 161 (6) (2014) F734-F743.
- [8] J. Hanna, W.Y. Lee, Y. Shi, A. Ghoniem, *Progress in Energy and Combustion Science* 40(2014) 74-111
- [9] Liu, Y-L., Primdahl, S., & Mogensen, M. B. (2003) 161(1-2), 1-10
- [10] H. Yokokawa, K. Yamaji, M.E. Brito, H. Kishimoto, T. Horita, *J. Power Sources* 196 (2011) 7070-7075.
- [11] S. Zha, Z. Cheng, M. Liu, *J. Electrochem. Soc.* 154 (2) (2007) B201-B206.
- [12] K. Sasaki, K. Susuki, A. Iyoshi, M. Uchimura, N. Imamura, H. Kusaba, Y. Teraoka, H. Fuchino, K. Tsujimoto, Y. Uchida, N. Jingo, *J. Electrochem. Soc.* 153(11), (2006) A2023-A2029.
- [13] J.P. Trembley, A.I. Marquez, T.R. Ohn, D.J. Bayless, *J. Power Sources*, 2006, 158, 263-273
- [14] T.S. Li, H. Miao, T. Chen, W.G. Wang, C. Xu, *J. Electrochem. Soc.*, 2009, 156, B1383-B1388
- [15] W. Feduska and A.O. Isenberg, *J. Power Sources*, 1983, 10, 89-102

- [16] A. Kromp, S. Dierickx, A. Leonide, A. Weber, and E. Ivers-Tiffée, *J. Electrochem. Soc.*, 159(5), B597 (2012).
- [17] A. Hagen, G.B. Johnson, P. Hjalmarsson, *J. Power Sources*, 272 (2014) 776-785.
- [18] L. Aguilar, S. Zha, S. Li, J. Winnick, M. Liu, *J. Power Sources* 135 (2004) 17–24.
- [19] J.P. Tremblay, A.I. Marquez, T.R. Ohm, D.J. Bayless, *J. Power Sources* 158 (2006) 263–273.
- [20] K. Sasaki, Y. Teraoka, *J. Electrochem. Soc.* 150 (11) (2003) A885.
- [21] Sanchit Khurana, Mark LaBarbera, Mark V. Fedkin, Serguei N. Lvov, Harry Abernathy, Kirk Gerdes, *J. Power Sources* 274 (2015) 1049-1054.
- [22] M.S. LaBarbera, M.V. Fedkin, J.K. Lee, Z. Zhou, S.N. Lvov, *ECS Transactions* 25 (2) 1125-1132 (2009).
- [23] M. LaBarbera, M. Fedkin, S.N. Lvov, *ECS Transactions* 35 (1) 2725-2734 (2011).
- [24] M. LaBarbera, M. Fedkin, X. Wang, X. Chao, C. Song, S. Lvov, *ECS Transactions* 35 (1) 2867-2872 (2011).
- [25] S.H. Jensen, A. Hauch, R. Knibbe, T. Jacobsen, M. Mogensen, *J. Electrochem. Soc.* 160(3) F244-F250 (2013)
- [26] *Handbook of Fuel Cells – Fundamentals, Technology and Applications*, 2009
- [27] P. Lamp, J. Tachtler, O. Finkenwirth, S. Mukherjee, S. Shaffer, *Fuel Cells* 2003, 3, No. 3
- [28] Subhasish Mukherjee, Karl Haltiner, Rick Kerr, Jin Yong Kim, Vince Sprenkle, *ECS Transactions* 35 (1) 139-146 (2011)
- [29] M. Sluyters-Rehbach, J.H. Sluyters, in: A.J. Bard (Ed.), *Electrochemical Chemistry*, vol. 4, Marcel Dekker, New York, 1970, p. 68
- [30] H. Yokokawa, T. Horita, K. Yamaji, H. Kishimoto, M.E. Brito, *Journal of the Korean Ceramic Society* 49 (2012) 11-18.

- [31] B. Ozturk, R.J. Fruehan, Metallurgical Transactions 16B (1985) 801.
- [32] Anne-Kristine Meland, Dick Bedeaux, Signe Kjelstrup, J. Phys. Chem. B 2005 109(45) 21380-21388.
- [33] E. Shin, P. Ahn, H. Seo, D. Nguyen, S. Kim, S. Woo, J. Yu, J. Lee, Solid State Ionics 277 (2015) 1-10
- [34] Bernard A. Boukamp, Henry J.M. Bouwmeester, Solid State Ionics 157 (2003) 29-33.
- [35] Vinod M. Janardhanan, Dayadeep S. Monder, J. Electrochem. Soc. 161 (14) F1427-F1436 (2014).
- [36] S. Appari, V. M. Janardhanan, R. Bauri, S. Jayanti, and O. Deutschmann, Appl. Catal. A, 471, 118 (2014)
- [37] K. Karan, A. Mehrotra, L. Behie, American Chemical Society 37 (1998) 4609-4616.
- [38] F. Hiu-Ling, L. Chun-Hu, G. Han-Xian, Journal of Natural Gas Chemistry, Vol. 8 (1999).
- [39] Bustamante, Uncatalyzed and Wall-Catalyzed Forward Water-Gas Shift Reaction Kinetics, Department of Energy.
- [40] J. McKinley, K. Shuler, The Journal of Chemical Physics 28 (1958) 1207.
- [41] T. Ramos, M. Sogaard, M.B. Mogensen, J. Electrochem. Soc. 161(4) (2014) F434-F444.
- [42] Yeging Fu, "Theoretical and Experimental Study of Solid Oxide Fuel Cell (SOFC) Using Impedance Spectra", 2014.
- [43] K. Haga, Y. Shiratori, K. Ito, K. Sasaki, J. Electrochem. Soc. 155 (12) B1233-B1239 (2008)
- [44] K. Sasaki, K. Haga, T. Yoshizumi, D. Minematsu, E. Yuki, R. Liu, C. Uryu, T. Oshima, T. Ogura, Y. Shiratori, K. Ito, M. Koyama, K. Yokomoto, J. Power Sources 196 (2011) 9130-9140

## Chapter 4

---

### Electrochemical Frequency Modulation for Estimating the Exchange Current Density in Solid Oxide Fuel Cells

This text for this chapter was originally prepared for the *Journal of Electrochemical Society Transactions* as “Electrochemical Frequency Modulation for Estimating the Exchange Current Density in Solid Oxide Fuel Cells”; **Debanjan Das**, Derek Hall, Serguei N. Lvov. The paper was accepted for publication in ECS Meeting, San Diego (June 2016)

#### **Preface to Chapter 4**

Electrochemical frequency modulation (EFM) was applied for the first time to solid oxide fuel cells (SOFC) to obtain *effective* exchange current density and transfer coefficient values. Values obtained from EFM data were compared to values obtained from electrochemical impedance spectroscopy (EIS) and linear sweep voltammetry (LSV) to validate the obtained information. An appropriate kinetic model based on Butler-Volmer (B-V) equation was used as the basis for the analysis. It was found that the values obtained via EFM were in good agreement with EIS and Tafel analyses. The obtained values from EFM, EIS and LSV for cell 3 of the SOFC stack closely range from around 11 - 16 mA cm<sup>-2</sup> with excellent repeatability.

#### 4.1. Introduction

Solid Oxide Fuel Cells (SOFC's) are electrochemical energy conversion devices which convert the chemical energy of the fuels, e.g.  $H_2$ ,  $CH_4$ ,  $CO$  and various hydrocarbons into useful electrical energy [1-7]. The electrochemical process involves the oxidation of the fuel at one of the electrodes, which is called the anode simultaneously coupled with the reduction of oxygen at the cathode. Fuel Cells are becoming increasingly popular, primarily due to their lower emissions and higher efficiencies compared to conventional combustions processes. One significant advantage which SOFC's have over other fuel cell types, is that they can work efficiently on a variety of fuels, which gives them inherent fuel flexibility over other systems. Due to a sustained and constant effort by both industry and government, an infrastructure for producing natural gas as a large scale is underway. A market for solid oxide fuel cells is growing especially for stationary power generation applications [1-3].

To ensure that a SOFC stack runs at the optimum efficiency level, degradation studies are critical. Proper diagnostics and post-mortem analysis of the cells by advanced electrochemical and materials characterization techniques help to acquire useful information about the different sources of degradation occurring in the cell [2-4, 22-26]. Electrochemical Impedance Spectroscopy (EIS) is a powerful technique which has the ability to distinguish (in the frequency domain) the internal resistance of each cell of the stack as well as the full stack. Even though EIS helps to localize each different process separately, it does not provide with any direct measurement process on the exchange current density and the Tafel parameters of a solid oxide fuel cell. It requires post acquisition data treatment which takes time for proper reasoning and analysis [5-9, 28]. Exchange current density and Tafel parameters are important kinetic parameters which indicate how fast an electrochemical reaction is proceeding at the electrode surface [27-29]. When a fuel cell stack runs for longer periods of time under various operating regimes, external and internal factors cause the

reactions to slow down significantly. Understanding the kinetic parameters plays a key role in making improved materials types and microstructures, for more efficient SOFC systems for commercial applications. In the research community, not much importance was given to study kinetic parameters in the past and certain models neglected the activation related losses completely. The primary reasons typically relate to the fact that SOFCs operating around very high temperatures such as 1000 °C tend to have significantly lower kinetic losses and high ohmic losses dominate the overall performance barometer of the fuel cell system under normal operating conditions. Also such considerations are viable for older non-planar and tubular solid oxide fuel cells which operated at very high temperatures. But conventional and modern planar geometries operating below 800 °C have shorter current conduction paths and hence can possibly result in comparable activation related losses which can influence the overall cell behavior under normal or certain specified operating conditions [1-4, 20]. Also a common error is to consider the dominant linear region in SOFC voltage-current curves exclusively related to the ohmic losses. It is not a good idea to neglect the contribution of activation and concentration losses completely just because mathematically they are logarithmic functions of current density as we can see from a representative example from a planar fuel cell derived from a PNNL model data [20]. In practical systems, low temperature SOFCs may have smaller exchange current densities and thus can exhibit a behavior under which they can have appreciable activation losses at low operating current which then becomes steady at higher currents [7,8,20].

Intermodulation and harmonic frequency response analysis have been used by a few researchers over the years [11,15-19,56] for understanding the non-linear behavior of electrochemical systems with regards to their reaction mechanism, electrode kinetics and structure of the double layer. In 1962, Neeb first applied the concept of the intermodulation to an electrochemical system [17] by using polarography to study the non-linear behavior of the polarization resistance of an

electrochemical system. According to their work, they proposed that the measurement of the intermodulation components is more useful than only harmonics due to them being unaffected by instrumental distortions. Lopez et al. [18] also used the technique to study the electrochemical double layer and thus expanded its utility to both faradaic and non-faradaic reactions of an electrochemical system. The non-linear frequency response technique has also seen its application recently in the area of fuel cell kinetics and reaction mechanisms such as in direct methanol fuel cell, PEM fuel cell and solid oxide fuel cells [16-20]. According to the primary literature references, there are two main broad categories of non-linear methods in which they can be divided into. The first one initially suggested by Engblom et al. [21] and Gavaghan and Bond [22] is based on the classical ac voltammetry and is referred to as large amplitude ac voltammetry. The above technique class involves the application of an alternating potential of a single frequency with much higher amplitude being superimposed on the input signal. The second and newer class of non-linear technique is based on a sinusoidal perturbation of the system by multiple excitation frequencies around one single operating point [16]. The above mentioned second class can also be further subdivided into three sections (i) methods related to dc rectification and faradaic rectification [22,23] (ii) methods related to the analysis of higher harmonics/intermodulation [23] such as faradaic distortion, electrochemical frequency modulation, intermodulation voltammetry and (iii) methods analyzing the amplitude dependence of the fundamental harmonics on non-linear EIS [25]. The main important aspect to consider is that the various individual techniques used in the range of applications involves the same fundamental concepts but different mathematical treatment and background. The different treatments lie in the analysis and adoption of a variety of possible kinetic models from the theory and applying them to Taylor expansions, Fourier Transforms and Volterra series and hence finding a reasonable solution for them. A series of general steps in the overall procedure of performing analysis and mathematical treatment of an

assumed electrochemical model is clearly explained by Bensmann et al [16]. A similar step-by-step procedure has been adopted in this study by us.

Electrochemical Frequency Modulation (EFM)/ Intermodulation voltammetry has been used extensively in monitoring corrosion processes since its inception over the past 10 years [27-31]. However, minimal or no work has been carried out in application, evaluation and determination of any information on any kinetic parameters for fuel cell applications based on this technique. This work demonstrates the possibility and feasibility of using this non-destructive technique in obtaining valuable information on the kinetic variables in a fuel cell. Linear Sweep Voltammetry (LSV) and EIS are traditionally used methods for kinetic parameters estimation but the concerns with the above mentioned methods are two-fold. The two methods take arbitrary assumptions and simplifications which requires a larger polarization range resulting in an increased measurement time and large overpotential which could possibly lead to a change in electrode surface or damage the microstructure. Another important restriction of the above mentioned techniques is the inaccurate estimation of the Tafel slopes or their determination by extrapolation.

EFM is a small ac excitation technique like EIS. It is different from EIS in the sense that it involves a non-linear potential perturbation signal by two sine waves which generate non-linear current responses at additional frequencies than the frequencies of the applied input signal [11, 28-30]. The additional frequencies are the sum, difference and multiples of the two input frequencies together termed as intermodulation frequencies. Current responses can then be measured at intermodulation frequencies and then can be used with empirical relations to quantify exchange current and the respective Tafel parameters. It is worth mentioning in this case, that the Tafel constants are not required to measure the exchange current density. Both the parameters can be independently measured using EFM which is a significant advantage compared to other electrochemical techniques. The causality factors used in EFM are used to validate the data and

they are an internal check which indicate and confirm the consistency and validity of the measurement process. Any “significant” deviation from these ideal values indicates the quality of the obtained data [11].

This work is an attempt to apply non-linear intermodulation/harmonic measurements for the estimation of the exchange current and Tafel parameters of a single cell from a commercial SOFC stack running on pure hydrogen fuel at the anode and air at the cathode at a temperature of 800 °C. EIS and LSV measurements were also recorded at the same conditions and used as standard tested techniques to compare the results with EFM. Even though the “traditional” methods and EFM are distinct electrochemical methods, comparative analysis of the data obtained, provided a check for the consistency and the relative quality of the values obtained. As mentioned before even though there are some similarities in the non-linear techniques used in case of fuel cells, the mathematical treatment and the selection of the chosen model has varied across researchers depending on its suitability. Consequently this is an effort to consider the most common and simplistic SOFC kinetic model and experimentally determine the kinetic parameters and check their validity. A comparative assessment between this approach and the other non-linear techniques applied in electrochemical systems is beyond the scope of this paper.

Both the exchange current density and transfer coefficients can be independently measured using EFM which is a significant advantage compared to other electrochemical techniques. Despite the advantages of EFM, to our knowledge EFM has yet to be applied to solid oxide fuel cells (SOFCs). This work introduces this non-linear intermodulation/harmonic technique for estimating the exchange current density and Tafel parameters to SOFCs by examining a single cell sub-commercial SOFC stack running on pure hydrogen fuel at a temperature of 750 °C.

## 4.2. Background Theory

### 4.2.1 Exchange Current Density and Butler-Volmer equation

The exchange current density is one of the most important kinetic parameters in electrochemistry. It provides the information on the “speed” of an electrochemical charge transfer reaction and is a direct indication of the performance of the system. In the case of fuel cells, it can be explained as a kind of "idle current" for charge exchange across the electrode interface. It can also be termed as the rate of oxidation and reduction at equilibrium across an electrode surface [6-9]. If a net current is to be drawn which is actually a small fraction of this bidirectional idle current, then only a tiny over-potential will be required to extract it and vice-versa. This implies a better performing fuel cell system where the voltage drop will be much less when extracting large currents. If the exchange current is large, then the system can supply large net currents. This may happen even if there is mass-transfer-limited current, with insignificant or very less activation overpotential. The lower the exchange current, the more sluggish the kinetics are, hence larger the activation overpotential must be for achieving any particular net current. At equilibrium, an electrochemical system is delivering charge across the interfaces at rates much greater than is required. The role of the small overpotential in the case of higher exchange currents is to unbalance the rates in the two directions to a small degree that one of them predominates. If the system has to draw a net current that exceeds the exchange current, the system has to deliver a charge at the required rate which can be done by applying a significant overpotential. This shows that the exchange current is a measure of any system's ability to deliver a net current without a significant energy loss due to activation. The exchange current density is mostly affected by electrode micro-structural properties and also by operational conditions such as nature of the redox reaction, operating temperature and gas composition [6-10].

The relation between electrode overpotential ( $\eta$ ) and current density ( $j$ ) is represented by the Butler-Volmer (B-V) equation, shown here [8.9]:

$$j = j_0 [\exp\{(\alpha_a F/RT) \eta\} - \exp\{(-\alpha_c F/RT) \eta\}] \quad (1)$$

In the above equation  $j$  is the current density in the system,  $j_0$  is the exchange current density,  $\alpha_a$  &  $\alpha_c$  is the transfer coefficient in anodic (forward) and cathodic (reverse) reactions,  $F$  is Faraday's constant,  $R$  is universal gas constant and  $T$  is the absolute temperature. The above equation is the governing equation for the activation overpotential associated with each electrode-electrolyte interface and it is applied individually (or separately) at the anode and the cathode of a particular electrochemical system. The B-V equation accounts for both the forward and reverse currents for a certain interfacial reaction (anodic or cathodic) in the case of a solid oxide fuel cell. In this case only the anodic reaction is considered. At higher anodic overpotentials, the Butler-Volmer equation can be simplified and the backward current can be neglected to give the following equation:

$$j = j_0 [\exp\{(\alpha_a n F/RT) \eta\}] \quad (2)$$

Taking the natural logarithm of both sides and rearranging, yields the relation which is commonly known as the Tafel Equation:

$$\ln j = \ln j_0 + b^{-1} \eta \quad b^{-1} = \alpha_a n F/RT \quad (3)$$

where  $\eta$  is the over-potential,  $j$  is the current density and  $b$  is the Tafel slope. Utilizing equation [3], the raw experimental data is plotted as  $\ln(j)$  against  $\eta$  to obtain the exchange current density ( $j_{0,ex}$ ) as the intercept and the value of the Tafel slope. The measurement of the slope from the Tafel equation is also given great attention and the linear region is chosen at regions with  $\eta \geq RT/F$ . This is one of the major drawbacks of a Tafel analysis which is associated with the uncertainty of the

selection of the linear region in a Tafel curve which at times may lead to incorrect slope estimation. This issue is even bigger when multi-step real world reactions are observed, when the asymmetry parameter has no physical definition or meaning in Butler Volmer kinetics [38, 39]. Nonetheless, these systematic errors are the main motivation for testing the applicability of EFM for kinetic parameter estimation in Solid Oxide Fuel Cells.

All of the above parameters, including the exchange current, the transfer coefficients and the Tafel constants, provide vital information on the kinetics of an electrochemical reaction and helps to estimate how fast or sluggish a reaction is occurring. In the case of solid oxide fuel cells, this information helps to get an idea about any changes or microstructure degradation which might be happening in the anode due to variation in operating and fuel conditions directly impacting the above mentioned kinetic parameters. As a result, measurement and observation of the exchange current and the Tafel parameters becomes important. Electrochemical Impedance Spectroscopy (EIS), Linear and Linear Sweep Voltammetry (LSV) are two useful techniques which can provide such information with reasonable accuracy. Even though the basic concepts and operation are different, they are expected to provide similar values of parameters of the same order with acceptable deviations and can serve as complimentary to each other in predicting fuel cell performance.

Here, EFM is compared with the above mentioned methods to verify its suitability and applicability on getting similar kinetic data

#### *4.2.2 Tafel Slopes and Concept of the Transfer Coefficient ( $\alpha$ )*

The Tafel slopes are directly obtained from the EFM data treatment and used to estimate the anodic and cathodic transfer coefficients which are then incorporated into representative equations to calculate the exchange current density. Due to the reason mentioned before, erroneous

determination of the Tafel slopes through extrapolation is an important drawback of that analysis. Hence in this case, we get the Tafel values from the post analysis of EFM. The higher the Tafel slope, the faster the overpotential increases with the current density. Thus, for an electrochemical reaction to obtain a high current at low overpotential, the reaction should exhibit a low Tafel slope. Tafel slope is an intensive parameter dependent primarily on the electrode materials, microstructure and also temperature but it is independent of the electrode surface area [9].

The transfer coefficient  $\alpha$  is a quantity that is commonly applied to investigate the kinetic response of electrode processes. It should also be noted that most real world electrode reactions occur in several steps, and the transition from the reactants to the products requires the transfer of several electrons [38]. The concept of symmetry factor ( $\beta$ ) is different from the transfer coefficient in the sense that the symmetry factor is strictly defined for a single step electrode reaction and is associated to the shape of the free energy barrier and to the position of the activated complex along the reaction coordinate. In case of a multi-step process such as those occurring at the fuel cell electrodes, it is replaced by an experimental parameter, called the transfer coefficient. It is also worth mentioning that the transfer coefficient is a value calculated after experimental data treatment but the symmetry factor is obtained only after a set of assumptions. Also the sum of the anodic and cathodic symmetry factors will always be unity due to the way it is decided, but it is not necessarily true with respect to the transfer coefficient. Thus  $(\alpha_A + \alpha_C)$  does not necessarily add up to unity for a specific electrochemical reaction mechanism [38-42]. Therefore the value of  $\alpha$  is “experimentally determined” and not “settled or assumed”. In a recently published IUPAC technical report in 2014, Guidelli et al. [39] has recommended and defined quantitatively the expression for both the anodic and cathodic transfer coefficients as:

$$\alpha_A = (RT/F)(1/b_a) \qquad \alpha_C = - (RT/F)(1/b_c) \qquad (4)$$

For an electrode process with the same rate determining step in the cathodic and anodic directions, we have

$$\alpha_A + \alpha_C = n/\nu \quad (5)$$

Here,  $n$  is the number of electrons involved in the process and  $\nu$  is the stoichiometric number which is defined as the frequency of the rate determining step which should occur, to complete the overall reaction. Various researchers have tried to come up with plausible mechanisms of the hydrogen oxidation reaction in a fuel cell to produce water. Even though mechanistic predictions of such complex reaction systems has not been performed with much confidence and are often debatable, but couple of proposed mechanisms are extensively used across research groups [38-46].

#### 4.2.3 Electrochemical Frequency Modulation (EFM)

EFM is a nondestructive electrochemical technique that has the capability of giving values of the corrosion currents without prior knowledge of the Tafel Constants. EFM just like other harmonic methods have the advantage of determining the kinetics of an electrochemical process and Tafel parameters in a short period of time. The original concepts of EFM can be applied on the traditional Butler-Volmer equation as mentioned in the early works on this technique [11, 27-31]. Similar to EIS, EFM is an ac excitation method, where a small signal is applied to the electrochemical system. In EFM two sine waves at different excitation frequencies are generated ( $\omega_1$  and  $\omega_2$ ), which is used to stimulate the cell simultaneously. It is known that current is a non-linear function of potential so that the system also responds in a non-linear way to the potential perturbation. The electrical current contains responses from the input frequencies as well as sum, difference (modulation) and multiples (harmonic) of the two input frequencies. The input signal is represented as below:

where,  $\eta$  is the overpotential,  $U_0$  is the amplitude of the applied signal,  $\omega_1$  and  $\omega_2$  are two different excitation frequencies decided ( $\omega_2 > \omega_1$ ) and chosen with proper considerations. The two frequencies are accordingly selected to optimize the output. The frequencies should be as high as possible so as to reduce the time of operation and be sufficiently low so that the charging of the double layer does not contribute to the current response. The amplitude of the signal excitation is also selected to be as low as possible, just like EIS. In their work, Bosch described empirical relationships between the electrochemical parameters and the current responses at different intermodulation frequencies. The main advantage which EFM has is that the current response at the intermodulation frequencies is not affected by the harmonics of the excitation frequency signal. We speculate that these relations could be used in this case also for calculation of the exchange current density which is synonymous to the corrosion current density in the interpretation of the EFM data for corrosion systems. Fuel cell systems like corrosion systems exhibit strong nonlinear and discontinuous behavior. There is also an internal check device, named as causality factors, which helps to perform a validation of the data and estimate its applicability and also presence of any background noise. The noise could be originating from the instrument or the system under test itself. The causality factors, 2 and 3, are used as baseline data verification to help decide if the data obtained through EFM can be trusted and analyzed further. Significant deviation from the ideal values of 2 and 3, is the result of a system with high disturbance and inconsistent data [11].

### 4.3 Experimental

The solid oxide fuel cell was an anode supported planar stack provided by Delphi Automotive, Michigan. The stack was composed of 5 cells, each of area  $105 \text{ cm}^2$ . The cell consisted of a  $30 \text{ }\mu\text{m}$  Lanthanum Strontium Cobalt Ferrite (LSCF) cathode,  $10 \text{ }\mu\text{m}$  Ytria-Stabilized Zirconia (YSZ) membrane (electrolyte) and a  $500 \text{ }\mu\text{m}$  Ni/YSZ anode. The cells were operated at a temperatures of  $750 \text{ }^\circ\text{C}$ . EFM, EIS and LSV were carried under similar operating conditions and repeated multiple

times for consistency. The anode was supplied with 3 % humidified  $\text{H}_2$  at a flow rate of  $2.5 \text{ L min}^{-1}$ , and the cathode was supplied with air at a flow rate of  $5 \text{ L min}^{-1}$ . For measuring EIS, a Solartron 1252A FRA was used in conjunction with a 1470E Solartron Cell Test System. A two electrode – 4 wire arrangement was used on the stack with the anode as the working electrode, cathode as the counter electrode and two separate wires for carrying the current across the external circuit. The frequency ranged used for the impedance data was from 10 kHz to 0.1 Hz. Circuit Modeling (CM) was performed on the obtained EIS spectra with ZView to determine the corresponding electrochemical parameters. The permissible fitting between the experimental data and considered model was checked using the chi-squared value ( $\sim 10^{-4}$ ) obtained by complex non-linear least squares fitting (CNLS) method [8.9]. Kramers-Kronig (KK) transformations [8] were performed to verify the obtained data quality and validity. HP 6060B was used to perform the linear sweep due to its high current handling capability of 60 A. LSV was carried out with anodic/cathodic overpotential ranging from 0 mV to  $\pm 200 \text{ mV}$ . EFM data was measured by using Gamry Reference 600 and EFM 140 software package. The multiplier frequencies [6] chosen to study the application of EFM were 2 and 5 and the base frequency chosen as 2.5 Hz. Five sets of EIS, LSV and EFM data ( $N = 1 - 5$ ) were recorded at independent times to confirm reproducibility and repeatability of the obtained data. The five data points reported here were taken from the final 3h of measurement (at an interval of  $\sim 45$  minutes), which were observed to be stable enough after the initial 10h of steady state operation. This was performed to verify whether the obtained values drifted significantly with passage of time.

#### 4.4. Results and Discussion

A Nyquist Plot at the open circuit potential ( $E_{\text{OCP}}$ ) ( $\sim 1.13$  V) is shown in Fig. 1a. The obtained EIS data was modeled with an equivalent circuit in the form of a modified Randles circuit as shown in the inset. Mathematical interpretations of the physical elements in relation to electrochemical processes have been given elsewhere [11]. The bounded Warburg element ( $W_s$ ) was considered to simulate the diffusion related process at the anode arising from the low  $\text{H}_2\text{O}$  partial pressure near the electrode surface. In studies, it was repeatedly shown that the high frequency arc corresponded to an activation controlled region of a typical SOFC system fuelled by pure hydrogen and the low frequency arc  $\{R(\text{gas conv})\}$  included the gas conversion impedance. [8,12-14,17-21]. A similar trend was observed here. The high frequency arc ( $R_{\text{ct,eff}}$ ) (centered around 100 Hz) signified the *effective* charge transfer resistance of the system [17,18] as it showed significant dependency on overpotential, operating temperature (as shown in Fig. 1c) and hydrogen/oxygen partial pressure thus corresponding to an activation controlled reaction(s).

In our case, the *effective* exchange current density ( $j_{0,\text{eff}}$ ) is being considered based on some popular works [17,18,20] as the limitations with analyzing combined anode and cathode activation losses in SOFC's by reference electrodes have been documented [27-30].  $j_{0,\text{eff}}$  takes into account electrode kinetics for the composite electrodes and does not include arbitrary assumptions of similar or different activation losses for anode and cathode.  $j_{0,\text{eff}}$  can thus be considered as a kinetic parameter indicating the “true” cell performance taking into account both anodic reaction ( $\text{H}_2 + \text{O}^{2-} \leftrightarrow \text{H}_2\text{O} + 2\text{e}^-$ ) and cathodic reaction ( $\frac{1}{2} \text{O}_2 + 2\text{e}^- \leftrightarrow \frac{1}{2} \text{O}^{2-}$ ).

Regarding EIS, the low field approximation of the Butler-Volmer equation gave the relation for the exchange current density ( $j_{0,\text{eff}}$ ) as follows [8-10],

$$j_{0,\text{eff}} = (RT)/(nFR_{\text{ct-eff}}) \text{ 1/A} \quad (1)$$

where  $F$  is the Faraday's constant,  $R$  is the molar gas constant,  $T$  is the thermodynamic temperature, electron number ( $n$ ) transferred in the overall half-reaction was taken as 2 and  $A$  is the geometric surface area ( $105 \text{ cm}^2$ ). From the fitting of Fig. 4.1a and Table 4.1, the charge transfer resistance from anode was estimated;  $R_{\text{ct-eff}} = 0.025 \text{ } \Omega$ . Therefore, using the equation (1), we get,  $j_{0,\text{eff}}$  (EIS) as  $16.8 \text{ mA cm}^{-2}$ .

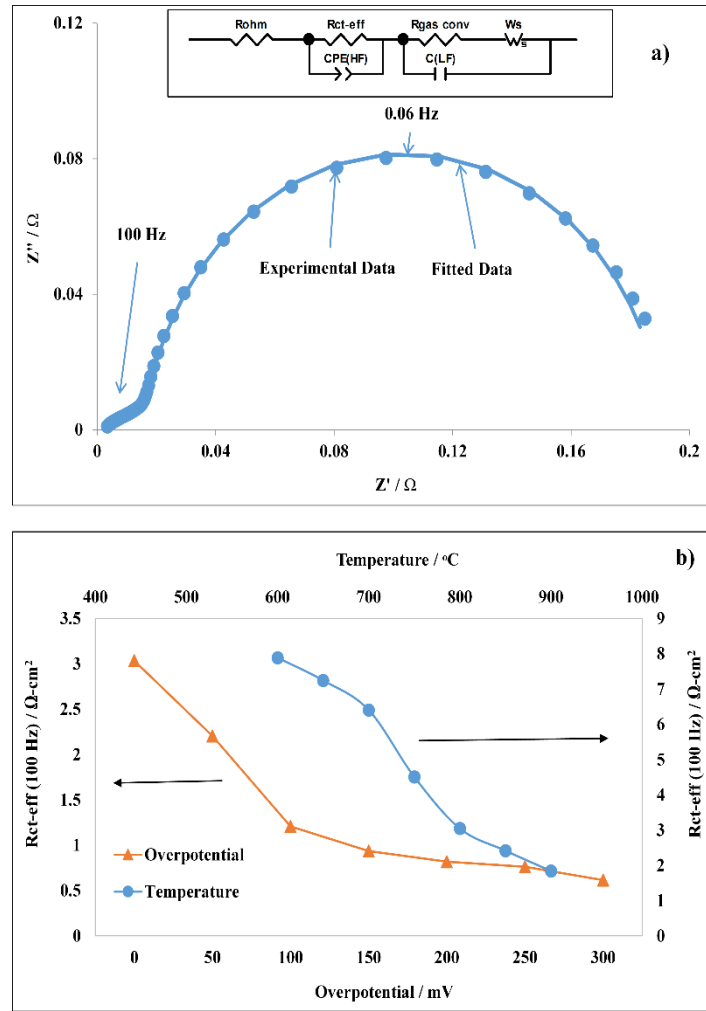


**Fig. 4.1** (a) Nyquist Plot for at OCP at  $750^{\circ}\text{C}$  with fuel: 3 % wet  $\text{H}_2$  (2.5 SLPM), oxidant: Air (5 SLPM). (Inset) Circuit Model fitted by CNLS method to model the experimental data. (b) Impedance parameter trends for cell 3 with varying overpotential and operating temperature, to determine the dependency of the respective arc  $R_{\text{ct-eff}}$  on anodic charge transfer process.

**Table 4.1** Values of the electrochemical parameters obtained from CNLS fitting of the impedance diagram from Fig. 4.1a.

Element/Parameter	Freedom	Value	Error %
$R_2$	Free (+)	0.025	1.2881
$W_S$ -R ( $R_d$ )	Free (+)	0.026278	0.49043
Chi- Squared value : 1.26E-04			
Weighted Sum of Squares : 0.011718			

LSV was performed on the same cell at the same time intervals considered for other electrochemical measurements. The LSV data were corrected for the ohmic drop  $IR_{ohm}$  to evaluate overpotential ( $\eta$ ) on x-axis. The  $R_{ohm}$  values obtained from EIS were used to correct for the ohmic drop and  $E_{OCP}$  values ( $\sim 1.13$  V) were the measured OCP for the cell as shown in equation (2) [21],

$$\eta = E_{FC} - E_{OCP} - IR_{ohm} \quad (2)$$

where  $\eta$  is the overpotential,  $I$  is the measured cell current and  $E_{FC}$  is the measured cell potential. The corresponding LSV plots are shown in Fig. 4.2a. In Fig. 4.2b, the linear part of the Tafel plot in SOFC direction was best fitted by the equation:  $\log_{10} j = 9.988 \eta - 1.82$ . The value of the intercept was used to estimate the value of  $j_{0,eff} (LSV) = 15.13 \text{ mA cm}^{-2}$ . SOEC direction was not considered for reasons explained later.

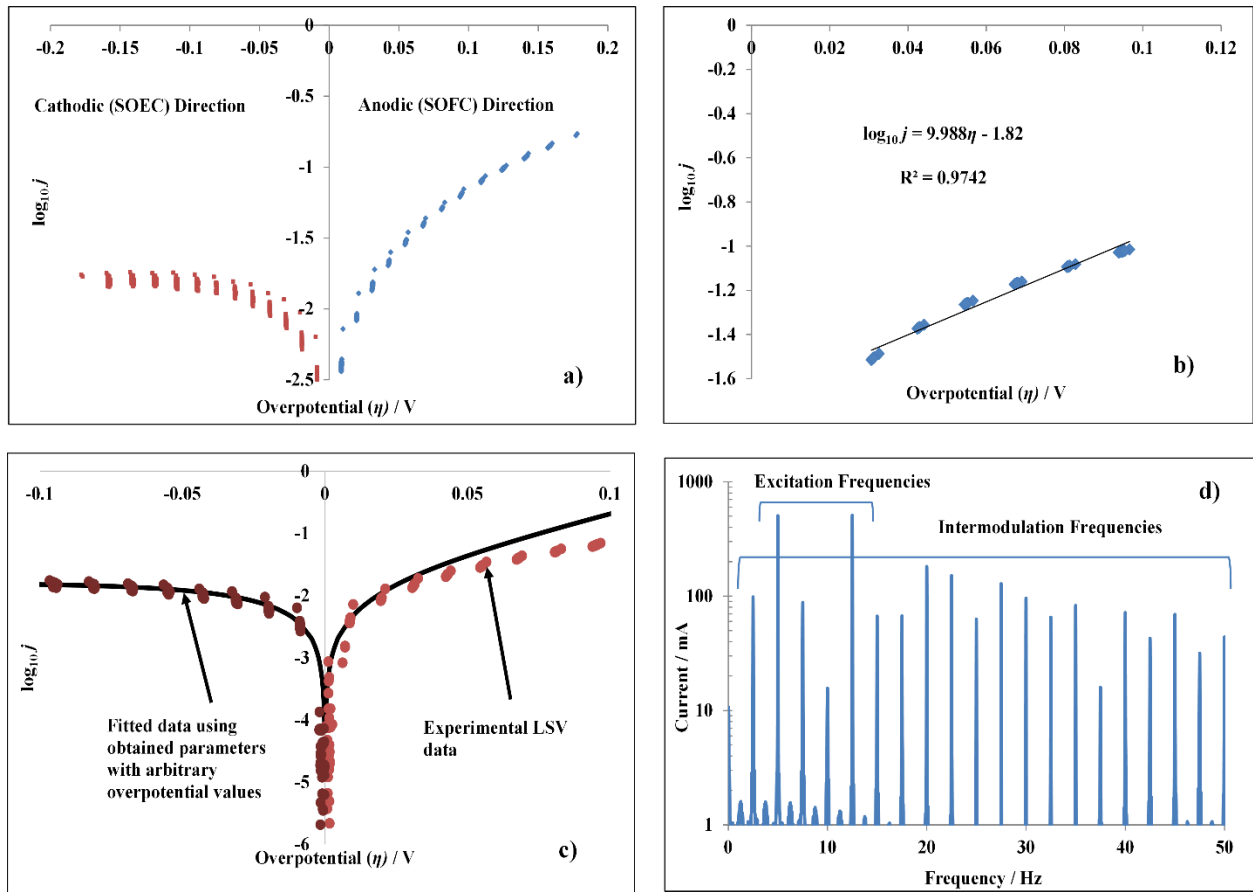


**Fig. 4.2** (a) LSV data for at 750 °C with fuel: 3 % wet H<sub>2</sub> (2.5 SLPM), oxidant: Air (5 SLPM). (b) Straight line fit with the equation for the linear Tafel plot in SOFC mode (c) Comparison between estimated polarization data from obtained parameters (bold line) and experimentally measured LSV data (circles). (d) Electrochemical Frequency Modulation Spectra at 750 °C; Fuel: 3 % Wet H<sub>2</sub> (2.5 SLPM), Oxidant: Air (5 SLPM).

EFM is an ac technique which requires two sine-waves at different excitation frequencies ( $\omega_1$  and  $\omega_2$ ), used to stimulate the cell simultaneously. It is known that current is a non-linear function of potential so that the system also responds in a non-linear way to the potential perturbation. The electrical current contains responses from the input frequencies as well as sum, difference (intermodulation) and multiples (harmonic) of the two input frequencies. The input signal is represented as follows [5,6,16]:

$$\eta = U_0 \sin \omega_1 t + U_0 \sin \omega_2 t \quad (3)$$

where,  $\eta$  is the overpotential,  $U_0$  is the amplitude of the applied signal,  $\omega_1$  and  $\omega_2$  are two different excitation frequencies ( $\omega_2 > \omega_1$ ) chosen with proper considerations in the non-capacitive region of the frequency spectrum and  $t$  is time period. [6].

The electrochemical model applied to determine the kinetic parameters from EFM were obtained from an approximation of the classical B-V equation. The B-V equation included both the directions of the activation process which constituted the SOFC (forward) and the solid oxide electrolytic cell (SOEC) part (backward). The water content in the bulk fuel stream (3 %) resulted in mass transport limited behaviour for the SOEC direction. As evident from Fig. 2a, it reached a limiting current density ( $j_{lim}$ ) in the reverse SOEC direction within  $\sim -30$  mV of the  $E_{OCP}$ . This above observation could be attributed to a transport limited process in the reverse direction near the anode-electrolyte-gas phase triple phase boundaries. The anodic (forward) part for the cell was a purely activation controlled process.

Therefore, in SOEC direction at the specified overpotential range the Tafel slope was assumed as infinity (parallel to x-axis) for this specific condition. The anodic side was considered as forward direction (SOFC) and cathodic side was considered as reverse (SOEC). The current-potential relationship of the cell was given by the generalized B-V equation assuming a single electron transfer rate determining step below including the  $j_{lim}$  term in the reverse direction [9,10,23]. The current-potential relationship was given by the generalized B-V equation considering a single rate determining step below including the  $j_{lim}$  term in the reverse direction [9,10,22],

$$j = j_{0,eff} \left[ \exp \left\{ \left( \frac{\alpha_f F}{RT} \right) \eta \right\} - \left\{ 1 - \frac{j}{j_{lim}} \right\} \exp \left\{ \left( \frac{-\alpha_b F}{RT} \right) \eta \right\} \right] \quad (4)$$

where  $j$  is the current density,  $\alpha_f$  is the forward transfer coefficient,  $\alpha_b$  is the backward transfer coefficient.  $j_{0,eff}$  can be considered an analogous term and treated in the same way as a conventional anodic or cathodic exchange current density [4].

Simplifying equation (4),

$$j = j_{0,eff} \left[ \exp \left\{ \frac{\eta}{b_f} \right\} - \left\{ 1 - \frac{j}{j_{lim}} \right\} \exp \left\{ \frac{-\eta}{b_b} \right\} \right] \quad (5)$$

where  $b_f$  (forward Tafel slope) =  $RT/\alpha_f F$  and  $b_b$  (backward Tafel slope) =  $RT/\alpha_b F$ . From discussed before, the SOEC Tafel slope ( $b_b$ ) is assumed infinity ( $\alpha_b = 0$ ) under diffusion-controlled reverse mode. The equation (5) thus reduces to,

$$j = j_{0,eff} \left[ \exp \left\{ \frac{\eta}{b_f} \right\} - \left\{ 1 - \frac{j}{j_{lim}} \right\} \right] \quad (6)$$

Rearranging equation (6) we get,

$$j = \frac{\left[ \exp \left\{ \frac{\eta}{b_f} \right\} - 1 \right]}{\frac{1}{j_{0,eff}} - \frac{1}{j_{lim}}} \quad (7)$$

An input distortion signal according to EFM (equation 3) was applied to the system and using Taylor series expansion and mathematical simplifications as adopted by Bosch et al. [6], the expressions for estimating  $j_{0,eff}$  and  $\beta_a$  were derived for this model below,

$$\frac{j_{0,eff}}{1 - \frac{j_{0,eff}}{j_{lim}}} = \frac{i_{\omega_1, \omega_2}}{2i_{\omega_2 \pm \omega_1}} \quad (8)$$

$$\beta_a = \frac{i_{\omega_1, \omega_2}}{2i_{\omega_2 \pm \omega_1}} U_0 \quad (9)$$

where  $i_{\omega_1, \omega_2}$  are the averaged current density at the respective perturbation frequencies ( $\omega_1, \omega_2$ ),  $i_{\omega_2 \pm \omega_1}$  are the averaged current density at the respective intermodulation frequencies ( $\omega_2 + \omega_1, \omega_2 - \omega_1$ ).

Interestingly, the harmonic and intermodulation components can be internally related as well to check the validity and applicability of the obtained data through the term causality factors [6]

$$i_{\omega 2 \pm \omega 1} = 2 i_{2\omega 1, 2\omega 2} \quad \text{and} \quad i_{2\omega 2 \pm \omega 1} = 3 i_{3\omega 1, 3\omega 2} \quad (10)$$

Therefore the causality factors (C.F.) can be defined as,

$$\text{C. F. (2)} = \frac{i_{\omega 2 \pm \omega 1}}{i_{2\omega 1, 2\omega 2}} \quad (11)$$

$$\text{C. F. (3)} = \frac{i_{2\omega 2 \pm \omega 1}}{i_{3\omega 1, 3\omega 2}} \quad (12)$$

The EFM spectra is shown in Fig. 4.2d and the value of the obtained harmonic and intermodulation current components are as below in Table 4.2,

The  $j_{\text{lim}}$  was estimated as 17.9 mA cm<sup>-2</sup> from Fig. 4.2a.  $j_{\text{lim}}$  can alternatively be calculated from the resistance term of the Warburg element ( $R_d$ ) in the impedance plot from the relation below [15];

$$j_{\text{lim}} = \frac{RT}{nFAR_d} \quad (13)$$

From circuit modelling,  $R_d$  was obtained as 0.026278  $\Omega$  from the Warburg ( $W_s$ ) parameter estimation in Fig. 4.1b. The  $j_{\text{lim}}$  was estimated from EIS as 16.1 mA cm<sup>-2</sup>. Therefore the values of  $j_{\text{lim}}$  from both EIS and LSV were quite similar and can be considered consistent. Rearranging equation (8) for  $j_{0,\text{eff}}$  and using obtained EFM current components,  $j_{0,\text{eff}}$  (EFM) was calculated as 11.21 mA cm<sup>-2</sup>.

**Table 4.2** Current components obtained with EFM for the corresponding excitation, harmonic and intermodulation frequencies.

Current component	Angular frequency (rad s <sup>-1</sup> )	Frequency (Hz)	Current (mA)	Averaged Current (mA)
$i_{\omega_1, \omega_2}$	$\omega_1$	5	694.90	694.7
	$\omega_2$	12.5	693.89	
$i_{\omega_2 \pm \omega_1}$	$\omega_2 - \omega_1$	7.5	87.94	77.52
	$\omega_2 + \omega_1$	17.5	67.10	
$i_{2\omega_2 \pm \omega_1}$	$\omega_2 - 2\omega_1$	2.5	98.38	131.64
	$2\omega_2 - \omega_1$	20	181.20	
	$\omega_2 + 2\omega_1$	22.5	151.14	
	$2\omega_2 + \omega_1$	30	95.87	
$i_{2\omega_1, 2\omega_2}$	$2\omega_1$	10	15.65	39.175
	$2\omega_2$	25	62.70	
$i_{3\omega_1, 3\omega_2}$	$3\omega_1$	15	66.73	41.325
	$3\omega_2$	37.5	15.92	

To validate the data, the causality factors were obtained as mentioned before using equation (11) and (12);

$$C.F.(2) = 1.978$$

$$C.F.(3) = 3.185$$

Thus it was observed that the data was causal and followed close relationship between the harmonic and intermodulation frequencies. This confirmed the validity of the obtained data.

The anodic Tafel slope can also be calculated from EFM and compared with the one obtained from LSV data. From equation (9), the estimated Tafel slope was,

$$\beta_{a, \text{EFM}} = 79 \text{ mV decade}^{-1}$$

The forward transfer coefficient ( $\alpha_f$ ) according to IUPAC recommendations 2014 [23], can be calculated as follows;

$$\alpha_{f, \text{EFM}} = \frac{RT}{F} \frac{1}{b_{f, \text{EFM}}} = 1.13 \quad (14)$$

From Fig. 4.2b, the Tafel slope is numerically equal to the inverse of the slope = 100 mV decade<sup>-1</sup>. Similarly,  $\alpha_{f, \text{LSV}} = 0.88$

With the obtained parameters from EFM, it is possible to predict the current-potential relationship of the tested electrochemical cell. Arbitrary  $\eta$  were considered from 0 V to  $\pm 0.15$  V and using  $j_{0, \text{eff}}$  (EFM) as 11.21 mA cm<sup>-2</sup>,  $j_{\text{lim}}$  as 17.86 mA cm<sup>-2</sup> and  $\alpha_{f, \text{EFM}} = 1.13$  in equation (4), the corresponding  $j$  was calculated. The calculated plot was compared with the actual experimental LSV data in Fig. 2c. It was seen that the simulated and measured polarization have excellent agreement and show close correspondence in both directions. This indicates that the parameters determined by EFM measurements are reliable enough when compared with EIS and LSV. The results provide information that the data obtained were valid and consistent for the specific kinetic model and operating conditions. Moreover, the results give proof that equation (4) can predict with reasonable accuracy the  $\eta$ - $j$  relationship in a SOFC at intermediate temperatures and primary fuel being pure H<sub>2</sub> with very less humidification. It is however important to note that the results in this paper cannot be considered as fingerprint values for a fundamental charge transfer step of the anodic/cathodic reactions for various fuel conditions at the same/different temperature and pressure. The obtained  $j_{0, \text{eff}}$  and  $\alpha_f$  values were compared with the values reported by other authors

for SOFC's with similar conditions and seemed to match reasonably well. Giorgi et al. [13-15] obtained experimentally, values of exchange current density in SOFC mode ranging from 10-30 mA cm<sup>-2</sup> from 750 - 850 °C. Thomsen et al. [25] and Fueyo et al. [21] found that for a Ni/YSZ – LSCF cell, in the SOFC direction, charge transfer coefficients were typically 1.1–1.5, and were independent of either temperature or p<sub>H2O</sub>.  $j_0$  described by empirical equations showing partial pressure dependencies and an Arrhenius-type temperature dependency [21, 22, 26] also ranged from 20-35 mA cm<sup>-2</sup>.

It was observed that the values obtained reasonably match in all the three electrochemical techniques and was of the same order of magnitude. It is well known from literature that EIS and LSV could be used for the calculation of exchange current density. But in this work, we successfully proposed and confirmed the use of another useful AC technique, EFM, in obtaining the value of the exchange current directly from in-situ testing. The advantage of EFM is that, it is a non-destructive technique and also is completed within a shorter period of time. The values obtained for the exchange current are included in Table 4.3 for all the data acquisition points  $N = 1$  to  $N = 5$ . One important aspect which is to be considered was the use of different equipment in obtaining the different data which accounts for slight variations in the  $j_{0,\text{eff}}$  values obtained after data treatment.

**Table 4.3** Comparative values of the Exchange Current Density Obtained from EIS, LSV, and EFM

<b>Data Acquisition Point</b>	<b><math>j_{0,\text{eff}}</math> (mA cm<sup>-2</sup>) EIS</b>	<b><math>j_{0,\text{eff}}</math> (mA cm<sup>-2</sup>) LSV - Tafel</b>	<b><math>j_{0,\text{eff}}</math> (mA cm<sup>-2</sup>) EFM</b>
<b><math>N = 1</math></b>	16.305	16.987	11.856
<b><math>N = 2</math></b>	18.818	15.796	11.814
<b><math>N = 3</math></b>	16.634	14.265	10.450
<b><math>N = 4</math></b>	17.415	14.256	12.915
<b><math>N = 5</math></b>	16.743	15.045	11.189

The exchange current density is a critical factor in determining the performance of a SOFC. It is a measure of the kinetics of the electrochemical charge transfer reaction. In this work, the operating conditions used were standard including the fuel used (Pure H<sub>2</sub>). While carrying out the degradation analysis of fuel cell stacks under other hydrocarbon fuels and simulated reformat streams, it becomes useful to monitor the change of the exchange current density. This helps to judge how and to what extent the cell degradation is occurring with regards to change in electrochemical properties due to modification in the microstructural properties or operating conditions. In some cases, there are various inorganic impurities present in hydrocarbon fuel streams. This affects the fuel cell by reacting with the anode microstructure or by altering the shape and size of the active catalyst surface & particles by reducing the amount of available triple phase reaction sites for electrochemical reaction. In such instances, a direct change in the exchange current density is observed in some cases, which makes it even more imperative to measure them in the course of time of operation for a typical fuel cell system. Even though EIS has been used extensively in monitoring global degradation in SOFCs by measuring trends in cell resistances with time, continuous *in-situ* measurement of the exchange current also adds a great diagnostic value to the overall data acquisition process.  $j_{0,eff}$  values can provide good information regarding any change in surface oxidation/reduction reactions occurring at the interface between the electrolyte-electrode-gas phase boundaries. EIS often takes a reasonable amount of time to perform one cycle of test within which depending on the materials and process conditions, the electrode response may or may not change or drift especially at very low frequencies. With LSV, due to polarizing the electrode to wide potential range, it may lead to a change in the electrode surface. In spite of that, researchers have used them quite successfully in their measurement processes. EFM simply adds flexibility to the entire picture and helps to measure the parameter by an independent method which gives the value of the exchange current without much extensive post-testing data analysis and treatment. Thus the theoretical analysis which follows any EIS and LSV measurement

can be well complimented by the EFM data directly obtained from the software. The obtained data (harmonic and intermodulation current components) can then readily be substituted into the derived model equations and the exchange current density value can be approximately calculated.

#### 4.5. Conclusion

It was shown for the first time to our knowledge that EFM can be successfully used for extracting kinetic parameters on SOFCs and the current-potential relationship for a cell in pure  $H_2$  at 750 °C was successfully predicted using electrochemical parameters extracted from three techniques (EFM, EIS and LSV). EFM can be used as a quick and non-destructive ac technique for estimating  $j_{0,eff}$  without previous knowledge of Tafel slopes.  $j_{0,eff}$  from EFM in our case was  $\sim 11.21 \text{ mA cm}^{-2}$  and the values showed close correspondence when compared with conventional electrochemical techniques such as EIS ( $\sim 16.8 \text{ mA cm}^{-2}$ ) and LSV ( $\sim 14.3 \text{ mA cm}^{-2}$ ). A calculated polarization trend from parameters obtained through EFM showed good relationship with the experimentally measured polarization data. EFM is more advantageous than EIS or LSV due to its fast data acquisition nature which can be beneficial in rapid performance monitoring of commercial SOFC systems over a long period of time. Also due to LSV being carried out at high overpotential, there remains a chance of surface alteration which can be undesirable. EIS has limitations with being time consuming and does not provide information on Tafel slopes. It is not our objective to suggest that EIS and LSV are less important electrochemical methods for kinetic parameter estimation. However, they have their own constraints. EFM can act as a complementary technique which provides reasonable accuracy with respect to kinetic analysis. Application of EFM on more complex SOFC systems can be specifically studied on a case-by-case basis with proper electrochemical model considerations under different operating conditions.

## References – Chapter 4

- [1] K. Darowicki, Corrosion Sci. 37 (6) (1995) 913–925
- [2] J. Jankowski, Corrosion Reviews, 20 (2002) 179
- [3] Esra Kus, Florian Mansfield, Corrosion Science 48 (2006) 965-979
- [4] J. Larminie, A. Dicks, Fuel Cell Systems Explained, 2nd ed, Wiley, 2003
- [5] T. Kadyk, R. Hanke-Rauschenbach, K. Sundmacher, J. Electroanal. Chem. 630 (2009) 19
- [6] R.W. Bosch, J. Hubrecht, W.F. Bogaerts, B.C. Syrett, Corrosion, 2001
- [7] Boris Bensmann, Menka Petkovska, Tanja Vidakovic-Koch, Richard Hanke-Rauschenbach, Kai Sundmacher, J. Electrochem. Soc. 157 (9) (2010) B1279-B1289
- [8] E. Barsuokov, J.R. Macdonald, Impedance Spectroscopy Theory, Experiment and Applications, Second Edition: John Wiley and Sons, 2005
- [9] Bard, Faulkner, 2nd ed, Electrochemical Methods: Fundamentals and Applications, Wiley, 2001
- [10] Eliezer Gileadi, Electrode Kinetics for Chemists, Chemical Engineers and Materials Scientists, Wiley 1993.
- [11] M. Sluyters-Rehbach, Impedances of electrochemical systems: Terminology, nomenclature and representation - Part I: Cells with metal electrodes and liquid solutions (IUPAC Recommendations 1994), Pure Appl. Chem. 66 (1994) 1831–1891.
- [12] John S. Newman, Electrochemical Systems, Prentice Hall, 1991
- [13] Julie S. O'Brien, Javier B. Giorgi, J. Power Sources 200 (2012) 14-20
- [14] Catherine M. Grgicak, Malgosia M. Pakulska, Julie S. O'Brien, Javier B. Giorgi, J. Power Sources 183 (2008) 26-33
- [15] Julie S. O'Brien, Javier B. Giorgi, ECS Transactions 28 (33) (2010) 221-231
- [16] Y. Matsuzaki, I. Yasudu, Solid State Ionics 132 (2000) 271-278

- [17] C. Tanner, K. Fung, A. Virkar, J. Electrochem Soc 144 (1997) 21-30
- [18] A. Virkar, J. Chen, C. Tanner, J. Kim, Solid State Ionics 131 (2000) 189-198
- [19] Sanchit Khurana, Mark LaBarbera, Mark V. Fedkin, Serguei N. Lvov, Harry Abernathy, Kirk Gerdes, J. Power Sources 274 (2015) 1049-1054.
- [20] S.C Singhal, M. Dokiya, Solid Oxide Fuel Cells (SOFC VI): Proceedings of the Sixth International, 19 (1999) 832-837
- [21] M. Garcia Camprubi, S. Izquierdo, N. Fueyo, Renewable and Sustainable Energy Reviews 33 (2014) 701-718
- [22] A. Utz, H. Stormer, A. Leonide, A. Weber, E. Ivers-Tiffée, J. Electrochem Soc 157 (6) (2010) B920-B930
- [23] D. Hall, J. Beck, S.N. Lvov, Electrochemistry Communications 57 (2015) 74-77.
- [24] Rolando Guidelli, Richard G. Compton, Juan M. Feliu, Eliezer Gileadi, Jacek Lipkowski, Wolfgang Schmickler, Sergio Trasatti, IUPAC Technical Report 2014.
- [25] O. A. Marina, L. R. Pederson, M. C. Williams, G. W. Coffey, K. D. Meinhardt, C. D. Nguyen, and E. C. Thomsen, J. Electrochem Soc. 154 (5) (2007) B452-B459
- [26] T. Yonekura, Y. Tachikawa, T. Yoshizumi, Y. Shiratori, K. Ito and K. Sasaki, ECS Transactions 35(1) (2011) 1007-1014
- [27] S. Adler, J. Electrochem. Soc. 149 (2002) E166-E172.
- [28] S. Adler, B. Henderson, M. Wilson, D. Taylor, R. Richards, Solid State Ionics 134 (2000) 35-42.
- [29] S. McIntosh, S.B. Adler, J.M. Vohs, R.J. Gorte, Electrochem. Solid-State Lett. 7 (2004) A111-A114.
- [30] S. McIntosh, J. Vohs, R. Gorte, J. Electrochem. Soc. 150 (2003) A1305-A1312

## Chapter 5

---

### **Sensitivity Studies of Fuel Characteristics and State of Health Investigation of a Planar SOFC Short Stack Operating on Syngas by Electrochemical Impedance Spectroscopy**

This text for this chapter was originally prepared for the *Journal of Electrochemical Society Transactions* as “Sensitivity Studies of Fuel Characteristics and State of Health Investigation of a Planar SOFC Short Stack Operating on Syngas by Electrochemical Impedance Spectroscopy”; **Debanjan Das**, Serguei N. Lvov. The paper was accepted for publication in ECS Meeting, San Diego (June 2016)

#### **Preface to Chapter 5**

An approach based on Electrochemical Impedance Spectroscopy (EIS) was formulated and investigated to understand the most efficient fuel conditions for suitable long term operation of a solid oxide fuel cell stack under power generation conditions. The procedure helped to reflect the individual effects of CO/H<sub>2</sub> volumetric ratio, S/C ratio and fuel utilization under the presence of a simulated alternative fuel at 0.4 A cm<sup>-2</sup>. Signature impedance plots were obtained with variation of each parameters and subsequent circuit modelling is used to calculate the electrochemical resistances associated with the plots. It was seen that the impedance plots show an additional arc at lower frequencies attributed to the diffusion of CO during the water gas shift reaction near the anode ( $\text{CO} + \text{H}_2\text{O} \rightarrow \text{H}_2 + \text{CO}$ ). Tests with various CO/H<sub>2</sub> ratio helped to narrow down the operating regimes where CO electro-oxidation was expected to take an important part with H<sub>2</sub> oxidation. S/C ratios less than 2 were tested to understand the limits of non-carbon-anode

interaction region without reducing system efficiency. Optimum fuel utilization was obtained for cell operation, highlighting regions having a negative effect on performance. Finally, 8 different combinations of the optimized parameters were tested long term with the stack, and the most efficient blend was determined.

## 1. Introduction

There inherent advantages which SOFCs have over other types of fuel cells improves their capability and flexibility to work on a different ranges of hydrocarbon fuels with good electrical efficiency and mechanical stability [1-4]. Sustained efforts are also being carried out to develop advanced electrode materials for anode catalysts which would work on steam reformed fuels as well as directly fed fuels such as hydrogen, natural gas, bio-gas and other higher hydrocarbon fuels [1-12, 15-18]. At such high operating temperatures, the SOFC can utilize the methane present in the natural gas and catalyzes the endothermic direct reforming and water-gas shift reactions. However direct usage of such hydrocarbon fuels or in pre-reformed condition, may also cause degradation by poisoning the SOFC stacks due to the presence of inorganic contaminants, carbon deposition reactions and also electrode delamination [17,18]. Additionally a few other operating and physical factors such as fuel utilization, operating temperature, Steam to Carbon ratio,  $H_2/CO$  ratio, operating pressure, current cycling, thermal cycling etc. are important aspects for study as pointed by various researchers [14-19]. To our knowledge, studies on State-Of-Health (SOH) analysis on sub-commercial level SOFC systems have been limited perhaps due to restricted availability of such system infrastructures across academic laboratories. While significant efforts have been made to study miniature button cells and their performance [5-8, 17-23], it is equally important to understand the behavior of scaled-up robust SOFC systems under conventional testing conditions to check system variability and degradation characteristics by advanced electrochemical (experimental and modeling) techniques.

Electrochemical Impedance Spectroscopy (EIS) is a sophisticated technique which helps to characterize the stack performance and distinguish, identify and separate the various electrochemical processes occurring near the electrode on different time scales [13]. Research efforts in the last decade has provided effective ways to study physical processes and associate

them to the corresponding EIS diagram. Even though there exists a little confusion and ambiguity among researchers regarding proper interpretation of EIS data, still it can provide useful information on degradation dynamics and performance measurement of SOFC systems.

In this work, we aim at the detailed electrochemical characterization of a sub-commercial 5-cell short stack. The stack was an intermediate temperature planar SOFC type. Two different types of fuels were used in the study namely pure hydrogen/nitrogen blend and a simulated diesel reformat blend or syngas. The primary objective of the work was to test the stack behavior in response to real fuel feed from a hypothetical reformer. But the anodic flow-rate required to maintain normal operation was very high for a short stack. Thus corresponding simulated reformat streams were considered according to results obtained from researchers [8-10, 17, 20] to make the response as close as possible to a system running on pre-reformed fuel. Three important process factors and their dependency on cell performance were tested which included  $H_2/CO$  ratio, Steam-Carbon (S/C) ratio and fuel utilization %. Impedance diagrams in conjunction with I-V curves and best fit circuit models helped to confirm cell operation quantitatively and understand their response with respect to the parameters mentioned above across time scales. Also, the impedance contributions from the electrodes were successfully identified and separated along with their individual variations with different operating conditions. Finally long term SOH tests of 500 h each were carried out for the experimentally determined and optimized process conditions. This paper intends to contribute towards the current research efforts in the characterization of larger SOFC systems with higher power generation capabilities and understand the factors which probably impacts the performance in a more significant nature.

## 2. Experimental

The solid oxide fuel cell was an anode supported planar stack provided by Delphi Automotive, Michigan [11, 12]. The stack was composed of 5 cells, each of area  $105\text{ cm}^2$ . The cell consisted of a  $30\text{ }\mu\text{m}$  Lanthanum Strontium Cobalt Ferrite (LSCF) cathode,  $10\text{ }\mu\text{m}$  Ytria-Stabilized Zirconia (YSZ) membrane (electrolyte) and a  $500\text{ }\mu\text{m}$  Ni/YSZ anode. The cells were operated at a temperatures of  $750\text{ }^\circ\text{C}$ . The simulated hydrocarbon reformate stream was assembled from different individual fuel streams and passed through a manifold structure to allow for proper mixing and stable flow. The composition which was selected was according to the previous work in our lab with Song et al. [5-8] based on their reformer results. For all the tests, a composition blend of  $\text{H}_2$ ,  $\text{CO}$ ,  $\text{CO}_2$ ,  $\text{CH}_4$  and  $\text{H}_2\text{O}$  was selected and fed to the anode of the fuel cell while air is used as the oxidant on the cathode side. The flow rates maintained were in the SLPM/  $\text{L min}^{-1}$  (Standard Liquid per Minute) range for both anodic and cathodic flows. For measuring EIS, a Solartron 1252A FRA was used in conjunction with a 1470E Solartron Cell Test System. A two electrode – 4 wire arrangement was used on the stack with the anode as the working electrode, cathode as the counter electrode and two separate wires for carrying the current across the external circuit. The frequency ranged used for the impedance data was from  $10\text{ kHz}$  to  $0.1\text{ Hz}$ . Circuit Modeling (CM) was performed on the obtained EIS spectra with ZView to determine the corresponding electrochemical parameters. The permissible fitting between the experimental data and considered model was checked using the chi-squared value ( $\sim 10^{-4}$ ) obtained by complex non-linear least squares fitting (CNLS) method [13]. Kramers-Kronig (KK) transformations [13] were performed to verify the obtained data quality and validity. HP 6060B was used to perform the linear sweep due to its high current handling capability of  $60\text{ A}$ . Polarization behavior was observed ranging from OCP to  $0.6\text{ V}$ . A Kepco BOP was also used in conjunction with the Solartron to perform EIS at high current conditions on the stack. The Op-Amp transforms the small

AC perturbation voltage from the Solartron to an equivalent AC current response and subsequently applies it on top of the DC current supplied to the stack by the HP 6060B.

### 3. Results & Discussion

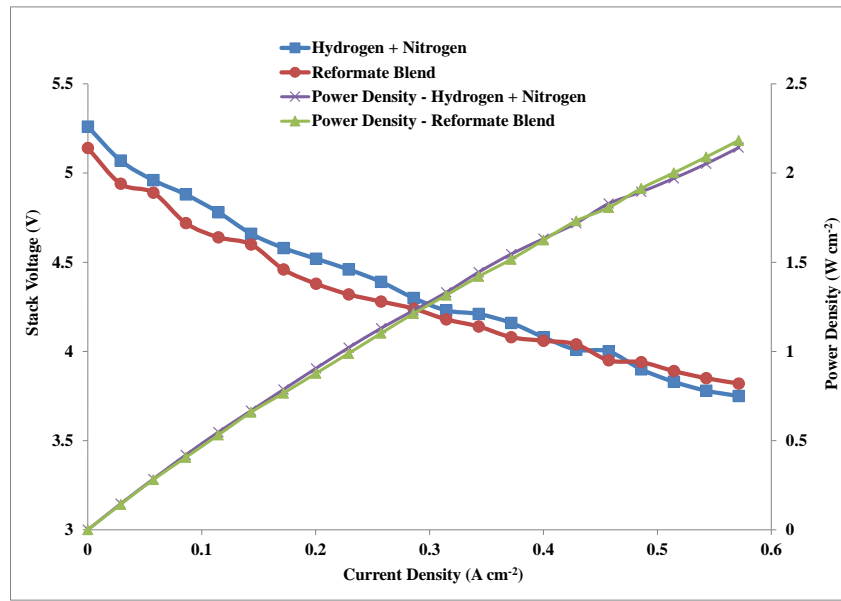
#### 3.1 Baseline DC Polarization Behavior

Fig. 5.1 shows the polarization curves performed for Hydrogen/Nitrogen and a simulated hydrocarbon reformed fuel. The fuel composition, flow-rate and S/C ratio used in the two cases are shown in Table 5.1. The baseline reformat composition was selected from an optimized point of view considering the composition of general bio-hydrogen reformed streams obtained by various researchers [19-22]. The OCP for the hydrogen fuel was estimated as 5.26 V and for the reformat blend it was 5.14 V. This behavior was expected in case of the reformat blend which can be directly inferred from the thermodynamic point of view and the Nernst equation {1} obtained below by a combination of both the theoretical equations for the H<sub>2</sub> and CO oxidation.

$$E = E_0 + (RT/nF) \{ \ln([CO][H_2][O_2]) / ([H_2O][CO_2]) \} \quad \{1\}$$

**Table 5.1** Composition of Hydrogen and Reformat blend used for baselines current –potential and impedance plots

	Base H <sub>2</sub> Fuel	Base Reformat Blend
H <sub>2</sub>	48.5 %	49 %
CO	-	11 %
CO <sub>2</sub>	-	6 %
H <sub>2</sub> O	3 %	15 %
CH <sub>4</sub>	-	19 %
N <sub>2</sub>	48.5 %	-



**Fig. 5.1** Polarization plots showing stack voltage and power density with respect to current run on baseline fuel conditions.

It was also interesting to observe that till a current density of  $0.3 \text{ A cm}^{-2}$ , the reformate mixture showed a reduced performance in power output generated by the cell. At this low current density range, the flux of oxygen ions through the YSZ electrolyte into the anode triple phase sites was lesser. It is known that  $\text{H}_2$  is a light gas and its diffusion coefficient is much higher than CO. When the current density was increased beyond a threshold value, the additional oxygen flux allowed CO species to contribute towards the electro-oxidation process in addition to  $\text{H}_2$  showing comparable performances for both blends. In addition to the above mentioned reasons, another possibility of a comparable performance between the two fuel blends was the possibility for the water gas shift reaction. The steam which was provided along with reformate blend was mainly aimed at inhibiting the Boudouard reaction below and other side reactions [9-10, 19-24] to prevent any undesired deposition of coke or carbon from CO and  $\text{CH}_4$  in the fuel mixture.



When the main bulk fuel stream entered the high temperature assembly, the steam in the inlet feed was used for preventing reaction (1) and other side reactions originating from pyrolysis of  $\text{CH}_4$  to form coke or soot. In the process, the shift reaction also initiated conversion of a part of  $\text{CO}$  to  $\text{H}_2$ . The unreacted steam usually was expected to leave the system exhaust along with unreacted  $\text{CO}_2$  as inert species. Thus the most important function of the above process was primarily to prevent deactivation of catalyst sites by carbon deposition. Ghonem et al. [30] postulated in their work that,  $\text{CO}$  electro-oxidation on Ni catalysts was a three step adsorption-charge transfer process. But  $\text{CO}$  was strongly chemisorbed only on the surface of the catalyst where the reaction took place. Due to a reduced tendency to diffuse through the porous structure, the adsorbed species do not reach the internal triple phase sites as effectively as  $\text{H}_2$  resulting in slower reaction rates. At higher current density regions between  $0.4 \text{ A cm}^{-2} - 0.6 \text{ A cm}^{-2}$  due to a higher oxygen flux, the  $\text{CO}$  species which participated in the oxidation at the anode surface also was also speculated to undergo shift reaction from the additional water produced from the electrochemical oxidation of hydrogen. Thus it was believed to result in additional hydrogen formation which can readily transport and diffuse to the porous active sites increasing the global electro-oxidation efficiency.

### *3.2 Baseline AC Impedance Behavior*

The impedance spectra for the cell at the two fuel conditions at OCP mode and current density  $0.4 \text{ A cm}^{-2}$  is shown in Fig. 5.2a and 5.2b respectively. The hydrogen content in terms of the moles delivered to the anode feed of the fuel cell was kept to understand the main differences contributed by the carbonaceous species part of the reformate blend.

It was observed that the trend and nature of the impedance curves obtained in both cases (zero current & polarized) had differences between the responses of two fuel types. It was observed that

there were two main processes signified by two time constants in the hydrogen case while there were three different time constants for the reformat case. In general according to literature [5-8, 13, 23-27], arcs pertaining to high frequency region pertained to charge transfer processes while arcs in the low frequency region corresponded to transport or diffusion processes. Having said that, there is no fixed rule for assigning every impedance spectrum to typical process definitions and thus it is ambiguous to generalize every case.

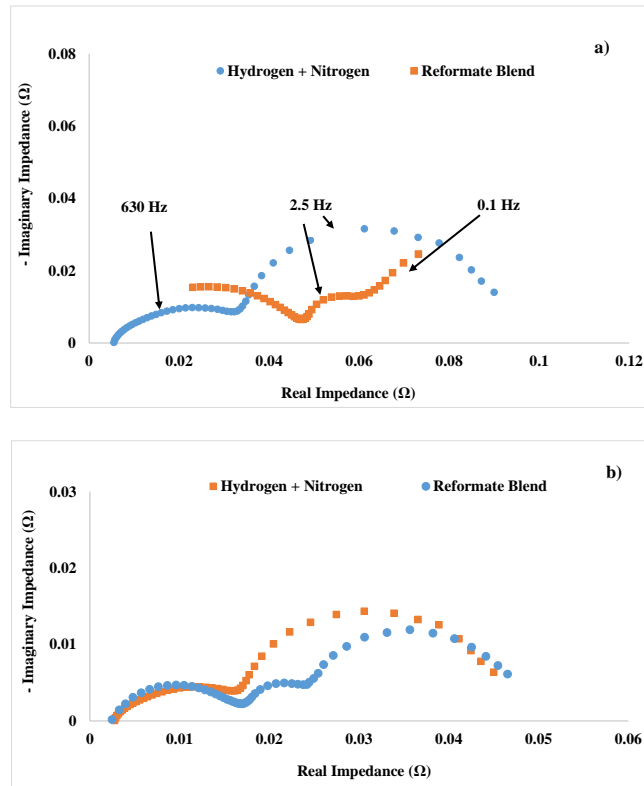


**Fig. 5.2 (a)** Impedance spectra of the SOFC stack at 750 °C exposed to hydrogen fuel and reformat blend at OCP mode with fuel flow - 5 L min<sup>-1</sup>, air flow - 10 L min<sup>-1</sup>, S/C = 2 **(b)** Impedance spectra of the SOFC stack at 750 °C exposed to hydrogen fuel and reformat blend at 0.4 A cm<sup>-2</sup> with same conditions.

Fig. 5.3 shows the two best fit circuit diagrams to model the impedance behavior obtained. The hydrogen blend EIS data was fitted with two RC time constants as shown in Fig. 5.3a and reformat blend was fitted with three RC time constants as shown in Fig 5.3b. The obtained values for the

respective area specific resistances were obtained for both the fuel blends at OCP and polarized conditions, and are summarized in Table 5.2.

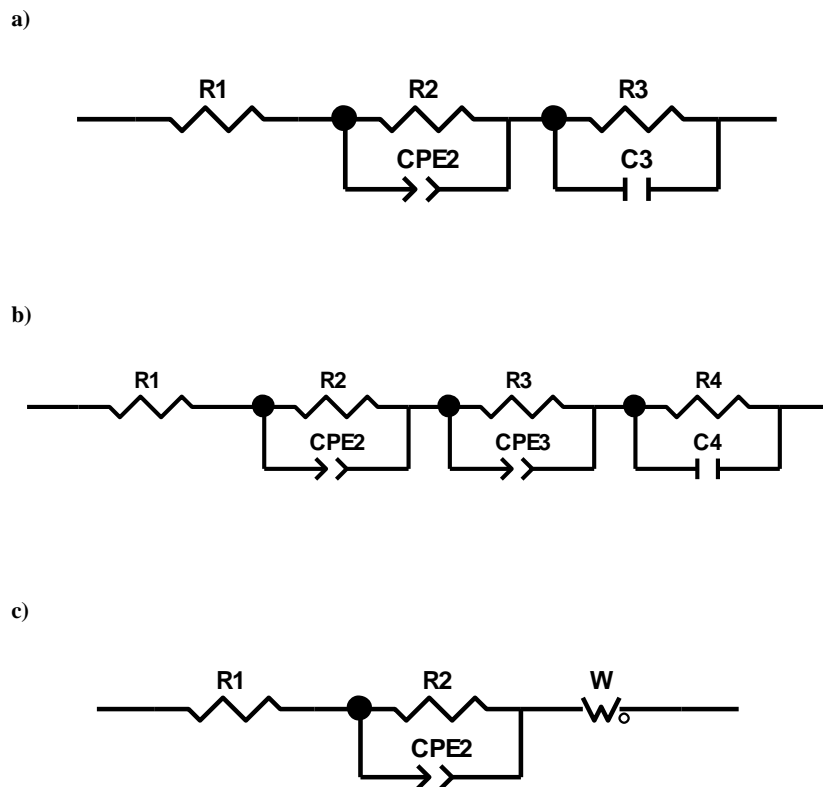


**Fig. 5.3** Circuit Model fitted by CNLS method to model the (a) baseline experimental data for hydrogen fuel (b) baseline experimental data for reformate blend and (c) impedance data obtained from S/C values of 0.95, 0.83 and 0.62.

**Table 5.2** Electrochemical resistances obtained from the CNLS fitting for Hydrogen and Reformate blend used for baselines impedance plots.

	$R_{1\text{H}_2\text{-BL}} (\Omega)$	$R_{2\text{H}_2\text{-BL}} (\Omega)$	$R_{3\text{H}_2\text{-BL}} (\Omega)$	$R_{4\text{H}_2\text{-BL}} (\Omega)$
<b>Hydrogen + Nitrogen (OCP)</b>	0.0053	0.0289	0.0564	-
<b>Hydrogen + Nitrogen (Polarized)</b>	0.0027	0.0140	0.0280	-
	$R_{1\text{REF-BL}} (\Omega)$	$R_{2\text{REF-BL}} (\Omega)$	$R_{3\text{REF-BL}} (\Omega)$	$R_{4\text{REF-BL}} (\Omega)$
<b>Reformate Blend (OCP)</b>	0.0045	0.0420	0.0105	0.0375
<b>Reformate Blend (Polarized)</b>	0.0026	0.0120	0.008	0.0220

As shown in Fig. 5.4, the area specific resistance (ASR) of first arc (high frequency  $R_{2\text{H}_2\text{-BL}}$ ) in the case of hydrogen was believed to be related to the charge transfer resistance due to its dependence on temperature and overpotential. The second arc (low frequency arc  $R_{3\text{H}_2\text{-BL}}$ ) was mainly associated to bulk mass transport or interfacial resistance and gas conversion impedance as it mainly depended on water partial pressure. Also, the negligible dependency of  $R_{3\text{H}_2\text{-BL}}$  on temperature further reiterate its association to gas diffusion. In the case of reformate streams in Fig. 5.2, the three respective arcs at different time scales can be termed as high (summit frequency  $\sim 630$  Hz), mid (summit frequency  $\sim 2.5$  Hz) and low frequency regimes (summit frequency  $\sim 0.1$  Hz). The high frequency region was observed to behave and respond similarly just like the hydrogen spectra and contributed towards the global electro-oxidation process through charge transfer. In this case though, this high frequency region was believed to constitute both the  $\text{H}_2$  and CO oxidation at the anode catalytic sites. The mid frequency region and the corresponding arc depended primarily on the  $\text{H}_2$  flow-rate which indicated towards a bulk  $\text{H}_2$  transport process. This

region was thus dominated by the diffusion of  $H_2$  into the porous anode structure through the  $H_2$  and steam (produced by the electro-oxidation of  $H_2$ ) mixture formed near the anode surface. This behavior was similar to the one obtained for the low frequency arc in case of the impedance spectra for the hydrogen fuel case.

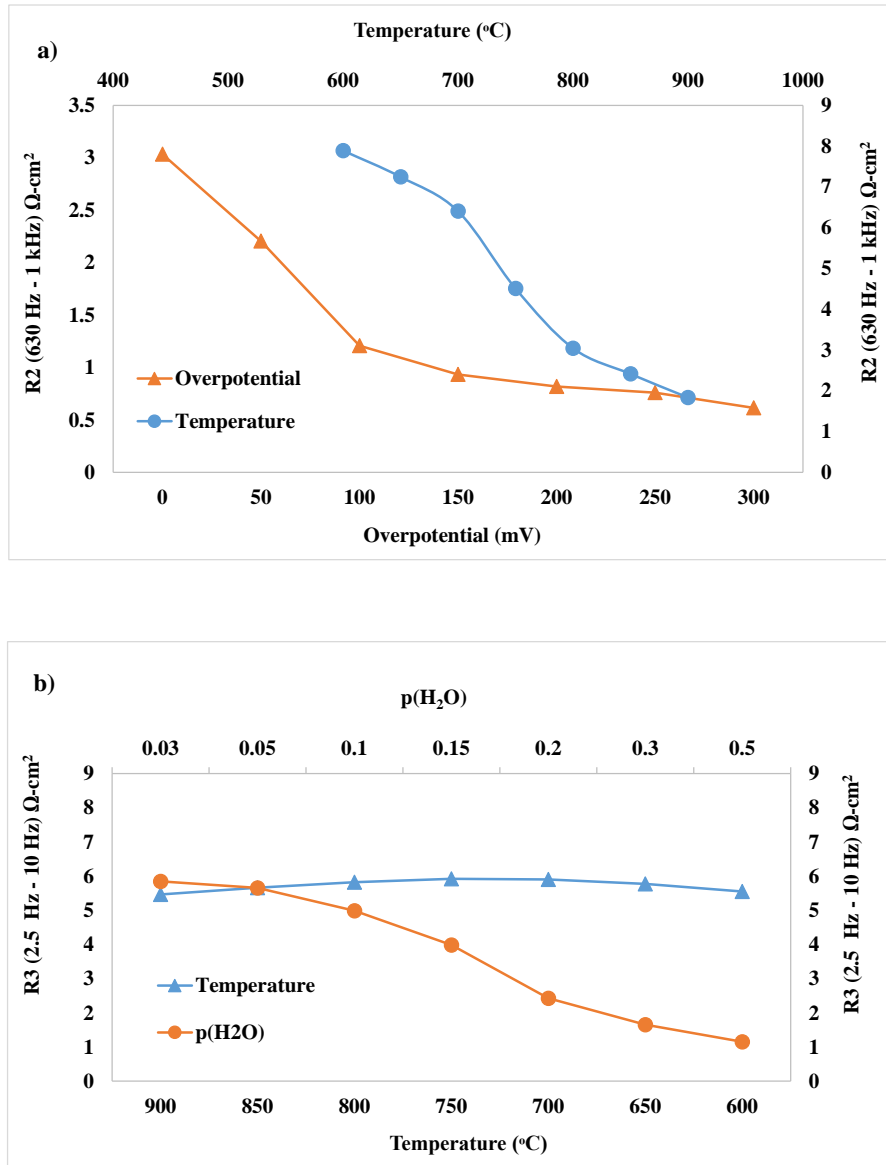


**Fig. 5.4** (a) Parameter dependency of  $R_2$  (630 Hz – 1 kHz) on overpotential and temperature. (b) Parameter dependency of  $R_3$  (2.5 Hz – 10 Hz) on  $H_2O$  partial pressure and temperature.

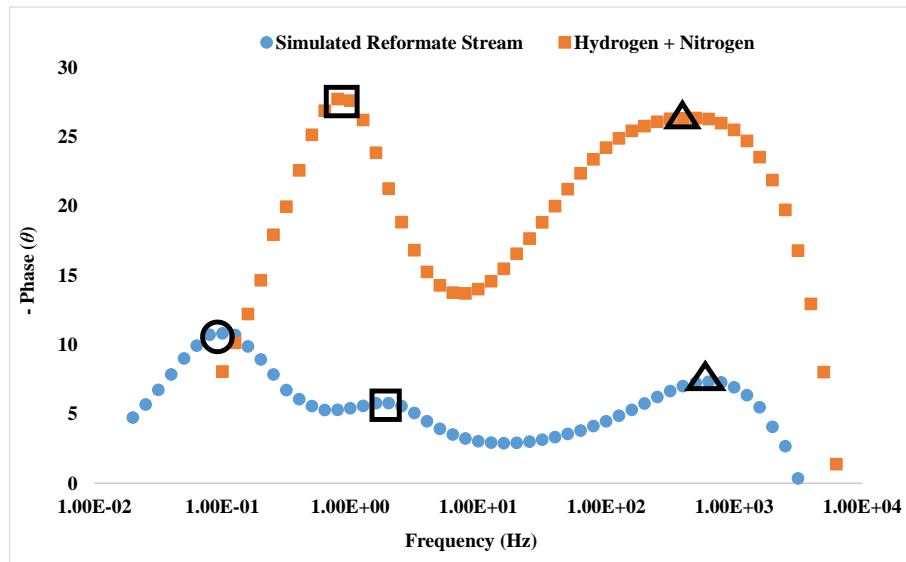


**Fig. 5.5** Bode plot (phase angle v/s logarithmic frequency) showing the respective peaks (rectangular boxes) for the hydrogen fuel and reformate blend across a frequency range of 1 kHz to 0.05 Hz

Fig. 5.5 shows the comparison for the two fuel cases with respect to the phase angle in the Bode plot. It clearly shows that two time constants centered around 1000 Hz (high frequency) and 1 Hz (low frequency) almost overlapped each other. The above observation further pointed towards two similar processes occurring on the same time scales in the system on two different fuel conditions. The low frequency region (third arc) centered around 0.1 Hz from Fig. 5.5 in case of the reformate fuel was the differentiating factor between the two data sets. It explicitly indicated that there was an additional process visible at a slower time scale after changing the fuel stream. Due to the fact that the time constant appeared at a much higher time scale pointed towards a process with comparatively slower reaction rate than competing processes. As it did not appear before the mid frequency arc, it can be safely concluded that it did not belong to a charge transfer related mechanism. Therefore another diffusion or mass transport related process was believed to contribute towards this. Because this process was slower than hydrogen diffusion arc it indicated towards diffusion related process involving CO and CO<sub>2</sub> near the catalyst surface. The water gas

shift reaction was expected to be the dominant reaction governing this portion of the frequency spectrum. The above observation seemed to match reasonably with findings of other researchers [22, 26, 28].

Fig. 5.2b shows the behavior under similar fuel conditions but in current generation mode at  $0.4 \text{ A cm}^{-2}$ . It was previously seen that the performance in the polarization curve for both combinations almost coincided at higher current densities. Thus impedance plots were recorded at a particular current density to understand and compare the differences (if any) in stack behavior. It was seen that the charge transfer resistance (high frequency arc) decreased by a reasonable margin for both the fuels when current was passed through the system. In the OCP case, the high frequency resistance in case of reformat was higher than the hydrogen fuel and but in current density conditions, the same arc was actually smaller in value than the hydrogen fuel one. Even though the overall polarization impedance (total real impedance intercept minus the ohmic resistance) was quite similar in both cases from Fig. 5.2b, the reduction in the charge transfer resistance was quite apparent. This observation matched with the polarization data finding at high current conditions when the performance coincided. It was thus understood that the extent of reduction in charge transfer impedance for reformat case was higher than hydrogen fuel at polarized conditions. This finally led to a comparable performance at polarized conditions for both the fuel.

Interestingly the high frequency arc for reformat  $R_{2\text{REF-BL}}$  was slightly lesser than the hydrogen fuel  $R_{2\text{H}_2\text{-BL}}$  in polarized conditions ( $0.012 \Omega$  vs  $0.014 \Omega$ ) which was different from the OCP case ( $0.042 \Omega$  vs  $0.0289 \Omega$ ). While its ratio was almost  $\sim 1$  in polarized conditions, it increased to 1.45 at OCP. This can mean an improved charge transfer process with reformat at polarized conditions within a specific range also observed from Fig. 5.2b. Thus a higher oxygen flux in polarized

conditions can initiate a higher surface oxidation rate of the adsorbed CO species and additional  $H_2$  produced from shift reaction of CO.

The mid/low frequency regime which governed  $R_{3H_2-BL}$  arc in Hydrogen fuel ( $0.0564 \Omega$  at OCP and  $0.0280 \Omega$  at  $0.4 A cm^{-2}$ ) and  $R_{3REF-BL} + R_{4REF-BL}$  in reformat (  $0.048 \Omega$  at OCP and  $0.03 \Omega$  at  $0.4 A cm^{-2}$ ) had comparable values. It was believed that the impedance reduced accordingly by  $\sim 50 \%$  for the hydrogen and  $\sim 38 \%$  for the reformat in polarized state due to higher fuel conversion and gaseous diffusion. However if we consider the two fuels, at any particular condition (OCP or polarized), the difference between them in respect to total impedance was minimal. Therefore for both the different blends, it was reiterated that performance was comparable in this section of the frequency response diagram. The dependency of  $R_{3REF-BL}$  and  $R_{4REF-BL}$  on other process conditions such as steam ratio and fuel utilization and its related influence on performance was studied later in the paper. The ohmic resistance ( $R_{1H_2-BL}$  and  $R_{1REF-BL}$ ) in both fuel cases at OCP conditions was almost similar at  $0.0054 \Omega - 0.0045 \Omega$  which translated to an ASR of  $0.567 \Omega\text{-cm}^2$ -  $0.4725 \Omega\text{-cm}^2$ . But it was observed that when the conditions were polarized, the ASR reduced to  $0.283 \Omega\text{-cm}^2$ -  $0.273 \Omega\text{-cm}^2$ . The above behavior can be due to the activation of the ionic transport pathways in the anode triple phase boundaries in current generation conditions.

### *3.3 Impact of CO/H<sub>2</sub> volumetric composition ratio*

The tuning of reformat compositions is also an important characteristic to study their effect on the performance of the SOFC stack. We know that CO can act as a species for electro-oxidation at the anode catalyst like  $H_2$  and it also acts an oxidation species in the shift reaction .Therefore, it is useful to understand the range of composition ratios and limits of operation to get the most optimum condition for stack operation.

**Table 5.3** Range of compositions used for Reformate blend with varying CO/H<sub>2</sub> ( $X_f$ ) values.

	$X_f = 0.25$ CO % = 15	$X_f = 0.33$ CO % = 20	$X_f = 0.41$ CO % = 25	$X_f = 0.50$ CO % = 30	$X_f = 0.58$ CO % = 35	$X_f = 0.66$ CO % = 40
<b>H<sub>2</sub></b>	45 %	40 %	35 %	30 %	25 %	15 %
<b>CO</b>	15 %	20 %	25 %	30 %	35 %	40 %
<b>CO<sub>2</sub></b>	6 %	6 %	6 %	6 %	6 %	6 %
<b>H<sub>2</sub>O</b>	15 %	15 %	15 %	15 %	15 %	15 %
<b>CH<sub>4</sub></b>	19 %	19 %	19 %	19 %	19 %	19 %

Five fuel compositions were considered which had a constant total fuel flow-rate of 10 L min<sup>-1</sup>. The total (H<sub>2</sub> + CO) percentage was kept constant at 60 % in order to keep the volume of electrochemically reacting species constant. The CO % range was varied from 15 % - 40 % considering, the maximum amount of CO in a reformed carbonaceous fuel in standard systems was within 40 % [22, 24]. A detailed composition is shown in Table 5.3. The impedance curves were recorded in polarized conditions at a current density of 0.4 A cm<sup>-2</sup>. S/C ratio of ~ 2 was kept constant. For ease of treatment, CO amount in the fuel feed was represented as a ratio factor in the following equation,

$$X_f = [\text{CO}] / ([\text{CO}] + [\text{H}_2])$$

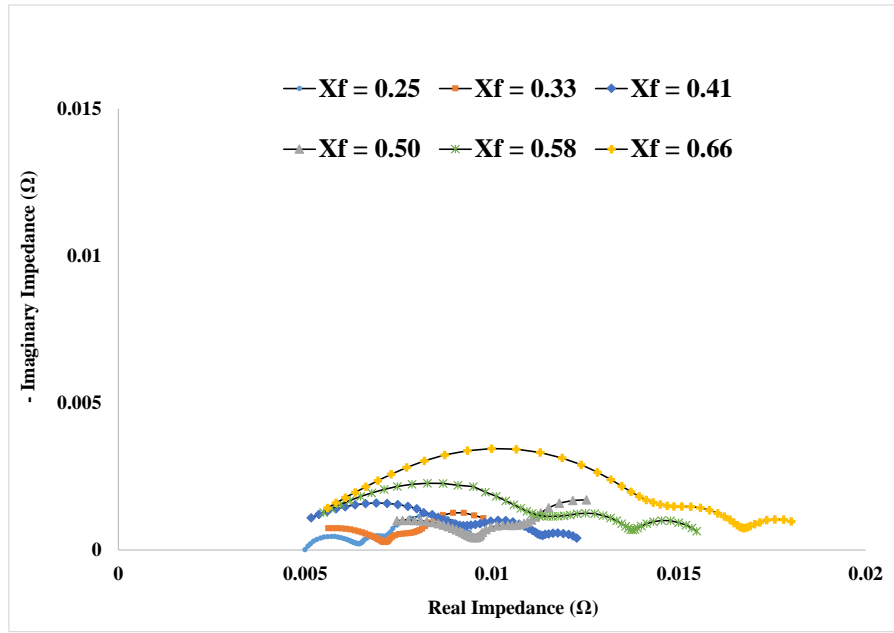


**Fig. 5.6** Impedance spectra of the SOFC stack at 750 °C exposed to reformat blend at 0.4 A cm<sup>-2</sup> with varying CO:H<sub>2</sub> ( $X_f$ ) ratios fuel flow - 5 L min<sup>-1</sup>, air flow - 10 L min<sup>-1</sup>, S/C = 2

**Table 5.4** Electrochemical resistances obtained from the CNLS fitting for Reformat blend with varying CO/H<sub>2</sub> ( $X_f$ ) values.

	$X_f = 0.25$ CO % = 15	$X_f = 0.33$ CO % = 20	$X_f = 0.41$ CO % = 25	$X_f = 0.50$ CO % = 30	$X_f = 0.58$ CO % = 35	$X_f = 0.66$ CO % = 40
$R_{1Xf}$	0.0050	0.0042	0.0042	0.0047	0.0045	0.0047
$R_{2Xf}$	0.0029	0.0030	0.0050	0.0040	0.0072	0.0104
$R_{3Xf}$	0.0014	0.0014	0.0012	0.0015	0.0020	0.0023
$R_{4Xf}$	0.0022	0.0023	0.0023	0.0033	0.0017	0.0018
$R_p$ ( $R_{2Xf} + R_{3Xf} + R_{4Xf}$ )	0.0065	0.0067	0.0093	0.0084	0.0109	0.0139
$\omega_{R2}$	630.96	630.96	501.99	501.99	251.19	125.89

Fig. 5.6 shows the impedance spectra recorded at the various  $X_f$  values. A similar trend was observed in impedance plots like the previous section. Table 5.4 shows the fitted resistance values at the different data points.  $R_1$  was the ohmic resistance which almost remained constant for all the cases as seen from Table 5.4. The most interesting change was observed in the values of the  $R_{2Xf}$  which mainly pertained to charge transfer related resistance. It was seen that  $R_{2Xf}$  in general increased when the CO % was increased 15 % to 40 % from  $0.0013 \Omega$  to  $0.0104 \Omega$  (ASR of  $0.1365 \Omega\text{-cm}^2$  to  $1.092 \Omega\text{-cm}^2$ ). This was mainly due to a reducing  $H_2$  partial pressure in the fuel mixture added to the fact that CO electro-oxidation was a slower process than  $H_2$  oxidation on the active anode surface. CO oxidation mainly occurred on the surface and the adsorbed species did not diffuse into the porous triple phase boundaries to improve charge transfer and electron production process [23, 25]. Interestingly it was found that around  $X_f$  values in the range of 0.41-0.5, the value of  $R_{2Xf}$  actually decreased by  $0.001 \Omega$  (ASR of  $0.105 \Omega\text{-cm}^2$ ) thus resulting in the reduction of the overall polarization resistance as seen from Table 5.4. The  $R_p$  at  $X_f = 0.5$  actually gave the lowest value compared to all other conditions. Therefore there can be two possibilities for such a behavior as understood from conceptual speculation. One reason can be associated to the fact that at the corresponding  $X_f$  value range, the water gas shift reaction reached equilibrium much faster which resulted in an increased  $H_2$  production near the electrode. A higher  $H_2$  content increased the rate of surface oxidation processes which represented the change of trend in  $R_{2Xf}$  values. Also another possible reason can be the subsequent competing oxidation of CO species at the anode surface at optimum CO % in the mixture. Simultaneous  $H_2$  and CO oxidation reactions can occur thereby increasing the rate of charge transfer in the anode. Now, by either of the above two probable processes there would be possible introduction of  $CO_2$  into the system. At this point it is important to mention the dependencies of arc  $R_{3Xf}$  and  $R_{4Xf}$  on  $H_2/H_2O$  diffusion and  $CO/CO_2$  diffusion/water gas shift reaction respectively through the anode porous structure [30]. The  $R_{4Xf}$  value increased from  $0.0023 \Omega$  to  $0.0033 \Omega$  (ASR of  $0.2415 \Omega\text{-cm}^2$  to  $0.3465 \Omega\text{-cm}^2$ ) at the above  $X_f$  range further

implying the additional CO conversion and transport of CO/CO<sub>2</sub> across the porous anode structure. Meanwhile, there was very less noticeable increase in arc  $R_{3X_f}$  which directly meant a comparable amount of water being formed from the previous conditions. It should also be noted that the percentage of water in the fuel mixture also increased accordingly with increase in  $X_f$ . Hence, it can be safely said that around this composition figure, the portion of CO/CO<sub>2</sub> near the anode surface increases at a faster rate than H<sub>2</sub>/H<sub>2</sub>O. This indicated that the electrochemical oxidation at the anode was equally dominated by H<sub>2</sub> and CO, and no additional H<sub>2</sub>O was being formed in the reaction scheme. The water required for shift reactions was balanced by the water produced in the electrochemical oxidation and the change in H<sub>2</sub>/H<sub>2</sub>O diffusion process represented by arc  $R_{3X_f}$  was minimal. Also values of the associated frequency ( $\omega_{R2}$ ) which governed the charge transfer oxidation reaction at the anode was shown in Table 5.4. It was observed than in the first four  $X_f$  data points the frequency associated did not change much and ranged within a lesser spread. This mainly indicated the fact that during that composition ranges, H<sub>2</sub> oxidation was the dominant reaction. It can also be said that at these concentration ranges, there were minimal or less significant effects of water-gas shift reaction. At  $X_f$  values of 0.41 and 0.5, the frequencies values similar at ~ 501.99 Hz. At these same data points, the value of  $R_{2X_f}$  did not increase (actually reduced) and were almost similar. Both of the above data observations strongly pointed towards a combined (H<sub>2</sub> + CO) electro-oxidation process in this concentration range in addition to reasons stated earlier. The above explanations reiterated the fact that H<sub>2</sub> and CO both contributed towards the cell current/potential and CO did not just contribute towards the shift reaction only. But this behavior was obtained in a definite composition range in our work and seemed to deviate at other conditions. This was different from results obtained by other researchers [14-18] who inferred that H<sub>2</sub> was the only primary fuel species for electrochemical oxidation.

When the  $X_f$  reached 0.58 and 0.66, the rate of increase in the overall polarization resistance from Table 5.4 can be attributed to three probable reasons. The most obvious reason can be related to the dilution effect induced by the increased water content in the fuel stream for keeping S/C ratio  $\sim 2$  to avoid carbon deposition. The second reason can be the occurrence of the shift reaction at higher CO and H<sub>2</sub>O concentrations. Even though it produced additional H<sub>2</sub> in the system, inert CO<sub>2</sub> formed during the reaction near the active reaction sites can limit the transport of H<sub>2</sub> through the porous anode which was evident by the increasing values of  $R_{2_{Xf}}$  and  $R_{3_{Xf}}$ . As already explained, CO/CO<sub>2</sub> diffusion arc  $R_{4_{Xf}}$  decreased for the last two conditions signifying CO being utilized in the shift process. The third probable reason can be associated to a possibility of minimal carbon deposition. Even though there was enough steam provided to the system to prevent the Boudouard reaction and other parasitic pyrolysis reactions, carbon poisoning through methanation reactions can be possible at high temperatures. A typical such reaction can be represented as below,



At higher CO partial pressures, as indicated by previous researchers [17, 18], CO reduction by H<sub>2</sub> is a possible mechanism for carbon deposition. There can also be possible heterogeneous reverse water gas shift reaction re-converting some of the H<sub>2</sub> to CO after the reaction reaches equilibrium. Also due to the fast nature of the reaction, Ni can serve as an appropriate catalyst for the reverse reaction at high temperatures [9, 10, 24-26].

### *3.4 Impact of low Steam to Carbon (S/C) ratio*

It is a known fact that carbon damage mitigation is an important cause of concern in SOFC systems running on carbonaceous fuels [22, 28-33]. Especially in commercial systems which should have greater stability and more longevity, management and knowledge of operating conditions is critical to maintain optimum performance with minimal or no damage. Microscopic

analysis has always been important [31, 32] but it's very cumbersome and difficult to perform real time acquisition with it especially on larger electrochemical systems. Usually it has been well established that for proper non carbon deposition conditions, S/C ratio of greater than 2 is required. Even though this benefit comes with the assurance of no carbon damage, but the efficiency of electrochemical systems gets reduced directly resulting in reduced peak power density which is an important parameter from an engineering point of view. Thus, knowledge of carbon interaction with the anode is important especially in case of negligence or accidental conditions when commercial system might run into conditions favorable for carbon effects.

In our work, a minimum S/C ratio of 2 was considered for initial tests. But lower S/C ratios were considered in this part to check for the type of effects in stack performance represented by finger print impedance plots. Therefore data was collected at six S/C ratios of 1.65, 1.42, 1.21, 0.95, 0.83 and 0.62 in polarized conditions of  $0.4 \text{ A cm}^{-2}$ . The base fuel composition selected was in the vicinity of  $X_f$  of 0.5 and composed of 35 %  $\text{H}_2$ , 35 %  $\text{CO}$ , 8 %  $\text{CO}_2$  and 22 %  $\text{CH}_4$ . Each S/C condition was kept for 2 hours before taking measurement to allow the system to stabilize and reach equilibrium.

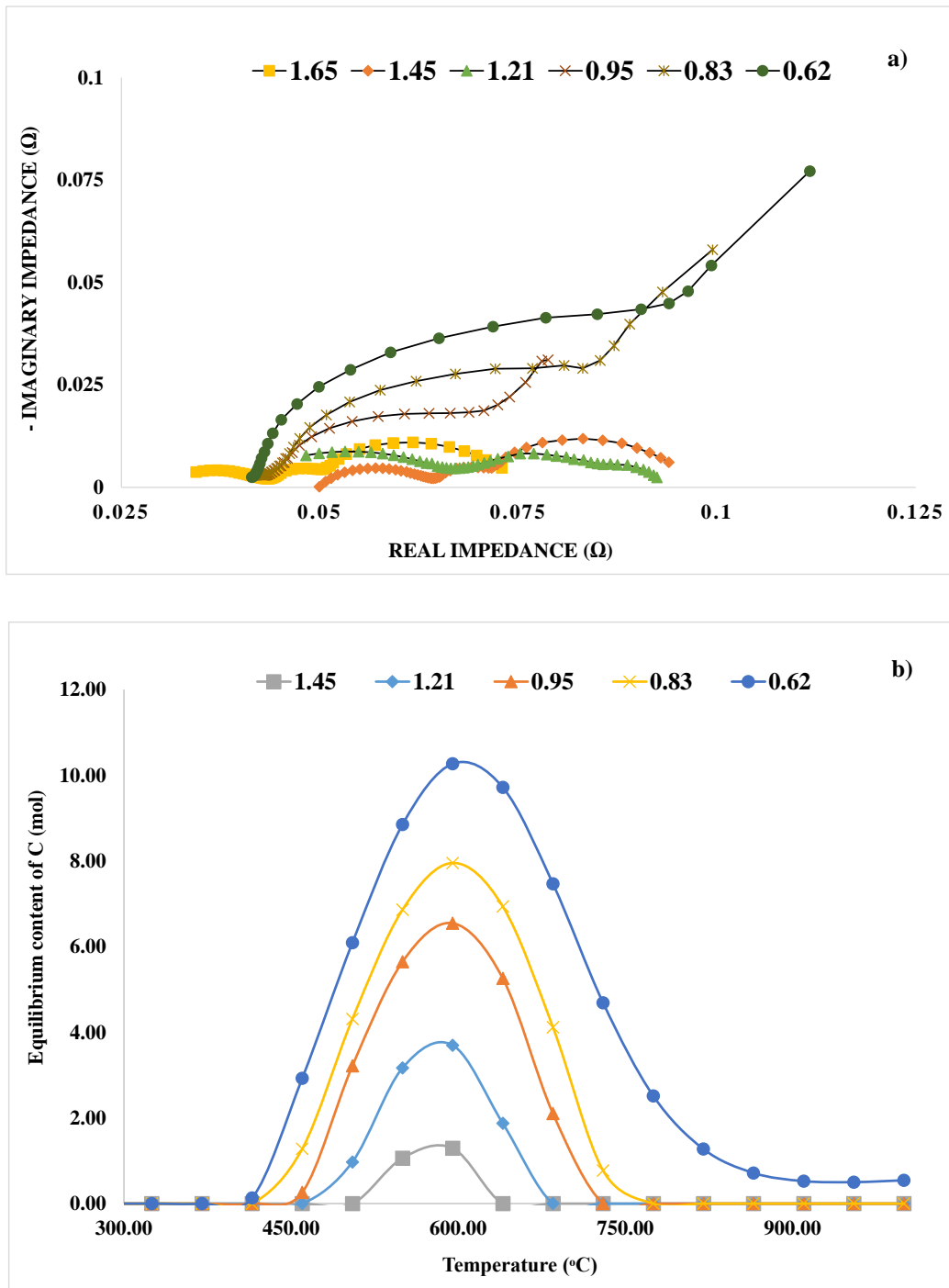


**Fig. 5.7 (a)** Impedance spectra of the SOFC stack at 750 °C exposed to reformat blend at 0.4 A  $\text{cm}^{-2}$  with varying S/C ratios fuel flow - 5 L  $\text{min}^{-1}$ , air flow - 10 L  $\text{min}^{-1}$ ,  $X_f = 0.5$ . **(b)** Equilibrium carbon formation diagram with the base fuel used for varying S/C ratios with respect to operating temperature.

The impedance spectra for the tested S/C ratios are shown in Fig. 5.7a. It clearly showed the trend of overall increase in the ohmic as well as the polarization resistance as the data was observed from S/C value of 1.65 to 0.62. It was evident from the changing nature of the impedance diagrams, interaction of carbon/coke with the anodic catalyst in the fuel feed. The first three spectra observed for S/C values 1.65, 1.45 and 1.21 were much similar like previous spectra obtained with S/C values of 2. It comprised of three time constants and the three arcs were fitted with the circuit model in Fig. 5.3b. Even though there were changes in the electrochemical parameters, the nature and variation in the three spectra suggested that there were not much major changes in the cell characteristics and behavior. For the data obtained from S/C values of 0.95, 0.83 and 0.62, the behavior was significantly different as observed. The number of arcs reduced to one governing the high frequency region and there was a visible straight line at an angle of  $45^\circ$  in the low-mid frequency region. The high frequency first arc was attributed to the conventional fuel oxidation reactions and charge transfer process. The low frequency part of the spectra seemed to match well and fit the characteristics governed by a Warburg element [13]. Warburg element has been reported extensively by researchers [5-10, 13] for understanding diffusion related behavior in porous medium. Such response is well-described by a linearized diffusion model in a semi-infinite planar domain. The rate of an electrochemical reaction can be strongly influenced by diffusion of a reactance towards or a product away from the electrode surface. This is often the case when a solution species must diffuse through a film on the electrode surface. This situation can exist when the electrode is covered with reaction products, adsorbed solution components, or a prepared coating. For diffusion-controlled electrochemical reaction, the current is 45 degrees out of phase with the imposed potential. In terms of simple equivalent circuits, the behavior of Warburg impedance (a 45 degree phase shift) is midway between that of a resistor (0 degree phase shift) and a capacitor (90 degree phase shift). Fig. 5.3c was adopted as the model for fitting the impedance data. The best fit electrochemical parameters are shown in Table 5.5.

**Table 5.5** Electrochemical parameters obtained from the CNLS fitting for Reformate blend with varying S/C values.

	<b>S/C = 1.65</b>	<b>S/C = 1.45</b>	<b>S/C = 1.21</b>	<b>S/C = 0.95</b>	<b>S/C = 0.83</b>	<b>S/C = 0.62</b>
<b><math>R_{1S/C}</math></b>	0.0278	0.0340	0.0390	0.0425	0.0427	0.0408
<b><math>R_{2S/C}</math></b>	0.0193	0.0098	0.0348	0.0500	0.0760	0.1012
<b><math>R_{3S/C}</math></b>	0.0093	0.0067	0.0187	-	-	-
<b><math>R_{4S/C}</math></b>	0.0240	0.0178	0.0132	-	-	-
<b>W-R</b>	-	-	-	0.1172	0.1766	0.2637
<b>W-T</b>	-	-	-	21.970	33.010	48.04
<b>W-P</b>	-	-	-	0.5817	0.5889	0.5840

The increase in the ohmic resistance ( $R_{1S/C}$ ) was observed from 0.0278  $\Omega$  to 0.0408  $\Omega$  within the first three S/C values as the amount of steam was reduced with an increase of  $\sim 46.7$  %. The interesting aspect in the above trend was that, it increased around 40 % within the first three S/C values and the remaining change comparatively lesser. When the S/C value was reduced from 1.65 to 1.45, there was a 22 % increase in the ohmic impedance which was almost half of the entire increase in  $R_{1S/C}$ . Even though there was maximum increase in the initial S/C ratios, the ohmic resistance stabilized and did not show any further change. In fact at the lowest S/C ratio, it reduced from the previous value by  $\sim 4.5$  %. This confirmed that the ohmic resistance increase was not alarming and it cannot be directly associated with decreasing S/C ratios. The ambiguous effect can

also initiate from natural aging due to continuous running of the stack for longer durations and possible interconnect degradation through chromium migration [9-12].

The trends observed in  $R_{2S/C}$ ,  $R_{3S/C}$  and  $R_{4S/C}$  were clear and meaningful. When the S/C value was reduced from 1.65 to 1.45, the fuel partial pressure increased which resulted in an increased electrochemical charge transfer process resulting in a reduction of  $R_{2S/C}$  by around 50 %. Therefore, the amount of diffusion resistance of  $H_2/H_2O$  ( $R_{3S/C}$ ) and  $CO/CO_2$  ( $R_{4S/C}$ ) also gets reduced by 28 % and 26 % due to reduced water content and shift reactions respectively. It can also be said that the performance actually improved by a reasonable margin when the S/C was reduced to 1.45. But as soon as the S/C ratio was reduced further down to 1.21, the actual carbon interaction with the anode catalyst began to take prominent effect. There was considerable and noticeable increase in  $R_{2S/C}$  (~ 255 %),  $R_{3S/C}$  (~ 179 %) from S/C of 1.45 to 1.21. The decrease of  $R_{4S/C}$  (~ 26 %) though was consistent as it pointed towards even reduced chances of occurrence of shift reaction because of lesser water content in the feed. During the lowest three S/C values of 0.95, 0.83 and 0.62, the nature of arcs completely changed as explained before. The charge transfer resistance arc was associated to similar high frequency regions like the rest and as expected it increased by around 190 % from S/C values of 1.21 to 0.62. But as stated before, in the low-mid frequency region, Warburg behavior was noticed for the lowest S/C ratios.  $W-R$  is the value or  $Z'$ (real part of impedance) at very low frequency,  $W-T$  is the diffusion interpretation of Warburg element (time constant) and it is given as  $W-T=L^2/D$  where  $L$  is effective diffusion thickness and  $D$  is diffusion coefficient of particle. As observed from the increasing  $W-R$  and  $T$  values, there was consistent increase in the diffusion resistance with reduction of S/C values along with an increase in the time constant values. Also, the overall impedance in the cell increased at a faster rate when the S/C moved into the range of 0.95 to 0.62. The repeatable Warburg response with decreasing steam pointed towards a deposited or adsorbed film on the electrode surface as mentioned before.

An equilibrium diagram indicating the regions of carbon formation for the baseline fuel with changing temperature is given in Fig. 5.7b. The degradation by carbon with respect to S/C ratios can be interpreted with two main theories or mechanisms as also explained in literature speculated to occur in two stages here. The most important phenomenon which can lead to the interaction especially at lesser S/C values seen in our case, is the metal dusting effect which is analogous to dry pitting in corrosion systems [31, 32]. Under this effect, production of filamentous carbon near Ni surface occurs at a rapid rate than its subsequent removal by steam. Even though thermochemical results state a non-stable carbon region at equilibrium at higher S/C ratios, under a certain limited steam content range, graphitic carbon can form depending on the reactor size, electrode area and the residence time. This process seemed to kick off in the S/C range 1.45 to 1.21 in our work, when appreciable percentage increase in cell parameters were observed. In this phenomenon, initially the carbon forms randomly oriented base planes on Ni lattice planes followed by its growth into the metal. This results in a diffusion gradient between the gas and metal interface which leads to a driving force for graphite penetration into the Ni porous structure. Finally, the Ni-YSZ cermet valuable for triple phase fuel oxidation reactions is disrupted forming sintered Ni powders resulting in lesser contact and conductivity. From Fig. 5.7b, it can be seen that at higher S/C ratios (1.45 and 1.21), the carbon formation region shifted to a narrower temperature range of 450 – 700 °C. Therefore, there can also be a possibility of carbon formation in the bulk stream near the feed inlet on the outer edges of the experimental setup because of a much reduced temperature than the inside of the furnace. Very fine carbon particles which are formed can get entrained and carried away with the bulk stream inside the furnace interior to the SOFC stack. The sudden increase in  $R_{2S/C}$  values in the above mentioned S/C range seemed to correlate well with the above effects. Below S/C values of 1.21, the above effect was dominated by the second mechanism of deposited carbon on the anode surface produced by pyrolysis, disproportionation and reduction of CO and CH<sub>4</sub> present in the bulk stream. With reduced H<sub>2</sub>O in the bulk fuel stream,

higher amounts of CO and H<sub>2</sub> seemed to have the ideal conditions to undergo chemical methanation producing elemental carbon. The above processes as indicated by the Warburg behavior seemed to cause a diffusion gradient in the porous anode. With decreasing S/C ratios (0.95 – 0.62), the time constant (W-T) also increased by 118 % signifying higher amount of diffusion pathways in the system. Each of the S/C ratios were kept for an hour in this test before measuring to reach steady state, thus conclusive evidence of time governed equilibration or additional degradation was beyond the scope of this study.

### *3.5 Impact of Fuel Utilization*

Fuel utilization (FU) is a critical factor for analysis of cell performance and optimum fuel flow-rate and S/C ratio [9-12, 20, 21]. Fuel utilization can be adjusted by tuning anode gas flow rate or S/C ratio. In this study, S/C ratios were not changed to avoid the effect of fuel dilution and subsequently to observe the effects from fuel utilization only.

Impedance plots were acquired at various operating utilizations with fuel combination for  $X_f = 0.5$  at  $0.4 \text{ A cm}^{-2}$  from Table 5.2. S/C ratio was kept at 2. The plots were modelled by the circuit diagram in Fig. 5.3b and the corresponding area specific resistances were plotted with respect to fuel utilization percentage in Fig. 5.8. It was clearly seen that  $R_{2FU}$  which was associated to charge transfer resistance showed very minimal increase. But the arcs  $R_{3FU}$  and  $R_{4FU}$  increased with increase in fuel utilization values above 70 %. While  $R_{3FU}$  showed an increase of ~ 43 %,  $R_{4FU}$  showed appreciable increase of ~ 109 % when fuel utilization was tested from 70 % to 90 %. This indicated an increase in the resistance associated to bulk diffusion due to an increase in the amount of H<sub>2</sub>O and CO<sub>2</sub> in the fuel stream resulting from an increased conversion of H<sub>2</sub> and CO in the fuel mixture. Fuel starvation can also occur at extremely high fuel utilization of around 90 % as reported by Stolten et al. [20]. At very high fuel conversion rates, the nominal oxygen partial pressure can be very close to the Ni oxidation potential, which can lead to re-oxidation of the anode

catalyst. The above effect may permanently harm the anode microstructure which can also represent itself in an increase of the charge transfer resistance. Even though our work did not involve fuel utilization more than 90 % (for protecting the stack), careful observation confirmed a slow increase of  $R_{2FU}$  at around 85% after being almost constant for all the previous data points.

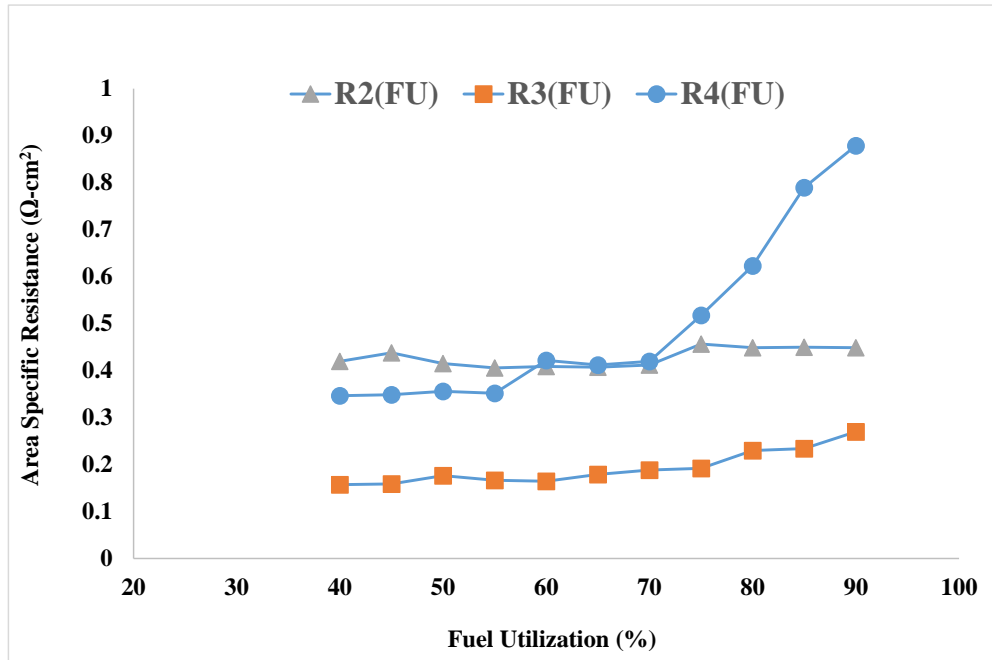


**Fig. 5.8** Area specific resistances with respect to fuel utilization % for SOFC stack at 750 °C exposed to reformat blend at  $0.4 \text{ A cm}^{-2}$  with S/C ratio = 2, air flow -  $10 \text{ L min}^{-1}$ ,  $X_f = 0.5$ .

It is a well-known fact that efficiency of SOFC systems is directly proportional to the fuel utilization but as mentioned before, as high utilizations were reached the power density also gets reduced due to increase of corresponding area specific resistances. Hence for a system of definite cell size and geometry, the fuel utilization has to be a trade-off and optimum choice should be made considering technico-economic factors. In this case it was seen that 65 % - 70 % fuel utilization was the ideal range for smooth stack operation without compromising on both the efficiency and the power output of the system. An efficiency of 52 % - 55 % was calculated in this utilization range under the above mentioned operating conditions which was an acceptable figure

as compared to other related systems in literature [22]. The efficiency of a SOFC system directly impacts the overall cost and therefore a judicious choice is necessary to maximize the return of investment especially in commercial systems without involving unwarranted cell damage.

### *3.6 Long Term Operation with Optimized Conditions*

After determination of the optimum operating conditions, long term durability and performance test was carried out as a State of Health analysis. Eight different operating conditions were considered and tested based on suitable judgement of the results obtained before. Also, testing with all possible sets of data points gave us an idea of the sensitivity of the stack behavior and its comparison with each other. The three different parameters with their six optimally selected values were  $X_f$  (0.41 and 0.5), S/C (1.45 and 2) and FU (65 % and 75 %) and all the eight possible combinations of set of operating conditions determined are shown in Table 5.6. Each of the conditions were run for an overall time period of 500 h and the air to fuel ratio on the cathode side was always kept constant at 2.5 with 40 % oxygen utilization. The temperature and current density were kept constant at 750 °C and 0.4 A cm<sup>-2</sup> respectively. In between each tests, the fuel was switched to humidified H<sub>2</sub> and run for one hour. During the tests, there were a couple of interruptions due to sudden power outages and blockages in fuel stream represented in the form of a voltage spike. But the stoppages were for a very short duration of time for which it didn't seem to affect the stack in a negative way. The compositions tested were selected judiciously keeping in mind that the H<sub>2</sub>/CO ratio was optimized according to a practical setting as if a real reforming system was used before the stack setup to provide the reformat blend. Therefore a fuel blend highly rich only in H<sub>2</sub> was not considered because that would make the assumption of a simulated reformat void and ambiguous. It is also useful to mention that due to each of the tests being carried out in the same or a different stack (of same physical and material characteristics) at various

timings, relative performance was of primary importance originating from the starting point of the individual tests.

**Table 5.6** Optimized operating conditions selected for long term stack performance tests.

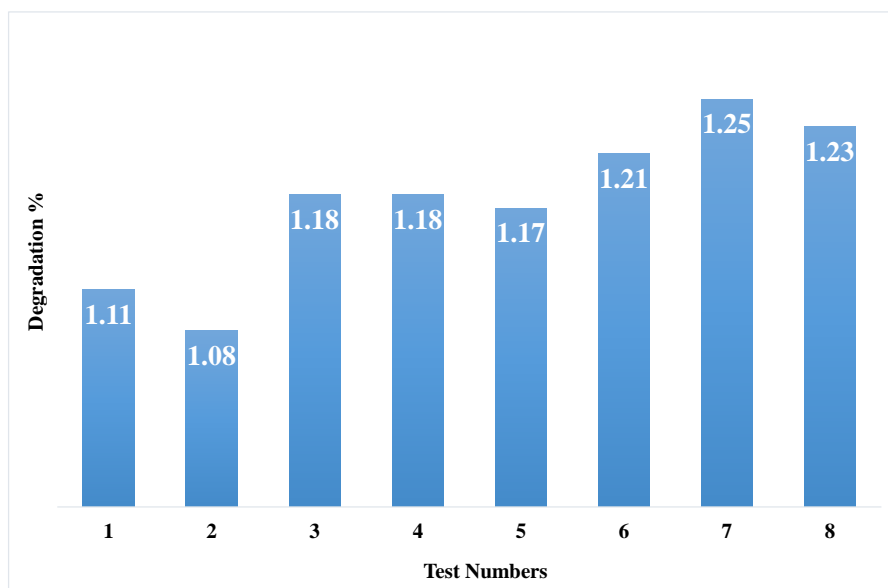
	<b>Test #1</b>	<b>Test #2</b>	<b>Test #3</b>	<b>Test #4</b>	<b>Test #5</b>	<b>Test #6</b>	<b>Test #7</b>	<b>Test #8</b>
<b><math>X_f</math></b>	0.41	0.41	0.41	0.41	0.5	0.5	0.5	0.5
<b>S/C</b>	1.45	1.45	2	2	1.45	1.45	2	2
<b>FU (%)</b>	65	75	65	75	65	75	65	75

From Fig. 5.9a, it was observed that the degradation range varied from 1.08 % to 1.25 % per 500 h. The condition for test #2 gave the lowest degradation rate and test #7 showed the highest degradation rate. The degradation numbers observed here were quite similar to values obtained by other researchers on similar stack designs. Sprenkle et al. [12] observed degradation of 1.12 % per 500 hour with similar stack characteristics. Even though, it is well known that degradation actually levels off after the initial 1000 h [11-12, 16], it was important to know and understand the stack behavior under various fuel operating conditions to get an idea of the sensitivity and variation. It was clear that the factor  $X_f$  was most sensitive because all the conditions with a lower  $X_f$  number showed lesser degradation rate consistently. Only test#5 with a higher  $X_f$ , showed a degradation rate lower than test#3 and test #4. This also indicated that a slightly lower S/C ratio (within non-carbon deposition regime) can be used to balance the performance reduction induced by less  $H_2$  partial pressure. Also the trend shown by test #1,2 and #7,8 clearly showed that a higher fuel

utilization led to a lesser degradation rate in both the cases with other two conditions same. Therefore, it can be said that considering the relative difference in degradation rate between high/low SC ratio and high/low fuel utilization, S/C ratio was more sensitive than Fuel Utilization in our case.

A trend in the individual area specific resistances obtained are shown in Fig. 5.9b. They were represented in the form of percentage change between initial and final data acquisition point to account for the relative comparison. Due to the stack being run for only 500 h for each case, ohmic resistance change was minimal and was neglected which also allowed us to focus on any interaction of the conditions with the cell itself. It was found that all the impedance curves for all the conditions can be modelled with the circuit shown in Fig. 5.4b thus confirming no interaction of carbon with the anode catalyst. Also, the charge transfer resistance  $R_{2SOH}$  showed very less increase showing that there was minimal harm caused to the anode. The primary contribution towards stack resistance was attributed to the arc  $R_{4SOH}$  which increased in a range of 34 % - 47 % through the entire duration of test for all conditions.

a)



b)

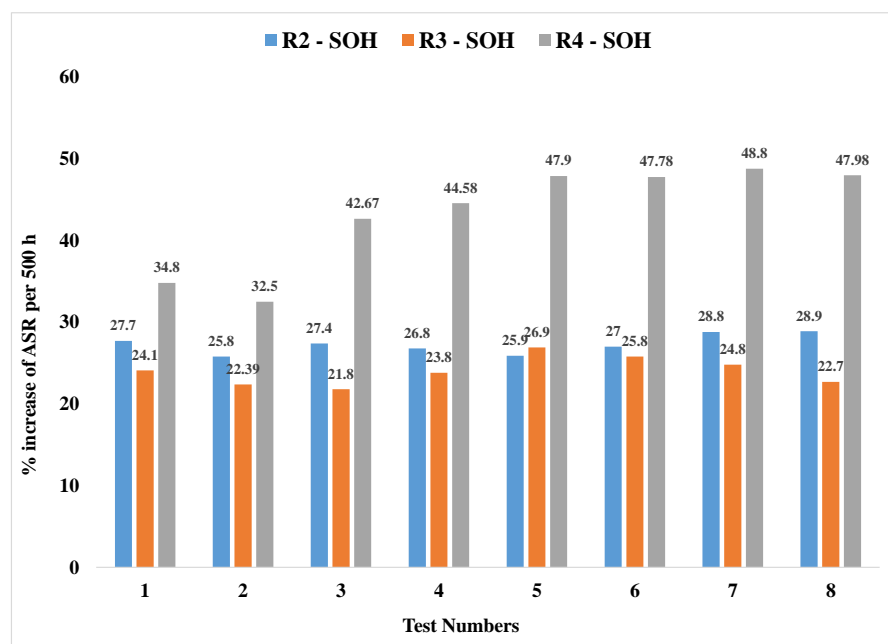


**Fig. 5.9 (a)** Degradation rates in % per 500 h of the SOFC stack at 750 °C for eight optimized operating conditions consisting of three variables:  $X_f$ , S/C and FU %. **(b)** Percentage increase in area specific resistances per 500 h for the SOFC stack at 750 °C with eight optimized operating conditions (R2<sub>SOH</sub> [left], R3<sub>SOH</sub> [middle], R4<sub>SOH</sub> [right]).

Therefore the main causes of degradation can be related to diffusion related processes which can arise from flow inconsistencies or inhomogeneous gas distribution due to heavier content in the bulk fuel. Chances of minor carbon deposition on top of the anode surface creating a diffusion flux between the triple phase sites and the bulk fuel can also be considered thus increasing the diffusion resistance in the cell. In spite of that, under the tested conditions there was no significant signs of accumulated carbon deposition due to constant oxygen flux and suitable steam content. This was confirmed by post mortem analysis of the stacks after disassembling them. Also previously we have seen finger print impedance behavior of the onset of carbon-anode interaction in Fig. 5.7, which was also not observed in this case for all the 8 tests of 500 h each.

#### **4. Conclusions**

An approach for performance characterization of sub-commercial scale SOFC stacks running on alternative syngas fuel have been discussed and highlighted by impedance spectroscopy. EIS helped to analyze and optimize the suitable fuel characteristics required for steady state operation of the stack within an acceptable range. Signature EIS spectra were obtained for both the fuel blends which helped to differentiate between them and their underlying governing processes. A comparison of the equivalent circuit parameters helped to quantify the resistances and determine the changes in cell characteristics with operating fuel conditions. The reformat fuel was seen to be diffusion controlled with an additional process associated to CO/CO<sub>2</sub> diffusion and shift reaction. The fuel characteristics tested were CO/H<sub>2</sub> volumetric ratio, S/C ratio and fuel utilization %. It was observed that the performance of the hydrogen blend and the reformat blend approached each other in performance at higher current regimes of around 0.5 A cm<sup>-2</sup>. This directly pointed towards CO involvement in electro-oxidation and also possible conversion of CO to H<sub>2</sub> via shift reaction. EIS was applied to identify the individual processes and understand their dependability on fuel composition. Various S/C ratios were tested to determine the limit of operation of the stack

without inflicting significant carbon damage on the anode. EIS plots from S/C ratio 1.65-1.45 did not indicate any noticeable carbon interaction and the performance were quite comparable. At lower S/C ratios though, the nature of impedance spectra changed showing a Warburg behavior at low frequencies indicating diffusion related to a film formation on the anode which was possibly a form of carbon deposited on the Ni. Also in a narrow range of around 1.45-1.21, there was noticeable increase in the charge transfer resistance without Warburg behavior indicating interaction of the porous anode structure with filamentous carbon produced possibly from disproportionation of CO. The effect of fuel utilization % on stack resistances was also analyzed and it was found that the primary effect was on the low frequency resistance. Utilization within around 70 % showed minimal change in the resistances. Finally, a long term performance and sensitivity test with the three optimized fuel characteristics was carried out for eight different conditions for a period of 500 h. The degradation rate for  $X_f = 0.41$ ,  $S/C = 1.45$  and  $FU = 75\%$  seemed to be the lowest and the values for all tests ranged from 1.08 % - 1.25 %. The degradation rate were quite comparable to values reported for hydrogen/nitrogen blend in literature [11,12] with a similar stack design thus validating our approach to converge on specific fuel operating conditions for suitable system operation, especially in carbonaceous fuel mixtures.

This work based its study on three primary fuel characteristics considering a simulated reformat from a hypothetical reformer unit. Even though direct reforming SOFC have been a topic of intense research, efficiency of commercial fuel cell systems have been found to be higher for pre-reformed fuel. But it is also important to optimize the economics of reformer units with optimum conversion of fuel to  $H_2$  and CO. EIS can effectively contribute in this effort. Future sensitivity studies with EIS applied on physical operating conditions such as current cycling, thermal cycling, redox cycling and pressure can help to optimize system performance even further.

Statistical sensitivity analysis based on key operating conditions may also help to complement electrochemical performance measurement efforts.

## References – Chapter 5

- [1] J. Larminie, A. Dicks, Fuel Cell Systems Explained, 2nd ed, Wiley, 2003.
- [2] A. Stambouli, E. Traversa, Renewable and Sustainable Energy Reviews 6 (2002) 433-455.
- [3] Thomas A. Adams, Jake Nease, David Tucker, Paul I. Barton, Industrial & Engineering Chemistry Research 2013, 52, 3089-3111.
- [4] Xiao-Ming Ge, Siew-Hwa Chen, Qing-Lin Liu, Qiang Sun, Advanced Energy Materials 2012 (20) 1156-1181.
- [5] Sanchit Khurana, Mark LaBarbera, Mark V. Fedkin, Serguei N. Lvov, Harry Abernathy, Kirk Gerdes, J. Power Sources 274 (2015) 1049-1054.
- [6] M.S. LaBarbera, M.V. Fedkin, J.K. Lee, Z. Zhou, S.N. Lvov, ECS Transactions 25 (2) 1125-1132 (2009).
- [7] M. LaBarbera, M. Fedkin, S.N. Lvov, ECS Transactions 35 (1) 2725-2734 (2011).
- [8] M. LaBarbera, M.Fedkin, X. Wang, X. Chao, C. Song, S. Lvov, ECS Transactions 35 (1) 2867-2872 (2011).
- [9] K. Huang, J.B. Goodenough, “Solid Oxide Fuel Cell Technology: Principles, Performance and Operations”, 1<sup>st</sup> edition, 2009
- [10] S.C. Singhal, K. Kendal, “High Temperature and Solid Oxide Fuel Cells”, 1<sup>st</sup> edition, 2003
- [11] P. Lamp, J. Tachtler, O. Finkenwirth, S. Mukherjee, S. Shaffer, Fuel Cells 2003, 3, No. 3
- [12] Subhasish Mukherjee, Karl Haltiner, Rick Kerr, Jin Yong Kim, Vince Sprenkle, ECS Transactions 35 (1) 139-146 (2011)
- [13] J.R. Macdonald, Impedance Spectroscopy Emphasizing Solid Materials and Systems, New York, NY: John Wiley and Sons, 1987.

- [15] M. Lang, C. Auer, A. Eismann, G. Schiller, P. Szabo, ECS Trans. 7 (1) 85-94 (2007)
- [16] S. Giles, G. Lin, A. Mohanram, Y. Narendar, J. Pietras, F.C. Qi, Wesley R., R. Robbins, and R.J. Sliwoski
- [17] R.R. Mosbæk, J. Hjelm, R. Barfod, J. Høgh, P.V. Hendriksen B1006, 10<sup>th</sup> European SOFC Forum, 2012.
- [18] S. McIntosh, R.J. Gorte, Chem. Rev. 2004, 104, 4845-4865.
- [19] G. Almutairi, A. Dhir, W. Bujalski, Fuel Cells 14, 2014, No. 2, 231-238
- [20] A.M. Sukeshini, B. Habibzadeh, B.P. Becker, C.A. Stoltz, B.W. Eichhorn, G.S. Jackson, J. Electrochem. Soc., 153 (4) A705-A715 (2006)
- [21] Q. Fang, L. Blum, R. Peters, M. Peksen, P. Batfalsky, D. Stolten, Int. J. Hydrog. Energ. 40 (2015) 1128-1136
- [22] D. Papurello, R. Borchellini, P. Bareschino, V. Chiodo, S. Freni, A. Lanzini, F. Pepe, G.A. Ortigoza, M. Santarelli, Applied Energy 125 (2014) 254-263
- [23] V.M. Janardhanan, V. Heuveline, O. Deutschmann, J. Power Sources 172 (2007) 296-307
- [24] J.S. O'Brien, "Cermets anodes for solid oxide fuel cells (SOFC) systems operating in multiple fuel environments: effects of sulfur and carbon composition as well as microstructure", PhD Dissertation, Ottawa, Canada, 2012
- [25] D. Pechini, G. Cinti, G. Discepoli, E. Sisani, U. Disederi, Int. J. Hydrog. Energy 38 (2013) 525-531
- [26] O. Razbani, M. Assadi, Int. J. Hydrog. Energy 38 (2013) 13781-13791
- [27] A. Kromp, A. Webser, E. Ivers-Tiffée, ECS Transac. 57 (1) 3063-3075 (2013)
- [28] T.S. Lee, J.N. Chung, Y. Chen, Energy Conv. and Management 52 (2011) 3214-3226

- [29] A. Weber, B. Sauer, A. Müller, D. Herbstritt, E. Ivers-Tiffée, *Solid State Ionics* 152-153 (2002) 543-550
- [30] W. Yao, E. Croiset, *ECS Transac.* 53 (30) 163-172 (2013)
- [31] J. Hanna, W.Y. Lee, A.F. Ghoniem, *J. Electrochem. Soc.* 160 (6) F698-F708 (2013)
- [32] T. Chen, W.G. Wang, H. Miao, T. Li, C. Xu, *J. Power Sources* 196 (2011) 2461-2468
- [33] S. K. Schubert, M. Kusnezoff, *ECS Transac.* 25 (2) 2073-2082 (2009)
- [34] C. Willich, A. Tomaszewski, M. Henke, J. Kallo, K.A. Friedrich, *ECS Transac.* 57 (1) 401-409 (2013)

## Chapter 6

---

### Summary of the Research

This dissertation investigates, presents and details the author's contribution towards the analysis, performance characterization and kinetics studies of an anode supported solid oxide fuel cell of similar material composition but different cell geometry and system design, with the help of sophisticated linear and non-linear electrochemical techniques. The primary linear electrochemical technique used was EIS which provided valuable insights into specific reaction mechanisms in presence of foreign undesired substances and was also used to diagnose the state of health of a stack to understand failure modes impeding long term durability of SOFCs. A non-linear technique, EFM was applied for the first time on SOFCs and its subsequent merits and utility was discussed and introduced to the SOFC research community. A brief chapter wise summary is provide below:

- Chapter 1 introduces the basic principles of a SOFC along with the fundamentals of the basic electron and ion transfer processes at the respective SOFC electrodes. The importance of SOFC in the scientific community is stated and the motivation of the dissertation is briefly outlined.
- Chapter 2 explains the experimental and analytical considerations important in the electrochemical characterization of the various process conditions and corresponding fuel cell behavior. A detailed description and pictures of the fuel cell setups (miniature cell and commercial scale) is also included in this chapter. Discussions regarding the main electrochemical characterization techniques (AC/DC/linear/non-linear) was provided in this chapter.
- Chapter 3 investigates the degradation effects of inorganic impurities (sulfur, siloxane, chlorine and ammonia) on SOFC button cell performance present in alternative syngas fuels and reformates from carbonaceous fuels. Linear AC and DC electrochemical

techniques are applied as *in-situ* monitoring methods for generating signature identification of cell response under various concentrations of different inorganic species. A subtraction EIS approach was adopted to associate the change of cell impedance exclusively to the effect of the foreign impurities. Finally concentration limits and corresponding effects of each of them are also determined by quantitative treatment.

- Chapter 4 explores a new, introductory non-linear electrochemical technique, EFM being applied for the first time on an SOFC system for determination of important kinetic parameters, exchange current density and transfer coefficients without restrictions unlike other conventional electrochemical methods. A specific electrochemical model was developed and the resulting EFM relations were derived. The results obtained from the technique are compared with other already established methods and validated. Also, inherent advantages associated with this technique over others are also explained and discussed.
- Chapter 5 presents the application of linear electrochemical characterization to understand the effects of three critical fuel composition parameters ( $\text{CO}/\text{H}_2$  volumetric ratio, Steam-to-Carbon ratio and Fuel Utilization %) on the performance of a SOFC sub-commercial stack. The fuel used in this case was an alternative syngas blend (simulated) to mimic a hypothetical pre-reformer system conditions attached to a SOFC setup. Finally the most optimum conditions for each of the parameters are zeroed in and long term state of health tests are carried out for eight possible combinations to check their individual degradation rate in 500 h.

### General Conclusions and Future Directions

This dissertation provides a basis for the performance and kinetic analysis of anode supported solid oxide fuel cell systems to run on alternative syngas fuels in presence of inorganic impurities and critical fuel characteristics. The subtraction impedance analysis approach adopted to study the effects of impurities on the cell has been shown to be very effective in associating the change in cell behavior directly to the related physical degradation arising from a specific foreign substance. In this way, finger-print impedance spectra can be developed which can help in better identification of the amount and nature of performance reduction caused by a particular contaminant. Sulfur was recognized by a Gerischer element signifying an adsorption followed by a chemical reaction. Siloxane showed characteristic open Warburg element behavior implying a change in porosity of the anode caused by a deposition of oxide in the structure. Chlorine and Ammonia had a much reduced effect on the cell performance with no specific behavior related to a specialized circuit element. Their response was similar to a non-poisoned cell indicating non surface interaction processes unlike the previous two. Quantification of individual impedance contributions for all cases can allow for the fine tuning of anode material properties by alloying or doping the Ni/YSZ anode to better function in the presence of the above mentioned substances.

A non-linear technique, EFM in these studies demonstrated favorable results and justified our novel research at exploring this sophisticated tool for the first time in SOFCs. Determination of exchange current density and transfer coefficients have always been cumbersome and also very important. Large scale systems and their performance can be tracked *in-situ* in a much better, faster way by EFM which also can be a measure to evaluate instantaneous and relative performance or indicate the degradation rate of a SOFC system. We have shown that EFM has the capability to

serve as a complementary technique in addition to conventional methods used in academia and industry. It overcomes some of the difficulties associated with EIS and LSV in terms of time of operation, data treatment and physical change in electrode surface properties. A similar approach can be devised for other SOFC systems based on their distinct operating and experimental conditions.

Finally, a State of Health analysis of a SOFC sub-commercial stack revealed that the effect of the factors on system performance in terms of sensitivity followed this order:  $\text{CO}/\text{H}_2 > \text{S}/\text{C Ratio} > \text{FU}$ . Systematic variation of the three fuel characteristics and understanding stack behavior by EIS allowed us to analyze the various electrochemical reactions and processes occurring in specific range of values of the above factors and helped us to zero in on the 8 most optimized conditions. Tests were conducted for a total of 4000 h to compare the relative differences in the 8 optimized conditions and evaluate them in order of their performance. It was found that for this system,  $[\text{CO}/(\text{CO}+\text{H}_2)]$  ratio of 0.41 , S/C ratio of 1.45 and FU of 75 % had the best performance amongst the 8 runs. The stacks were in power generation mode thus increasing the value of this work. Very limited work has been carried out yet in SOFC academic community with larger systems in power generation mode due to restrictions in high current handling capabilities. Therefore, our work emphasizes, elucidates this approach and its effectiveness in better diagnostic monitoring of SOFC commercial systems.

The future work as a possible extension of the research carried out here should be directed on,

1. Subtraction impedance analysis and development of signature impedance plots of SOFC button cells and stacks with a combination of various impurities at different concentrations.
2. Application of EFM on more complex SOFC systems involving fuel with multiple species can be specifically studied on a case-by-case basis with proper electrochemical model considerations under different operating conditions.

3. Future sensitivity studies with EIS applied on physical operating conditions such as current cycling, thermal cycling, redox cycling and pressure can help to optimize system performance even further. Statistical sensitivity analysis based on key operating conditions may also help to complement electrochemical performance measurement efforts.

## Appendix

As discussed before in Chapter 4, the cathodic Tafel coefficient ( $\beta_c$ ) becomes infinite under diffusion-controlled reverse reaction in the conditions mentioned. The kinetic equation thus reduces to,

$$i = [\exp (\eta / \beta_a) - 1] / [1 / i_{0, \text{eff}} - 1 / i_{\text{lim}}] \quad (1)$$

An input distortion signal ( $\eta = U_0 \sin \omega_1 t + U_0 \sin \omega_2 t$ ) according to the EFM technique is applied to the fuel cell system in the form of sine waves with two different frequencies. Therefore substituting the input signal into equation (1) gives,

$$i = i_{0, \text{eff}} [\exp (U_0 \sin \omega_1 t / \beta_a) \exp (U_0 \sin \omega_2 t / \beta_a) - 1] \quad (2)$$

where  $i_{0, \text{ex}} = 1 / [1 / i_{0, \text{eff}} - 1 / i_{\text{lim}}]$  (Used for ease of derivation)

The exponential terms above can be expanded to third order using Taylor series expansion as,

$$e^x = 1 + (x/1!) + (x^2/2!) + (x^3/3!) + \dots, -\infty < x < \infty \quad (3)$$

Therefore the exponential terms after the expansion in the current-potential equation becomes,

$$\begin{aligned} \exp (U_0 \sin \omega_1 t / \beta_a) &= 1 + (U_0 \sin \omega_1 t / \beta_a) + 1/2 (U_0 \sin \omega_1 t / \beta_a)^2 \\ &+ 1/6 (U_0 \sin \omega_1 t / \beta_a)^3 + \dots \end{aligned} \quad (4)$$

$$\begin{aligned} \exp (U_0 \sin \omega_2 t / \beta_a) &= 1 + (U_0 \sin \omega_2 t / \beta_a) + 1/2 (U_0 \sin \omega_2 t / \beta_a)^2 \\ &+ 1/6 (U_0 \sin \omega_2 t / \beta_a)^3 + \dots \end{aligned} \quad (5)$$

Therefore the equation (2) can be represented as [after neglecting the higher order terms ( $>3$ ) in the Taylor series expansion]

$$i = i_{0,\text{ex}} \{ [1 + (U_0 \sin \omega_1 t / \beta_a) + 1/2 (U_0 \sin \omega_1 t / \beta_a)^2 + 1/6 (U_0 \sin \omega_1 t / \beta_a)^3] [1 + (U_0 \sin \omega_2 t / \beta_a) + 1/2 (U_0 \sin \omega_2 t / \beta_a)^2 + 1/6 (U_0 \sin \omega_2 t / \beta_a)^3] - 1 \} \quad (6)$$

$$i = i_{0,\text{ex}} \{ [1 + U_0 / \beta_a \sin \omega_1 t + 1/2 (U_0 / \beta_a)^2 \sin^2 \omega_1 t + 1/6 (U_0 / \beta_a)^3 \sin^3 \omega_1 t + U_0 / \beta_a \sin \omega_2 t + 1/2 (U_0 / \beta_a)^2 \sin^2 \omega_2 t + 1/6 (U_0 / \beta_a)^3 \sin^3 \omega_2 t + (U_0 / \beta_a)^2 \sin \omega_1 t \sin \omega_2 t + 1/2 (U_0 / \beta_a)^3 \sin^2 \omega_1 t \sin \omega_2 t + 1/2 (U_0 / \beta_a)^3 \sin \omega_1 t \sin^2 \omega_2 t] - 1 \} \quad (7)$$

The above equation was solved further for the higher order (2<sup>nd</sup> and 3<sup>rd</sup>) by applying the power reducing/half angle trigonometric equation as following,

$$\sin^2 x = [1 - \cos(2x)]/2 \quad (8)$$

$$\sin^3 x = 3/4 \sin x - 1/4 \sin 3x \quad (9)$$

$$\sin x \sin y = 1/2 [\cos(y-x) - \cos(x+y)] \quad (10)$$

$$\cos x \sin y = 1/2 [\sin(y-x) + \sin(x+y)] \quad (11)$$

Applying the above relations (8-11) on equation (7), it reduces to,

$$i = i_{0,\text{ex}} \{ [1 + U_0 / \beta_a \sin \omega_1 t + U_0 / \beta_a \sin \omega_2 t + 1/4 (U_0 / \beta_a)^2 - 1/4 (U_0 / \beta_a)^2 \cos 2\omega_1 t + 1/4 (U_0 / \beta_a)^2 - 1/4 (U_0 / \beta_a)^2 \cos 2\omega_2 t + 1/8 (U_0 / \beta_a)^3 \sin \omega_1 t - 1/24 (U_0 / \beta_a)^3 \sin 3\omega_1 t + 1/8 (U_0 / \beta_a)^3 \sin \omega_2 t - 1/24 (U_0 / \beta_a)^3 \sin 3\omega_2 t + 1/2 (U_0 / \beta_a)^2 \cos (\omega_2 t - \omega_1 t) - 1/2 (U_0 / \beta_a)^2 \cos (\omega_2 t + \omega_1 t) + 1/4 (U_0 / \beta_a)^3 \sin \omega_2 t + 1/8 (U_0 / \beta_a)^3 \sin (2\omega_1 t - \omega_2 t) - 1/8 (U_0 / \beta_a)^3 \sin (\omega_2 t + 2\omega_1 t) + 1/4 (U_0 / \beta_a)^3 \sin \omega_1 t + 1/8 (U_0 / \beta_a)^3 \sin (2\omega_2 t - \omega_1 t) - 1/8 (U_0 / \beta_a)^3 \sin (\omega_1 t + 2\omega_2 t)] - 1 \} \quad (12)$$

Replacing the amplitude for the corresponding terms in equation (22) with current components and rearranging,

$$\begin{aligned}
i = & i_{fr} + i_{\omega 1} \sin \omega_1 t + i_{\omega 2} \sin \omega_2 t - i_{2\omega 1} \cos 2\omega_1 t - i_{2\omega 2} \cos 2\omega_2 t - i_{3\omega 1} \sin 3\omega_1 t - i_{3\omega 2} \sin 3\omega_2 t + i_{\omega 2 \pm \omega 1} \\
& \cos (\omega_2 t - \omega_1 t) - i_{\omega 2 \pm \omega 1} \cos (\omega_2 t + \omega_1 t) + i_{2\omega 2 \pm \omega 1} \sin (2\omega_2 t - \omega_1 t) - i_{2\omega 2 \pm \omega 1} \sin (2\omega_2 t + \omega_1 t) + i_{2\omega 1 \pm \omega 2} \\
& \sin (2\omega_1 t - \omega_2 t) - i_{2\omega 1 \pm \omega 2} \sin (2\omega_1 t + \omega_2 t)
\end{aligned} \tag{13}$$

where,  $i_{fr}$  is the Faradaic rectification current

Thus, equating the amplitude for each of the respective terms of their corresponding orders

$$i_{\omega 1} = i_{\omega 2} = i_{0,ex} U_0 / \beta_a \tag{14}$$

$$i_{2\omega 1} = i_{2\omega 2} = i_{0,ex} 1/4 (U_0 / \beta_a)^2 \tag{15}$$

$$i_{3\omega 1} = i_{3\omega 2} = i_{0,ex} 1/24 (U_0 / \beta_a)^3 \tag{16}$$

$$i_{\omega 2 \pm \omega 1} = i_{0,ex} 1/2 (U_0 / \beta_a)^2 \tag{17}$$

$$i_{2\omega 2 \pm \omega 1} = i_{2\omega 1 \pm \omega 2} = i_{0,ex} 1/8 (U_0 / \beta_a)^3 \tag{18}$$

The above current components (14-18) are the respective harmonic and intermodulation current responses of the derived model after two sine waves of different frequencies have been applied on the system according to the EFM technique. Therefore using the above equations and rearranging for the expression  $i_{0,ex}$  and anodic Tafel coefficient ( $\beta_a$ ), it gives

$$i_{0,ex} = (i_{\omega 1, \omega 2}^2) / 2 i_{\omega 2 \pm \omega 1} \tag{19}$$

$$1/[1/i_{0,eff} - 1/i_{lim}] = (i_{\omega 1, \omega 2}^2) / 2 i_{\omega 2 \pm \omega 1} \tag{20}$$

$$\beta_a = [(i_{\omega 1, \omega 2}) / 2 i_{\omega 2 \pm \omega 1}] U_0 \tag{21}$$

The above two relations (20 & 21) can be used to roughly determine the exchange current and anodic Tafel parameter from the observed values of response currents obtained from EFM observed data.

## DEBANJAN DAS

### Education

Ph.D. in Energy & Mineral Engineering 2009 – 2016  
The Pennsylvania State University, USA

B.S in Chemical Engineering 2005 – 2009  
National Institute of Technology, Durgapur, India

### Research Experience

Graduate Research Experience, Penn State University Summer 2011 – Summer 2015

Electrochemical Intern, Lam Research Corporation, CA May 2014 – October 2014

### Publications

- “Impedance Spectra Effects in Solid Oxide Fuel Cells Operating on Alternative Fuel Reformate Streams poisoned by Inorganic Impurities”; **Debanjan Das**, Serguei N. Lvov, *J. Power Sources* (Submitted)
- “Electrochemical Frequency Modulation for Estimating the Exchange Current Density in Solid Oxide Fuel Cells”; **Debanjan Das**, Derek Hall, Serguei N. Lvov, *Electrochem Communications* (Submitted)
- “Sensitivity Studies of Fuel Characteristics and State of Health Investigation of a Planar SOFC Short Stack Operating on Syngas by Electrochemical Impedance Spectroscopy”; **Debanjan Das**, , Serguei N. Lvov, *International J. of Hydrogen Energy* (Submitted)
- “Atmospheric Microplasma Jet: Spectroscopic Database Development and Analytical Results” Randall Vander L. Wal, Jane H. Fujiyama-Novak, Chethan Kumar Gaddam, **Debanjan Das**, Aditya Hariharan, and Benjamin Ward, *Applied Spectroscopy* 65 (2011) 1073 -1082
- “Detection of explosives by plasma optical emission spectroscopy”, Jane H. Fujiyama-Novak, Chethan Kumar Gaddam, **Debanjan Das**, Randall L. Vander Wal, Benjamin Ward, *Sensors and Actuators* 176 (2013) 985 -993